AFOSR-TR-97

0172

REPORT DOCUMENTATION PAGE

Public reporting burden for this collection of information is estimated to average 1 hour per response, including the time for reviewing instructions, searching existing data sources, gathering and maintaining the data needed, and completing and reviewing the collection of information. Send comments regarding this burden estimate or any other aspect of this collection of information, including suggestions for reducing this burden, to Washington Headquarters Services, Directorate for information Operations and Reports, 1215 Jefferson Davis Highway, suite 1204, Arlington, VA 22202-4302, and to the Office of Management and Budget, Paperwork Reduction Project (0704-0188), Washington, DC 20503.

1. Agency Use Only (Leave blank)	2. Report Date 31-Mar-97	3. Report Type and Dates Covered Final Report, Dec. 1, 1994 — Jan. 31, 1997	
4. Title and Subtitle Linear and Nonlinear Evolution of Disturbances in Supersonic Streamwise Vortices			5. Funding Numbers C F49620-95-C-0011
6. Author(s) Mehdi Khorrami & Chau-Lyan Chang			
7. Performing Organization Name(s) and Address(es) High Technology Corporation 28 Research Drive Hampton, VA 23666			8. Performing Organization Report Number HTC-FR-1703
9. Sponsoring / Monitoring Agency Name(s) and Address(es) Air Force Office of Scientific Research 110 Duncan Avenue, Room B115 Bolling AFB, DC 20332-8080 _NA_			10. Sponsoring / Monitoring Agency Report Number 95-C-0011
11. Supplementary Notes			
12a. Distribution / Availability Statement "Distribution Statement A: Approved for Public release; distribution is Unlimited."			12b. Distribution Code

13. Abstract (Maximum 200 words)

Evolution of disturbances in a supersonic vortex is studied by using quasi-cylindrical linear stability analysis and parabolized stability equations (PSE) formulation. Appropriate mean-flow profiles suitable for stability analysis were identified and modeled successfully. Using the quasi-cylindrical linear stability code, the stability characteristics of cylinder axisymmetric vortices were mapped thoroughly and discussed in detail. Important trends such as viscous and compressibility effects were obtained and analyzed. The results indicate that viscosity has very little effect while increasing Mach number significantly stabilizes the disturbance. The streamwise evolution of the constructed base flow was obtained by solving quasi-cylindrical steady-state equations using finite-difference techniques and the resulting mean flow was analyzed by using PSE. Linear PSE analysis shows that the effect of streamwise mean flow variation (non-parallelism) is small for the case considered here. Nonlinear evolution of helical modes as well as modal interaction is also studied by using PSE. It is found that the growth of the disturbances results in the appearance of coherent large scale motion and significant mean flow distortion in the axial velocity and temperature fields. In the end, nonlinear effects tend to stabilize the vortex.

14. Subject Terms (1) supersonic streamwise vortices, (2) linear and nonlinear stability analysis (3) parabolized stability equations			15. Number of Pages 87
			16. Price Code

17. Security Classification of Report Unclassified	18. Security Classification of this Page Unclassified	19. Security Classification of Abstract Unclassified	20. Limitation of Abstract UL

NSN 7540-01-280-5500

Standard Form 298 (Rev. 2-89)

19970602 041   DTIC QUALITY INSPECTED 1

Linear and Nonlinear Evolution of Disturbances in Supersonic Streamwise Vortices

Mehdi R. Khorrami & Chau-Lyan Chang

High Technology Corporation
28 Research Drive
Hampton, VA 23666

Summary

Evolution of disturbances in a supersonic vortex is studied by using quasi-cylindrical linear stability analysis and parabolized stability equations (PSE) formulation. Appropriate mean-flow profiles suitable for stability analysis were identified and modeled successfully. Using the quasi-cylindrical linear stability code, the stability characteristics of cylinder axisymmetric vortices were mapped thoroughly and discussed in detail. Important trends such as viscous and compressibility effects were obtained and analyzed. The results indicate that viscosity has very little effect while increasing Mach number significantly stabilizes the disturbance. The streamwise evolution of the constructed base flow was obtained by solving quasi-cylindrical steady-state equations using finite-difference techniques and the resulting mean flow was analyzed by using PSE. Linear PSE analysis shows that the effect of streamwise mean flow variation (non-parallelism) is small for the case considered here. Nonlinear evolution of helical modes as well as modal interaction is also studied by using PSE. It is found that the growth of the disturbances results in the appearance of coherent large scale motion and significant mean flow distortion in the axial velocity and temperature fields. In the end, nonlinear effects tend to stabilize the vortex.

1. Introduction

Formation and subsequent downstream evolution of three-dimensional compressible streamwise vortices play a significant role in both external and internal flows. Effective control or dissipation of vortices is an important issue in such diverse areas as aircraft tail buffeting, helicopter blade vibration/fatigue, efficient mixing in combustion chambers, and jet-engine noise reduction. Unlike boundary-layer flows, however, the temporal and spatial evolution of compressible vortices has remained largely unexplored. Our lack of understanding of the critical features of compressible vortex evolution, such as stability characteristics, laminar-to-turbulent transition, and compressibility effects has prevented effective control of vortical flows in practical situations.

Therefore, the objective of the present study is to determine and understand the stability characteristics of a physically realizable compressible streamwise vortex. This study focuses on identifying the types of instability modes present in such a vortex with the hope that these modes may be actively manipulated in future research on vortex control. In particular, the linear and nonlinear growth and evolution of disturbances in a compressible vortex is analyzed using quasi-cylindrical linear stability analysis and parabolized stability formulation. Both approaches complement each other and together provide a detailed view of the stability characteristics of supersonic vortices.

2. Governing Equations

The full governing equations for a compressible, variable-property Newtonian fluid flow in cylindrical-polar (r, θ, z) coordinates are given by the Navier-Stokes equations. They are

mass conservation:

$$\frac{D\tilde{\rho}}{Dt} + \tilde{\rho}\mathbf{V} \cdot \vec{V} = 0 , \qquad (2.1)$$

radial-momentum:

$$\tilde{\rho}\left[\frac{Du_r}{Dt} - \frac{u_\theta^2}{r}\right] = -\frac{\partial \tilde{p}}{\partial r} + \frac{\partial}{\partial r}\left[2\tilde{\mu}\frac{\partial u_r}{\partial r} + \tilde{\lambda}\mathbf{V} \cdot \vec{V}\right] + \frac{1}{r}\frac{\partial}{\partial \theta}\left[\tilde{\mu}\left(\frac{1}{r}\frac{\partial u_r}{\partial \theta} + \frac{\partial u_\theta}{\partial r} - \frac{u_\theta}{r}\right)\right]$$

$$+ \frac{\partial}{\partial z}\left[\tilde{\mu}\left(\frac{\partial u_r}{\partial z} + \frac{\partial u_z}{\partial r}\right)\right] + \frac{2\tilde{\mu}}{r}\left(\frac{\partial u_r}{\partial r} - \frac{1}{r}\frac{\partial u_\theta}{\partial \theta} - \frac{u_r}{r}\right), \qquad (2.2)$$

tangential-momentum:

$$\tilde{\rho}\left[\frac{Du_\theta}{Dt}+\frac{u_r u_\theta}{r}\right]=-\frac{1}{r}\frac{\partial\tilde{p}}{\partial\theta}+\frac{1}{r}\frac{\partial}{\partial\theta}\left[2\tilde{\mu}\left(\frac{1}{r}\frac{\partial u_\theta}{\partial\theta}+\frac{u_r}{r}\right)+\tilde{\lambda}\mathbf{\nabla}\cdot\vec{V}\right]+\frac{\partial}{\partial z}\left[\tilde{\mu}\left(\frac{1}{r}\frac{\partial u_z}{\partial\theta}+\frac{\partial u_\theta}{\partial z}\right)\right]$$

$$+\frac{\partial}{\partial r}\left[\tilde{\mu}\left(\frac{1}{r}\frac{\partial u_r}{\partial\theta}+\frac{\partial u_\theta}{\partial r}-\frac{u_\theta}{r}\right)\right]+\frac{2\tilde{\mu}}{r}\left(\frac{1}{r}\frac{\partial u_r}{\partial\theta}+\frac{\partial u_\theta}{\partial r}-\frac{u_\theta}{r}\right), \tag{2.3}$$

axial-momentum:

$$\tilde{\rho}\frac{Du_z}{Dt}=-\frac{\partial\tilde{p}}{\partial z}+\frac{\partial}{\partial z}\left[2\tilde{\mu}\frac{\partial u_z}{\partial z}+\tilde{\lambda}\mathbf{\nabla}\cdot\vec{V}\right]+\frac{1}{r}\frac{\partial}{\partial r}\left[\tilde{\mu}r\left(\frac{\partial u_r}{\partial z}+\frac{\partial u_z}{\partial r}\right)\right]$$

$$+\frac{1}{r}\frac{\partial}{\partial\theta}\left[\tilde{\mu}\left(\frac{1}{r}\frac{\partial u_z}{\partial\theta}+\frac{\partial u_\theta}{\partial z}\right)\right], \tag{2.4}$$

and, for a perfect gas,
energy:

$$\tilde{\rho}C_p\frac{D\tilde{T}}{Dt}=\frac{D\tilde{p}}{Dt}+\mathbf{\nabla}\cdot\left(\tilde{\kappa}\mathbf{\nabla}\tilde{T}\right)+\tilde{\Phi}, \tag{2.5}$$

where the dissipation function is

$$\tilde{\Phi}=\tilde{\mu}\left\{2\left[\left(\frac{\partial u_r}{\partial r}\right)^2+\left(\frac{1}{r}\frac{\partial u_\theta}{\partial\theta}+\frac{u_r}{r}\right)^2+\left(\frac{\partial u_z}{\partial z}\right)^2\right]+\left(\frac{1}{r}\frac{\partial u_z}{\partial\theta}+\frac{\partial u_\theta}{\partial z}\right)^2+\left(\frac{\partial u_r}{\partial z}+\frac{\partial u_z}{\partial r}\right)^2\right.$$

$$\left.\left(\frac{1}{r}\frac{\partial u_r}{\partial\theta}+\frac{\partial u_\theta}{\partial r}-\frac{u_\theta}{r}\right)^2\right\}+\tilde{\lambda}\left[\frac{\partial u_r}{\partial r}+\frac{1}{r}\frac{\partial u_\theta}{\partial\theta}+\frac{u_r}{r}+\frac{\partial u_z}{\partial z}\right]^2,$$

with

$$\frac{D}{Dt}\equiv\frac{\partial}{\partial t}+u_r\frac{\partial}{\partial r}+\frac{u_\theta}{r}\frac{\partial}{\partial\theta}+u_z\frac{\partial}{\partial z},$$

and

$$\mathbf{\nabla}\cdot\vec{V}\equiv\frac{1}{r}\frac{\partial}{\partial r}(ru_r)+\frac{1}{r}\frac{\partial u_\theta}{\partial\theta}+\frac{\partial u_z}{\partial z}.$$

In equations (2.1)–(2.5), u_r, u_θ, u_z, $\tilde{p}$, $\tilde{T}$, and $\tilde{\rho}$ represent the three components of velocity, pressure, temperature and density, respectively. The coefficients $\tilde{\mu}$, $\tilde{\lambda}$, $\tilde{\kappa}$ and C_p denote the fluid dynamic viscosity, second coefficient of viscosity, thermal conductivity, and specific heat at

constant pressure, respectively, which are taken to be functions of temperature only. Finally, the above system of equations is closed with the addition of the ideal gas equation of state

$$\tilde{p} = \tilde{\rho} R \tilde{T} \ . \tag{2.6}$$

3. Construction of the Mean-Flow Profile

The selection of the mean-flow profiles for a supersonic vortex is not as straightforward as in the incompressible case and therefore must be handled with great care. One of the main concerns is to make certain that the chosen base flow is physically realizable. Unfortunately, the similarity solution of a compressible vortex obtained by Mayer and Powell (1992b) is not a good model for the flow field of interest, because their solutions do not resemble previous measurements of compressible vortices. Therefore, we decided to construct the mean-flow profiles from experimentally measured data. For this purpose, the work of Smart, Kalkhoran and Bentson (1994) provided some of the most extensive measurements of supersonic streamwise vortices. The construction of the base flow is presented and discussed in more detail in the following sections.

3.1 Profile Based on Smart et al. (1994) Measurements

The measurements of Smart et al. provide the necessary database to construct the velocity profiles for supersonic wing-tip vortices. The vortex generation is accomplished via a rectangular half-wing with a diamond-shaped cross section which is mounted vertically in the test section. Experimental flow visualization revealed the supersonic vortices to be slender. That is, compared to the radial gradients, the axial gradients tend to be small. Measurements were obtained for angles of attack of 10° (stronger vortex) and 5° (weaker vortex). These vortices show significant axial velocity deficit in the vortex core and thus are expected to be highly unstable. The 10° case was successfully modeled and is presented below.

The procedure for constructing the profiles is as follows. In the cylindrical coordinates (r, θ, z), let $\Pi(r)$ and $\eta(r)$ represent the non-dimensional pressure and temperature, respectively. In what follows, the pressure, temperature, and density are normalized by the far-field values of dynamic pressure $\rho_\infty W_\infty^2$, static temperature η_∞, and density ρ_∞, respectively. The radial coordinate is normalized by the value of the radial coordinate r_0 where the tangential velocity is a maximum, and the velocities are nondimensionalized by the far-field value of the axial velocity W_∞.

Noting that for a slender vortex the radial velocity u_r is negligible, good fits to the following expressions for the measured tangential and axial velocities were found to fit the data well,

$$u_\theta = V(r) = \frac{q}{r}\left(1 - e^{-r^2}\right), \tag{3.1}$$

4

and

$$u_z = W(r) = 1 - \delta e^{-2.4r^2}, \tag{3.2}$$

where q is the usual swirl parameter similar to that defined for the Batchelor vortex (see Lessen et al. 1974) and δ is the axial velocity deficit. Unfortunately, no measurements of temperature across the vortex were reported by Smart et al. (1994). As a first step, the total temperature is assumed to be constant throughout the vortex. The total temperature η_t then is given by

$$\eta_t = \text{constant} = \beta \tag{3.3}$$

where at a sufficiently large radius, β is determined from

$$\beta = 1 + \frac{1}{2}(\gamma - 1)M_\infty^2, \tag{3.4}$$

with

$$M_\infty = \frac{W_\infty}{\sqrt{\gamma R \eta_\infty}}. $$

Assuming the flow is locally adiabatic, the static temperature distribution, η, across the vortex is given by

$$\eta(r) = \beta - \frac{(\gamma-1)}{2}M_\infty^2\left(V^2 + W^2\right). \tag{3.5}$$

For a quasi-cylindrical vortex, the radial momentum equation for the mean flow reduces to

$$\frac{d\Pi}{dr} = \rho\frac{V^2}{r}. \tag{3.6}$$

or

$$\frac{d\Pi}{\Pi} = \frac{\gamma M_\theta^2}{r}dr. \tag{3.7}$$

Integrating both sides, we obtain

$$\Pi(r) = \frac{e^{-\gamma\int_r^\infty \frac{M_\theta^2}{r}dr}}{\gamma M_\infty^2}. \tag{3.8}$$

A numerical integration thus provides the pressure after substituting the experimentally determined M_θ distribution in equation (3.8). Finally, the density variation is obtained from the ideal gas law

$$\rho = \gamma M_\infty^2 \frac{\Pi}{\eta} \ .$$ (3.9)

3.2 Quasi-Cylindrical Computation of Base Flow

The fitted vortex (3.1)–(3.9) is used as an initial profile to obtain the streamwise evolution and quasi-cylindrical nature of the vortex base-flow. The computed mean flows at different streamwise locations were subsequently used to determine the effect of core expansion on the vortex stability characteristics. In addition, the computed mean flows were used in conjunction with the Parabolized Stability Equation (PSE) formulation to determine linear and nonlinear evolution of disturbances in supersonic vortices.

A numerical method for modeling isolated compressible vortices is presented. The formulation is based on the assumptions that the vortex is steady, quasi-axisymmetric, and slender. The governing equations and the solution procedure are discussed in the following sections.

3.2.1 *Governing equations*

The governing equations are derived starting from the full unsteady, compressible Navier-Stokes equations in cylindrical coordinates (given by Eqs. (2.1)–(2.5) in Section 2.0) where z is the axial direction, r is the radial direction, θ is the azimuthal direction, and u, v, w are the velocity components in the r, θ, and z directions, respectively. Assuming the vortex is steady ($\partial/\partial t = 0$), quasi-axisymmetric ($\partial/\partial\theta = 0$), and slender ($r_{core} \ll L$ where r_{core} is the vortex core radius and L is the breakdown length), the Navier-Stokes equations reduce to

Continuity:
$$\frac{\partial}{\partial z}(\rho w) + \frac{1}{r}\frac{\partial}{\partial r}(r\rho u) = 0$$ (3.10)

Axial momentum:
$$\rho\left[w\frac{\partial w}{\partial z} + u\frac{\partial w}{\partial r}\right] = -\frac{\partial p}{\partial z} + \frac{1}{r}\frac{\partial}{\partial r}\left[\mu r\frac{\partial w}{\partial r}\right]$$ (3.11)

Azimuthal momentum:
$$\rho\left[w\frac{\partial v}{\partial z} + u\frac{\partial v}{\partial r} + \frac{uv}{r}\right] = \frac{1}{r^2}\frac{\partial}{\partial r}\left[\mu r^3\frac{\partial}{\partial r}\left(\frac{v}{r}\right)\right]$$ (3.12)

Radial momentum:
$$\frac{\rho v^2}{r} = \frac{\partial p}{\partial r}$$ (3.13)

6

Energy:
$$\rho C_p \left[w \frac{\partial T}{\partial z} + u \frac{\partial T}{\partial r} \right] = w \frac{\partial p}{\partial z} + u \frac{\partial p}{\partial r} + \frac{1}{r} \frac{\partial}{\partial r} \left[rk \frac{\partial T}{\partial r} \right] +$$

$$\mu \left[\left(\frac{\partial w}{\partial r} \right)^2 + \left\{ r \frac{\partial}{\partial r} \left(\frac{v}{r} \right) \right\}^2 \right] \tag{3.14}$$

Equation of state:
$$p = \rho RT \tag{3.15}$$

Here, ρ is the density, p is the static pressure, T is the static temperature, R is the gas constant, and μ, k, and C_p are the coefficients of dynamic viscosity, thermal conductivity, and specific heat at constant pressure, respectively. This set of equations is similar to the boundary-layer equations except that the radial momentum equation is retained and the pressure is allowed to vary through the vortex core.

Equations (3.10) through (3.15) are nondimensionalized based on the following procedure:

$$\overline{z} = \frac{z}{r_0} \qquad \overline{r} = \frac{r}{r_0} \qquad \overline{u} = \frac{u}{a_\infty} \qquad \overline{v} = \frac{v}{a_\infty} \qquad \overline{w} = \frac{w}{a_\infty} \qquad \overline{\rho} = \frac{\rho}{\rho_\infty} \qquad \overline{p} = \frac{p}{\rho_\infty a_\infty^2}$$

$$\overline{T} = \frac{T}{a_\infty^2 / C_p} \qquad \overline{\mu} = \frac{\mu}{\mu_\infty} \qquad M_\infty = \frac{W_\infty}{a_\infty} \qquad Pr = \frac{\mu C_p}{k} \qquad Re = \frac{\rho_\infty W_\infty r_0}{\mu_\infty}$$

where r_0 is the initial vortex core radius, a_∞ is the freestream speed of sound, ρ_∞ is the freestream density, μ_∞ is the freestream coefficient of dynamic viscosity, M_∞ is the freestream Mach number, Pr is the Prandtl number, and Re is the Reynolds number. In terms of these nondimensional variables, the governing equations become (the overbars are omitted)

Continuity:
$$\frac{\partial}{\partial z} (\rho w) + \frac{1}{r} \frac{\partial}{\partial r} (r\rho u) = 0 \tag{3.16}$$

Axial momentum:
$$\rho \left[w \frac{\partial w}{\partial z} + u \frac{\partial w}{\partial r} \right] = - \frac{\partial p}{\partial z} + \frac{M_\infty}{Re} \frac{1}{r} \frac{\partial}{\partial r} \left[\mu r \frac{\partial w}{\partial r} \right] \tag{3.17}$$

Azimuthal momentum:
$$\rho \left[w \frac{\partial v}{\partial z} + u \frac{\partial v}{\partial r} + \frac{uv}{r} \right] = \frac{M_\infty}{Re} \frac{1}{r^2} \frac{\partial}{\partial r} \left[\mu r^3 \frac{\partial}{\partial r} \left(\frac{v}{r} \right) \right] \tag{3.18}$$

Radial momentum:
$$\frac{\rho v^2}{r} = \frac{\partial p}{\partial r} \tag{3.19}$$

Energy:
$$\rho\left[w\frac{\partial T}{\partial z}+u\frac{\partial T}{\partial r}\right]=w\frac{\partial p}{\partial z}+u\frac{\partial p}{\partial r}+\frac{M_\infty}{Pr\,Re}\frac{1}{r}\frac{\partial}{\partial r}\left[r\mu\frac{\partial T}{\partial r}\right]+$$

$$\frac{M_\infty}{Re}\mu\left[\left(\frac{\partial w}{\partial r}\right)^2+\left\{r\frac{\partial}{\partial r}\left(\frac{v}{r}\right)\right\}^2\right] \tag{3.20}$$

Equation of state:
$$p=\frac{\gamma-1}{\gamma}\rho T \tag{3.21}$$

In the present formulation, μ is determined from Sutherland's viscosity law which takes the following form in terms of the nondimensional variables:

$$\mu=[(\gamma-1)T]^{3/2}\frac{1+C}{(\gamma-1)T+C}\quad\text{where}\quad C=\frac{110.4^\circ K}{T_\infty} \tag{3.22}$$

Once μ is known, the thermal conductivity k is determined from the Prandtl number. The boundary conditions at $r=0$ and $r\to\infty$ are

$$r=0:\ u=v=\frac{\partial w}{\partial r}=\frac{\partial T}{\partial r}=0 \tag{3.23}$$

$$r\to\infty:\ \frac{\partial w}{\partial r}=\frac{\partial(rv)}{\partial r}=\frac{\partial T}{\partial r}=0 \tag{3.24}$$

$$p=p_e(z) \tag{3.25}$$

With M_∞, Re, T_∞, Pr, and $p_e(z)$ specified, Eqs. (3.16)–(3.21) can be marched along the axial direction starting from a set of initial profiles for w, v, and T at $z=z_0$. The initial profiles for p and ρ are obtained from Eqs. (3.19) and (3.21) while u is set to zero at $z=z_0$.

3.2.2 *Solution procedure*

Equations (3.16)–(3.21) are solved in a decoupled manner at each marching step. First, the axial momentum, azimuthal momentum, and energy equations are marched to obtain w, v, and T. Next, p and ρ are computed by integrating the radial momentum equation together with the equation of state. Finally, u is obtained by integrating the continuity equation. The entire solution procedure is described in detail below.

8

<u>Step 1</u>:

In the first step w, v, and T are computed from Eqs. (3.17), (3.18), and (3.20). These three equations are first written in vector form as follows

$$\frac{\partial \mathbf{Q}}{\partial z} + \mathbf{A}\ \frac{\partial \mathbf{Q}}{\partial r} = \mathbf{B} \tag{3.26}$$

where

$$\mathbf{Q} = \begin{bmatrix} w \\ v \\ T \end{bmatrix} \qquad \mathbf{A} = \begin{bmatrix} \dfrac{u}{w} & 0 & 0 \\ 0 & \dfrac{u}{w} & 0 \\ 0 & 0 & \dfrac{u}{w} \end{bmatrix}$$

$$\mathbf{B} = \begin{bmatrix} -\dfrac{1}{\rho w}\dfrac{\partial p}{\partial z} + \dfrac{M_\infty}{Re}\dfrac{1}{r\rho w}\dfrac{\partial}{\partial r}\left[\mu r \dfrac{\partial w}{\partial r}\right] \\[3mm] -\dfrac{uv}{rw} + \dfrac{M_\infty}{Re}\dfrac{1}{r^2\rho w}\dfrac{\partial}{\partial r}\left[\mu r^3 \dfrac{\partial}{\partial r}\left(\dfrac{v}{r}\right)\right] \\[3mm] \dfrac{1}{\rho}\dfrac{\partial p}{\partial z} + \dfrac{uv^2}{rw} + \dfrac{M_\infty}{Pr\,Re}\dfrac{1}{r\rho w}\dfrac{\partial}{\partial r}\left[\mu r \dfrac{\partial T}{\partial r}\right] + \dfrac{M_\infty}{Re}\dfrac{\mu}{\rho w}\left[\left(\dfrac{\partial w}{\partial r}\right)^2 + \left\{r\dfrac{\partial}{\partial r}\left(\dfrac{v}{r}\right)\right\}^2\right] \end{bmatrix}$$

Equation (3.26) is discretized using the implicit Crank-Nicolson scheme which is second-order accurate in both spatial directions. On a computational grid with uniform grid spacing, the resulting expression is

$$\frac{\mathbf{A}_j^{i+1,n}}{4\Delta r}\mathbf{Q}_{j+1}^{i+1,n+1} + \frac{1}{\Delta z}\mathbf{Q}_j^{i+1,n+1} - \frac{\mathbf{A}_j^{i+1,n}}{4\Delta r}\mathbf{Q}_{j-1}^{i+1,n+1} = \frac{\mathbf{Q}_j^i}{\Delta z} - \frac{\mathbf{A}_j^i}{4\Delta r}\left[\mathbf{Q}_{j+1}^i - \mathbf{Q}_{j-1}^i\right] + \mathbf{B}_j^{i+1/2,n} \tag{3.27}$$

Here, superscript i and subscript j denote the discrete axial and radial locations, respectively, and superscript n represents the nonlinear iteration index. The solution of this equation requires the inversion of a 3 x 3 block tridiagonal matrix. The boundary conditions applied at $r = 0$ and $r = r_{max}$ are

r = 0:
$$\frac{\partial w}{\partial r} = 0 \rightarrow w_1 = w_2$$

$$v = 0 \rightarrow v_1 = 0$$

$$\frac{\partial T}{\partial r} = 0 \rightarrow T_1 = T_2$$

9

$$r = r_{max}: \qquad \frac{\partial w}{\partial r} = 0 \rightarrow w_{jmax} = w_{jmax-1}$$

$$\frac{\partial (rv)}{\partial r} = 0 \rightarrow v_{jmax} = \frac{r_{jmax-1}}{r_{jmax}} v_{jmax-1}$$

$$\frac{\partial T}{\partial r} = 0 \rightarrow T_{jmax} = T_{jmax-1}$$

Step 2:

After w, v and T are determined, ρ is computed by integrating Eq. (3.19) together with Eq. (3.21) from $r = r_{max}$ to $r = 0$. At $r = r_{max}$, ρ is obtained from the equation of state as follows:

$$\rho_{jmax} = \frac{\gamma}{\gamma - 1} \frac{p_e}{T_{jmax}}$$

Here either p_e or $\partial p_e / \partial z$ needs to be specified at $r = r_{max}$. If $\partial p_e / \partial z$ is specified, p_e is obtained as

$$p_e^{i+1} = p_e^i + \Delta z \frac{\partial p_e}{\partial z}$$

Once ρ is known, p is computed from the equation of state.

Step 3:

In the final step, u is computed by integrating Eq. (3.16) from $r = 0$ where $u = 0$ to $r = r_{max}$ using the values of w and ρ obtained in steps 1 and 2, respectively.

After ρ, p, and u are computed as described in steps 2 and 3, the left hand side matrix **A** and the right hand side vector **B** in Eq. (3.27) are then updated and the entire process (i.e., steps 1 through 3) is repeated until the solution converges. Note that in this solution procedure, the streamwise pressure gradient term in Eq. (3.26) is specified and treated as a source term at each iteration. Therefore, the stability problem associated with space marching in subsonic flow regions is avoided.

Numerical computations of the mean flowfield allows the variation of parameters such as vortex strength q, Mach number M_∞, and Reynolds number Re independently. In this manner, important effects (e.g., compressibility, viscous, etc.) can be isolated. Smart et al.'s experiments were conducted at a nominal Mach number of 2.49. Although variation of different flow parameters may cause the computed flowfield to become unrealizable in their tunnel, the realizability of the flowfield in some other tunnels is insured as long as numerically converged

solutions are obtained. The computed profiles for q = 0.2, Re = 30000, and M_∞ = 2.49 at several axial locations are presented in Figures 1a–1g. The vortex initial axial velocity deficit is 35% for these cases. Note viscous diffusion only significantly affects axial velocity, static temperature, and density while tangential velocity and static pressure remain unaffected.

4.   Stability Equations

The set of equations (2.1) – (2.6) provide the starting point for the derivation of any form of stability equations. In the present case, the base flowfield obtained by solving the axisymmetric slender vortex equations (section 3.2) is perturbed by small fluctuations. The flow variables then are assumed to consist of a mean part and a fluctuating part, i.e.,

$$u = U_r + \varepsilon u'_r, \quad v = U_\theta + \varepsilon u'_\theta, \quad w = U_z + \varepsilon u'_z$$

$$\tilde{p} = P + \varepsilon p', \quad \tilde{\rho} = \rho + \varepsilon \rho', \quad \tilde{T} = T + \varepsilon T' \tag{4.1}$$

and

$$\mu = \mu(\tilde{T}), \quad \lambda = \lambda(\tilde{T}), \quad \kappa = \kappa(\tilde{T}), \tag{4.2}$$

where ε denotes an infinitesimal quantity. Substituting equation (4.1)–(4.2) into the (2.1)–(2.6) and collecting terms in powers of ε, one obtains the equations governing linear and nonlinear evolution of small disturbances in compressible streamwise vortices. These, equations which are quite complicated and long (but straight forward to derive), provide the basis for developing the linear stability and parabolized stability formulations.

4.1 Quasi-Cylindrical Linear Stability Formulation

Linear stability analysis is applicable in the early stages of the disturbance evolution where, due to the smallness of the fluctuation amplitude, no significant modal interaction or mean flow distortion exists. The governing equations are obtained by keeping terms of O(ε) and neglecting all higher order terms. In this formulation, the base flow is very slowly developing in the streamwise direction and therefore at each downstream z station the local mean flow quantities are taken to be functions of the radial coordinate only. Next, the perturbations are assumed to be composed of three-dimensional helical Fourier modes. The flow variables are then written as

$$
\begin{Bmatrix} u \\ v \\ w \\ \tilde{p} \\ \tilde{T} \\ \tilde{\rho} \end{Bmatrix} = \begin{Bmatrix} U(r) \\ V(r) \\ W(r) \\ \Pi(r) \\ \eta(r) \\ \rho(r) \end{Bmatrix} + \begin{Bmatrix} F(r) \\ G(r) \\ H(r) \\ P(r) \\ T(r) \\ \Delta(r) \end{Bmatrix} e^{i(\alpha z + n\theta - \omega t)} \,,
\tag{4.3}
$$

where, F, G, H, P, T and Δ are the disturbance complex amplitudes which are only functions of the radial coordinate. For the temporal solution, the variables α and n are the real-valued wavenumbers in the axial and azimuthal directions, respectively. The azimuthal wave number is an integer where $n \neq 0$ indicates helical waves and $n = 0$ represent axisymmetric modes. The angular frequency ω is complex, and the sign of its imaginary part, ω_i, determines whether the disturbances will grow (unstable if $\omega_i > 0$) or decay (stable if $\omega_i < 0$). For the spatial formulation, ω and n are taken to be real and complex α is sought. If the imaginary part of the wave number α is negative $\alpha_i < 0$, the disturbance grows in space (unstable), and if $\alpha_i > 0$ it decays (stable). Substituting (4.3) into the $O(\varepsilon)$ terms in the equations and neglecting terms containing streamwise derivative of the mean flow, the linearized stability equations in terms of the perturbation eigenfunctions are obtained. These quasi-cylindrical equations in nondimensional form are:

mass conservation:

$$
\frac{dF}{dr} + \left[\frac{1}{\Pi}\frac{d\Pi}{dr} - \frac{1}{\eta}\frac{d\eta}{dr} + \frac{1}{r} \right]F + \left[\frac{in}{r} \right]G + [i\alpha]H + \left[\frac{U}{\Pi} \right]\frac{dP}{dr}\frac{dF}{dr} + \left[\frac{U}{\Pi} \right]\frac{dP}{dr}
$$

$$
+ \left[\frac{inV}{r\Pi} - \frac{U}{\Pi\eta}\frac{d\eta}{dr} + \frac{1}{\Pi}\left(\frac{dU}{dr} + \frac{U}{r} \right) + \frac{i\alpha W}{\Pi} - \frac{i\omega}{\Pi} \right]P - \left[\frac{U}{\eta} \right]\frac{dT}{dr} + \left[\frac{2U}{\eta^2}\frac{d\eta}{dr} - \frac{U}{\Pi\eta}\frac{d\Pi}{dr} - \frac{inV}{r\eta} \right.
$$

$$
\left. - \frac{1}{\eta}\left(\frac{dU}{dr} + \frac{U}{r} \right) - \frac{i\alpha W}{\eta} + \frac{i\omega}{\eta} \right]T = 0
\tag{4.4}
$$

r-momentum:

$$
\left[2 + \frac{\lambda}{\mu} \right]\frac{d^2F}{dr^2} + \left[-\frac{\mathrm{Re}\,\rho U}{\mu} + \frac{1}{\mu}\frac{d\eta}{dr}\left(2\frac{d\mu}{d\eta} + \frac{d\lambda}{d\eta} \right) + \frac{1}{r}\left(2 + \frac{\lambda}{\mu} \right) \right]\frac{dF}{dr} + \left[\frac{i\omega\,\mathrm{Re}\,\rho}{\mu} - \frac{\mathrm{Re}\,\rho}{\mu}\frac{dU}{dr} - \frac{in\,\mathrm{Re}\,\rho V}{\mu r} \right.
$$

12

$$-\frac{i\alpha\,\mathrm{Re}\,\rho W}{\mu}+\frac{2}{\mu r}\frac{d\lambda}{d\eta}\frac{d\eta}{dr}-\frac{1}{r^2}\left(2+\frac{\lambda}{\mu}\right)-\frac{n^2}{r^2}-\alpha^2\right]F+\left[\frac{in}{r}\left(1+\frac{\lambda}{\mu}\right)\right]\frac{dG}{dr}+\left[\frac{2\,\mathrm{Re}\,\rho V}{\mu r}\right.$$

$$+\frac{in}{r\mu}\frac{d\lambda}{d\eta}\frac{d\eta}{dr}-\frac{in}{r^2}\left(3+\frac{\lambda}{\mu}\right)\right]G+\left[i\alpha\left(1+\frac{\lambda}{\mu}\right)\right]\frac{dH}{dr}+\left[\frac{i\alpha}{\mu}\frac{d\lambda}{d\eta}\frac{d\eta}{dr}\right]H-\left[\frac{\mathrm{Re}}{\mu}\right]\frac{dP}{dr}$$

$$-\left[\frac{\mathrm{Re}\,\rho}{\mu\Pi}\left(U\frac{dU}{dr}-\frac{V^2}{r}\right)\right]P+\left[\frac{2}{\mu}\frac{d\mu}{d\eta}\frac{dU}{dr}+\frac{1}{\mu}\frac{d\lambda}{d\eta}\left(\frac{dU}{dr}+\frac{U}{r}\right)\right]\frac{dT}{dr}+\left[\frac{2}{\mu}\frac{d^2\mu}{d\eta^2}\frac{d\eta}{dr}\frac{dU}{dr}+\frac{2}{\mu}\frac{d\mu}{d\eta}\frac{d^2U}{dr^2}\right.$$

$$+\frac{1}{\mu}\frac{d^2\lambda}{d\eta^2}\frac{d\eta}{dr}\left(\frac{dU}{dr}+\frac{U}{r}\right)+\frac{1}{\mu}\frac{d\lambda}{d\eta}\left(\frac{d^2U}{dr^2}-\frac{U}{r}+\frac{1}{r}\frac{dU}{dr}\right)+\frac{in}{\mu}\frac{d\mu}{d\eta}\left(\frac{1}{r}\frac{dV}{dr}-\frac{V}{r}\right)$$

$$+\frac{\mathrm{Re}\,\rho}{\mu\eta}\left(U\frac{dU}{dr}-\frac{V^2}{r}\right)+\frac{i\alpha}{\mu}\frac{d\mu}{d\eta}\frac{dW}{dr}+\frac{2}{\mu}\frac{d\mu}{d\eta}\left(\frac{1}{r}\frac{dU}{dr}-\frac{U}{r^2}\right)\right]T=0 \qquad (4.5)$$

θ-momentum:

$$\left[\frac{in}{r}\left(1+\frac{\lambda}{\mu}\right)\right]\frac{dF}{dr}+\left[\frac{in}{r^2}\left(3+\frac{\lambda}{\mu}\right)-\frac{\mathrm{Re}\,\rho}{\mu}\frac{dV}{dr}-\frac{\mathrm{Re}\,\rho V}{\mu r}+\frac{in}{r}\frac{1}{\mu}\frac{d\mu}{d\eta}\frac{d\eta}{dr}\right]F+\frac{d^2G}{dr^2}+\left[\frac{1}{\mu}\frac{d\mu}{d\eta}\frac{d\eta}{dr}-\frac{\mathrm{Re}\,\rho U}{\mu}\right.$$

$$+\frac{1}{r}\right]\frac{dG}{dr}+\left[\frac{i\omega\,\mathrm{Re}\,\rho}{\mu}-\frac{in\,\mathrm{Re}\,\rho V}{\mu r}-\frac{i\alpha\,\mathrm{Re}\,\rho W}{\mu}-\frac{\mathrm{Re}\,\rho U}{\mu r}-\frac{n^2}{r^2}\left(2+\frac{\lambda}{\mu}\right)-\alpha^2-\frac{1}{r}\frac{1}{\mu}\frac{d\mu}{d\eta}\frac{d\eta}{dr}-\frac{1}{r^2}\right]G$$

$$-\left[\frac{\alpha n}{r}\left(1+\frac{\lambda}{\mu}\right)\right]H-\left[\frac{in\,\mathrm{Re}}{\mu r}+\frac{\mathrm{Re}\,\rho}{\mu\Pi}\left(U\frac{dV}{dr}+\frac{UV}{r}\right)\right]P+\left[\frac{1}{\mu}\frac{d\mu}{d\eta}\left(\frac{dV}{dr}-\frac{V}{r}\right)\right]\frac{dT}{dr}$$

$$+\left[\frac{\mathrm{Re}\,\rho}{\mu\eta}\left(U\frac{dV}{dr}+\frac{UV}{r}\right)+\frac{i2nU}{r^2}\frac{1}{\mu}\frac{d\mu}{d\eta}+\frac{in}{\mu}\frac{d\lambda}{d\eta}\left(\frac{1}{r}\frac{dU}{dr}+\frac{U}{r^2}\right)+\frac{1}{\mu}\frac{d^2\mu}{d\eta^2}\frac{d\eta}{dr}\left(\frac{dV}{dr}-\frac{V}{r}\right)\right.$$

$$+\frac{1}{\mu}\frac{d\mu}{d\eta}\left(\frac{d^2V}{dr^2}+\frac{V}{r^2}-\frac{1}{r}\frac{dV}{dr}\right)+\frac{2}{r\mu}\frac{d\mu}{d\eta}\left(\frac{dV}{dr}-\frac{V}{r}\right)\right]T=0 \qquad (4.6)$$

13

z-momentum:

$$\left[i\alpha\left(1+\frac{\lambda}{\mu}\right)\right]\frac{dF}{dr}+\left[\frac{i\alpha}{r}\left(1+\frac{\lambda}{\mu}\right)-\frac{\mathrm{Re}\,\rho}{\mu}\frac{dW}{dr}+\frac{i\alpha}{\mu}\frac{d\mu}{d\eta}\frac{d\eta}{dr}\right]F-\left[\frac{\alpha n}{r}\left(1+\frac{\lambda}{\mu}\right)\right]G+\frac{d^2H}{dr^2}+\left[-\frac{\mathrm{Re}\,\rho U}{\mu}\right.$$

$$\left.+\frac{1}{\mu}\frac{d\mu}{d\eta}\frac{d\eta}{dr}+\frac{1}{r}\right]\frac{dH}{dr}+\left[\frac{i\omega\mathrm{Re}\,\rho}{\mu}-\frac{in\,\mathrm{Re}\,\rho V}{\mu r}-\frac{i\alpha\,\mathrm{Re}\,\rho W}{\mu}-\alpha^2\left(2+\frac{\lambda}{\mu}\right)-\frac{n^2}{r^2}\right]H$$

$$-\left[\frac{\mathrm{Re}\,\rho U}{\mu\Pi}\frac{dW}{dr}+\frac{i\alpha\,\mathrm{Re}}{\mu}\right]P+\left[\frac{1}{\mu}\frac{d\mu}{d\eta}\frac{dW}{dr}\right]\frac{dT}{dr}+\left[\frac{\mathrm{Re}\,\rho U}{\mu\eta}\frac{dW}{dr}+\frac{i\alpha}{\mu}\frac{d\lambda}{d\eta}\left(\frac{dU}{dr}+\frac{U}{r}\right)\right.$$

$$\left.+\frac{1}{\mu}\frac{d\mu}{d\eta}\left(\frac{d^2W}{dr^2}+\frac{1}{r}\frac{dW}{dr}\right)+\frac{1}{\mu}\frac{d^2\mu}{d\eta^2}\frac{d\eta}{dr}\frac{dW}{dr}\right]T=0 \qquad (4.7)$$

energy-equation:

$$\left[2(\gamma-1)M_\infty^2\,\mathrm{Pr}\left\{\frac{2\mu}{\kappa}\frac{dU}{dr}+\frac{\lambda}{\kappa}\left(\frac{dU}{dr}+\frac{U}{r}\right)\right\}\right]\frac{dF}{dr}+\left[-\frac{\mathrm{Pr}\,\mathrm{Re}\,\rho}{\kappa}\frac{d\eta}{dr}+(\gamma-1)M_\infty^2\,\mathrm{Pr}\left\{\frac{\mathrm{Re}}{\kappa}\frac{d\Pi}{dr}+\frac{4\mu}{\kappa}\frac{U}{r^2}\right.\right.$$

$$\left.\left.+i2\alpha\frac{\mu}{\kappa}\frac{dW}{dr}+\frac{i2n\mu}{r\kappa}\left(\frac{dV}{dr}-\frac{V}{r}\right)+\frac{2}{r}\frac{\lambda}{\kappa}\left(\frac{dU}{dr}+\frac{U}{r}\right)\right\}\right]F+\left[2(\gamma-1)M_\infty^2\,\mathrm{Pr}\frac{\mu}{\kappa}\left(\frac{dV}{dr}-\frac{V}{r}\right)\right]\frac{dG}{dr}$$

$$+\left[\frac{2(\gamma-1)M_\infty^2\,\mathrm{Pr}}{r}\left\{\frac{i2n\mu U}{r\kappa}+\frac{in\lambda}{\kappa}\left(\frac{dU}{dr}+\frac{U}{r}\right)-\frac{\mu}{\kappa}\left(\frac{dV}{dr}-\frac{V}{r}\right)\right\}\right]G+\left[2(\gamma-1)M_\infty^2\,\mathrm{Pr}\frac{\mu}{\kappa}\frac{dW}{dr}\right]\frac{dH}{dr}$$

$$+\left[i2\alpha(\gamma-1)M_\infty^2\,\mathrm{Pr}\frac{\lambda}{\kappa}\left(\frac{dU}{dr}+\frac{U}{r}\right)\right]H+\left[\frac{(\gamma-1)M_\infty^2\,\mathrm{Pr}\,\mathrm{Re}}{\kappa}U\right]\frac{dP}{dr}+\left[-\frac{\mathrm{Pr}\,\mathrm{Re}\,\rho U}{\kappa\Pi}\frac{d\eta}{dr}\right.$$

$$\left.+\frac{i(\gamma-1)M_\infty^2\,\mathrm{Pr}\,\mathrm{Re}}{\kappa}\left(-\omega+\frac{nV}{r}+\alpha W\right)\right]P+\frac{d^2T}{dr^2}+\left[-\frac{\mathrm{Pr}\,\mathrm{Re}\,\rho U}{\kappa}+\frac{2}{\kappa}\frac{d\kappa}{d\eta}\frac{d\eta}{dr}+\frac{1}{r}\right]\frac{dT}{dr}$$

$$+\left[\frac{i\,\mathrm{Pr}\,\mathrm{Re}\,\rho}{\kappa}\left(\omega-\frac{nV}{r}-\alpha W\right)+\frac{\mathrm{Pr}\,\mathrm{Re}\,\rho U}{\kappa\eta}\frac{d\eta}{dr}+\frac{1}{\kappa}\frac{d^2\kappa}{d\eta^2}\left(\frac{d\eta}{dr}\right)^2-\frac{n^2}{r^2}-\alpha^2+\frac{1}{\kappa}\frac{d\kappa}{d\eta}\left(\frac{d^2\eta}{dr^2}+\frac{1}{r}\frac{d\eta}{dr}\right)\right.$$

14

$$+(\gamma-1)\ M_\infty^2 \mathrm{Pr} \frac{1}{\kappa}\frac{d\mu}{d\eta}\left(\frac{dW}{dr}\right)^2 \ +\frac{2(\gamma-1)M_\infty^2 \mathrm{Pr}}{\kappa}\frac{d\mu}{d\eta}\left\{\left(\frac{dU}{dr}\right)^2 +\frac{U^2}{r^2}\right\}$$

$$+\frac{(\gamma-1)M_\infty^2 \mathrm{Pr}}{\kappa}\frac{d\mu}{d\eta}\left\{\left(\frac{dV}{dr}-\frac{V}{r}\right)^2\right\}+\frac{(\gamma-1)M_\infty^2 \mathrm{Pr}}{\kappa}\frac{d\lambda}{d\eta}\left\{\left(\frac{dU}{dr}+\frac{U}{r}\right)^2\right\}\Bigg]T=0 \qquad (4.8)$$

In the linearized governing equations, the parameters Re, Pr and M_∞ represent the flow Reynolds, Prandtl, and Mach numbers, respectively. Moreover, fluctuations in the flow properties are related to the temperature perturbations via the assumed functional form of viscosity and thermal conductivity.

4.1.1 *Boundary Conditions and the Numerical Method*

The compressible governing equations (4.4)–(4.8) require eight boundary conditions. The appropriate boundary conditions on the centerline of the vortex depend on the wave number n, and must be chosen such that the solutions remain single-valued and smooth. The conditions at $r = 0$ (Khorrami 1991a) are

if $n=0$, $F(0)=G(0)=0$

$$\frac{dH}{dr}(0)=\frac{dT}{dr}(0)=0$$

if $n=\pm1$, $F(0)\pm iG(0)=0$

$$\frac{dF}{dr}(0)=0 \qquad\qquad (4.9)$$
$$H(0)=T(0)=0$$

if $|n|>1$, $F(0)=G(0)=0$

$$H(0)=T(0)=0.$$

The other set of the boundary conditions are applied at a large radial distance from the vortex centerline. Normally, at the far-field boundary, the disturbances are taken to approach zero; that is,

as $r\to\infty$ $F,G,H,T,\to 0$. $\qquad\qquad (4.10)$

The proper far-field behavior of the disturbances is shown more formally below. We restrict our attention to an inviscid analysis, even though in the numerical computations the effect of viscosity is fully taken into account. The reason for this restriction is two-fold. First, from the previous

incompressible results for three-dimensional vortices, the inviscid disturbances are known to be more unstable than the purely viscous modes of instability (Lessen et al. 1974, Mayer and Powell 1992a, Khorrami 1991b). Second, the Reynolds numbers of the experiments are quite high and therefore the inviscid disturbances are expected to dominate.

The limiting form of the mean-flow field developed in section 3.1 as $r \to \infty$ is

$$W, \quad \eta, \quad \rho \to 1, \quad \Pi \to \frac{1}{\gamma M_\infty^2}$$

$$V \to \frac{q}{r}, \quad \frac{dV}{dr} \to -\frac{q}{r^2} \tag{4.11}$$

$$\frac{dW}{dr}, \quad \frac{d\eta}{dr}, \quad \frac{d\rho}{dr}, \quad \frac{d\Pi}{dr} \to 0 \ .$$

Substituting these quantities into the governing stability equations for an inviscid, non-heat-conducting gas, the asymptotic form of the governing equations in the far-field are obtained. After much simplification, we get

$$\frac{d^2H}{dr^2} + \left(\frac{1}{r} - \frac{q^2 M_\infty^2}{r^3}\right)\frac{dH}{dr} - \left(\alpha^2 - M_\infty^2 \phi^2 + \frac{n^2}{r^2} - \frac{2q^2 M_\infty^2}{r^4}\right)H = 0 \ . \tag{4.12}$$

At a large radial distance from the vortex centerline, the solution to (4.12) approaches

$$H \sim K_n(\sigma r) \ , \tag{4.13}$$

where K_n is the modified Bessel function of the second kind of order n, and σ is given by

$$\sigma = \left[\alpha^2 - M_\infty^2 (\alpha - \omega)^2\right]^{1/2} . \tag{4.14}$$

The real part of σ is taken to be positive for the solution to remain finite. From equations (4.12)–(4.14), notice that in the limit as $M_\infty \to 0$, the incompressible solutions (Lessen et al. 1974, Ash and Khorrami 1995) are recovered. Proceeding a step further, it can be shown that for large arguments, the leading term expansion in (4.13) is

$$K_n(\sigma r) \sim \frac{e^{-\sigma r}}{\sigma r}. \tag{4.15}$$

The above behavior clearly demonstrates that the disturbances have a faster than exponential decay rate as $r \to \infty$. Thus, we may truncate the computational domain at a large radius $r_{\max}$ and enforce the boundary conditions given by (4.10).

The equations (4.4)–(4.8) and the boundary conditions (4.9)–(4.10) constitute a well-posed eigenvalue problem. Notice that there are no pressure boundary conditions given because the governing equations are discretized using a Chebyshev spectral collocation technique implemented on a staggered grid. In this method, the pressure terms are evaluated only at the interior nodal points, thus eliminating the need for any pressure conditions. The method is an extension of the formulations of Macaraeg, Streett and Hussaini (1988) and Khorrami (1991c) to the compressible rotating flow regime. The technique is very efficient and has been successfully applied to the case of compressible swirling jets by Khorrami (1991a, 1995). Next, for the temporal formulation, the discretized equations are arranged in a generalized eigenvalue format

$$E_1 \bar{x} = \omega E_2 \bar{x} \; , \tag{4.16}$$

where E_1 and E_2 are the square coefficient matrices of $O(5N_p)$ and N_p is the number of Chebyshev polynomials used in the expansion of the eigenfunctions. The eigenvector $\bar{x}$ is

$$\bar{x} = \begin{bmatrix} F & G & H & P & T \end{bmatrix}^T \; , \tag{4.17}$$

where the superscript T denotes the transpose. The solution of (4.16) for the eigenvalue ω is obtained utilizing any readily available QZ or LZ routines.

For the present study, the physical coordinate $[0, r_{\max}]$ is mapped into the computational domain $[-1,1]$ using the algebraic transformation

$$r = \hat{a}\frac{1+\xi}{\hat{b}-\xi} \; , \tag{4.18}$$

where $\hat{a}$ and $\hat{b}$ are constants with

$$\hat{b} = 1 + \frac{2\hat{a}}{r_{\max}} \; . \tag{4.19}$$

Throughout our studies, we found

$$4 \le \hat{a} \le 10 \; , \tag{4.20}$$

and

$$20 \le r_{\max} \le 60 \; , \tag{4.21}$$

to be sufficient to ensure that the computed results are domain independent and well resolved. Furthermore, the number of collocation points needed to obtain six or seven significant digits of accuracy varied between $70 \le N_p \le 130$.

4.2 Parabolized Stability Formulation

Parabolized stability formulation was pioneered by Herbert (1991), Bertolotti (1991), Bertolotti et al. (1992), Chang et al. (1991), and Chang and Malik (1994). The approach is applicable to flow fields that meet the following two important criteria. First, the base flow variations in the streamwise direction are relatively small and second, the disturbances are convective in nature. For supersonic streamwise vortices, which are of interest here, both of the above conditions are met.

4.2.1 *Governing Equations*

The governing equations for PSE are obtained by keeping all terms in the equations (A.1) – (A.5) (appendix A) up to the $O(\varepsilon^3)$. The full nonlinear equations are grouped and written in general form as

$$\Omega \frac{\partial \Phi}{\partial t} + A \frac{\partial \Phi}{\partial z} + B \frac{\partial \Phi}{\partial r} + \frac{C}{r} + D\Phi = \frac{1}{\text{Re}} \left\{ Q_{zz} \frac{\partial^2 \Phi}{\partial z^2} + Q_{zr} \frac{\partial^2 \Phi}{\partial z \partial r} + Q_{rr} \frac{\partial^2 \Phi}{\partial r^2} + \frac{Q_{z\theta}}{r} \frac{\partial^2 \Phi}{\partial z \partial \theta} \right.$$

$$\left. + \frac{Q_{r\theta}}{r} \frac{\partial^2 \Phi}{\partial r \partial \theta} + \frac{Q_{\theta\theta}}{r^2} \frac{\partial^2 \Phi}{\partial \theta^2} \right\} \tag{4.22}$$

where Φ is the perturbation vector given as

$$\Phi = \left\{ p', u_z', u_r', u_\theta', T' \right\}^T ,$$

and *Re* is the Reynolds number as defined in section 4.1. Matrices $\Omega, A, B, C, D, Q_{zz}, Q_{rr}, Q_{z\theta}, Q_{r\theta}$, and $Q_{\theta\theta}$ are Jacobians of the corresponding total flux vectors which are composed of a linear part with only mean flow quantities (denoted by superscripts ℓ below) and a nonlinear part which contains perturbation quantities (denoted by superscripts $n\ell$ below).

As in the previous section, the perturbations are assumed to be periodic in time and azimuthal direction resulting in an expansion of the form

$$\Phi(r,\theta,z) = \sum_{m=-\infty}^{\infty} \sum_{n=-\infty}^{\infty} \chi_{mn}(r,z) e^{i(n\theta - m\omega t)} . \tag{4.23}$$

18

For most flows of interest, it is sufficient to truncate the Fourier decomposition (4.23) after a finite number of modes

$$\Phi(r,\theta,z) = \sum_{m=-M}^{M} \sum_{n=-N}^{N} \chi_{mn}(r,z)e^{i(n\theta - m\omega t)} \tag{4.24}$$

where M and N are half the number of modes kept in the truncated series.

We are interested in the evolution of wave-like disturbances that are growing or decaying while convected downstream. Thus it can be assumed that $\chi(r,z)$ is composed of a fast oscillatory wave part plus a slowly varying shape function, i.e.,

$$\chi_{mn}(r,z) = \psi_{mn}(r,z)E_{mn}(z), \tag{4.25}$$

$$E_{mn}(z) = e^{i\int_{z_0}^{z} \alpha_{mn}(\tilde{z})d\tilde{z}}. \tag{4.26}$$

Substituting (4.24)–(4.26) into the governing equations, we obtain the equations for the shape function ψ_{mn} as

$$\hat{D}_{mn}\psi_{mn} + \hat{A}_{mn}\frac{\partial \psi_{mn}}{\partial z} + \hat{B}_{mn}\frac{\partial \psi_{mn}}{\partial r} - \frac{1}{\text{Re}}\left\{Q_{zz}^{\ell}\frac{\partial^2 \psi_{mn}}{\partial z^2} + Q_{zr}^{\ell}\frac{\partial^2 \psi_{mn}}{\partial z \partial r} + Q_{rr}^{\ell}\frac{\partial^2 \psi_{mn}}{\partial r^2}\right\} = F_{mn}/E_{mn}. \tag{4.27}$$

The left hand side of equation (4.27) contains only linear coefficient matrices and all nonlinear terms are included in the forcing function F_{mn} which is the Fourier component of the total forcing, $F^{n\ell}$ defined as

$$F^{n\ell} = -\Omega^{n\ell}\frac{\partial \Phi}{\partial t} - A^{n\ell}\frac{\partial \Phi}{\partial z} - B^{n\ell}\frac{\partial \Phi}{\partial r} - \frac{C^{n\ell}}{r}\frac{\partial \Phi}{\partial \theta} - D^{n\ell}\Phi + \frac{1}{\text{Re}}\left\{Q_{zz}^{n\ell}\frac{\partial^2 \Phi}{\partial z^2} Q_{zr}^{n\ell}\frac{\partial^2 \Phi}{\partial z \partial r}\right.$$

$$\left. + Q_{rr}^{n\ell}\frac{\partial^2 \Phi}{\partial r^2} + \frac{Q_{z\theta}^{n\ell}}{r}\frac{\partial^2 \Phi}{\partial z \partial \theta} + \frac{Q_{r\theta}^{n\ell}}{r}\frac{\partial^2 \Phi}{\partial r \partial \theta} + \frac{Q_{\theta\theta}^{n\ell}}{r^2}\frac{\partial^2 \Phi}{\partial \theta^2}\right\} \tag{4.28}$$

where all matrices with superscript $n\ell$ denote corresponding coefficients containing dependent variables Φ (nonlinear terms). The forcing function $F^{n\ell}$ is defined in physical space and can be evaluated by a similar Fourier series expansion

$$F^{n\ell}(r,\theta,z) = \sum_{m=-M}^{M} \sum_{n=-N}^{N} F_{mn}(r,z) e^{i(n\theta - m\alpha t)} . \qquad (4.29)$$

Computationally, the Fourier decomposition of equation (4.29) can be accomplished by using the Fast Fourier Transform (FFT) of $F^{n\ell}$ which is evaluated numerically in the physical space. The corresponding linear formulation is obtained by setting F_{mn} to zero in (4.27).

As it stands, equation (4.27) is elliptic in nature in particular due to the presence of the term $\dfrac{\partial^2 \psi_{mn}}{\partial z^2}$. The computational cost of solving such an equation is prohibitively expensive. PSE formulation removes this source of ellipticity based on physical and dimensional arguments. A brief overview of the procedure is given below.

In the PSE formulation, the perturbation quantities for a particular mode are expanded as,

$$u'_\theta = G(r,z) e^{i\int \alpha d\bar{z} + in\theta - i\alpha t} + c.c. \qquad (4.30)$$

with similar expansions for other flow variables. Here c.c. represents complex conjugate to ensure the physical quantities are real and is dropped from the subsequent discussion. Note that unlike the quasi-cylindrical expansion (4.3), here the disturbance amplitude is dependent on both radial and axial coordinates with the underlying assumption that streamwise variation is slow. Constructing the first and second derivatives of G in z, we have

$$\frac{\partial u'_\theta}{\partial z} = \left\{ i\alpha(z)G(r,z) + \frac{\partial G}{\partial z} \right\} e^{i\int \alpha d\bar{z} + in\theta - i\alpha t} \qquad (4.31)$$

$$\frac{\partial^2 u'_\theta}{\partial z^2} = \left\{ -\alpha^2(z)G(r,z) + i\frac{d\alpha(z)}{dz}G(r,z) + 2i\alpha(z)\frac{\partial G}{\partial z} + \frac{\partial^2 G}{\partial z^2} \right\} e^{i\int \alpha d\bar{z} + in\theta - i\alpha t} \qquad (4.32)$$

Since the mean flow variations are $O(\text{Re}^{-1})$, for moderate and high Reynolds number flows the wave amplitude is weakly dependent on the z coordinate. For these flows the term $\dfrac{\partial^2 G}{\partial z^2}$ can be omitted and the second derivative is approximated as

$$\frac{\partial^2 u'_\theta}{\partial z^2} \approx \left\{ -\alpha^2(z)G(r,z) + i\frac{d\alpha(z)}{dz}G(r,z) + 2i\alpha(z)\frac{\partial G}{\partial z} \right\} e^{i\int \alpha d\bar{z} + in\theta - i\alpha t} . \qquad (4.33)$$

Substituting expansion (4.30) into the equation (4.27) and utilizing approximation (4.33), all the second derivative terms will be removed and a set of partial differential equations which contain

only first derivatives in z is obtained. With the above simplification and after neglecting all terms of $O(\text{Re}^{-2})$, the following reduced equation is obtained

$$\hat{D}_{mn}\psi_{mn} + \hat{A}_{mn}\frac{\partial\psi_{mn}}{\partial z} + \hat{B}_{mn}\frac{\partial\psi_{mn}}{\partial r} - \frac{Q_{rr}^{\ell}}{\text{Re}}\frac{\partial^2\psi_{mn}}{\partial r^2} = F_{mn}/E_{mn}. \tag{4.34}$$

The emerging equation (4.34) which describes the evolution of the shape function ψ_{mn} is almost parabolized. For complete parabolizing (4.34), one needs to address the convective side of the governing equation. Here, the elliptic effects associated with the wave part is absorbed in matrices $\hat{D}_{mn}$, $\hat{A}_{mn}$ and $\hat{B}_{mn}$. The remaining ellipticity in the governing equation caused by the terms $\frac{\partial P}{\partial z}$ is a non-issue for the supersonic vortices of interest due to the absence of a subsonic region in the flow field.

4.2.2 *Boundary Conditions*

The boundary conditions on the centerline $r = 0$, are identical to the conditions (4.9) derived for the quasi-cylindrical stability formulation. In the farfield as $r \to \infty$, the Dirichlet boundary conditions (4.10) can be employed. For supersonic-mode disturbances, however, the farfield Dirichlet conditions may not be appropriate since the disturbance does not decay rapidly outside of the vortex core. Therefore, for both linear and nonlinear PSE calculations, the non-reflecting boundary conditions of Thompson (1987) are applied in the farfield.

4.2.3 *Numerical Approach*

Numerical solution of the parabolized stability equation (4.34) requires discretization in both r and z directions. The discretization procedure is identical to the approach employed by Malik and Chang (1997) in their PSE study of a supersonic axisymmetric jet flow. That paper describes the intricacies of the numerical method in detail and therefore is not repeated here. For the present study the farfield boundary conditions were applied at $r_{\max} = 25$ which proved to be more than sufficient.

5. Results and Discussions

The governing equations are written in a general form valid for a perfect gas with variable properties. The temperature dependency of the fluid properties may be assumed to follow Sutherland's law or a simple power law variation. In the present work, for the quasi-cylindrical linear stability calculations, we obtained results with both constant and variable flow properties. We found the difference between the two sets of computations (in terms of the computed growth rate and frequency) to be less than 3%. Therefore, for quasi-cylindrical linear stability analysis only results obtained with constant flow properties are presented. For both linear and nonlinear PSE

computations Sutherland's law was assumed with a freestream static temperature of 130°K. Overall, for the Mach number range of interest these variations do not play a significant role. In addition, the second coefficient of viscosity is taken to be $\lambda = -2/3\mu$.

The parameter space affecting stability is multidimensional. We expect the stability characteristics of supersonic vortices to be dependent on q, δ, M, Re, Pr, α, ω, n, etc. For the problem to be tractable, some restriction on the values of these parameters is warranted. The Prandtl number Pr was set to 0.76 to match the Smart et. al experiment. The Reynolds number Re was chosen to be as in the Smart et. al experiment. Owing to the inviscid nature of the disturbance field, for moderate and high Re, the Reynolds number does not play a significant role. The vortex initial axial velocity deficit δ is 35% which matches the experiment. As in the case of incompressible vortices (see Lessen et. al 1974), the ratio q/δ determines stability or instability and therefore not much generality is lost by fixing δ.

Numerical computations of the mean flowfield allow one to vary parameters such as vortex strength q, Mach number M_∞, and Reynolds number Re independently. In this manner, important effects (e.g., compressibility, viscous, etc.) can be isolated. Smart et al.'s experiments were conducted at a nominal Mach number of 2.49. Although variation of different flow parameters may result in a computed flowfield that is unattainable in their tunnel, the realizability of the flowfield in some other tunnels is insured as long as numerically converged solutions are obtained. The computed profiles for q = 0.2, Re = 30000, and M_∞ = 2.49 at several axial locations are presented in Figures 1a–1g. The vortex initial axial velocity deficit is 35% for these cases. Note viscous diffusion only significantly affects axial velocity, static temperature, and density while tangential velocity and static pressure remain unaffected. Table I presents values and ranges of different parameters used in the present study.

5.1 Quasi-Cylindrical Linear Stability Analysis

The local linear stability analysis is very adept at determining the relevant parameter space, general trends, and overall stability characteristics. These computations also provide the guidance to conduct the nonlinear PSE calculations. We now proceed with presenting the computed results. The reference point to be established for this vortex is the case of $q = 0$. Here the flow is simply that of an axisymmetric wake which is only unstable with respect to instabilities having an azimuthal wave number of $n = \pm 1$.

The variation of growth rate versus frequency of the $n = 1$ mode for the wake is displayed in figure 2. The instability has a modest growth rate which does not change significantly as the wake evolves downstream. The growth rate curve has a peak value of 0.027 at the initial location which subsequently drops to 0.022 at a station 320 core radii downstream. The nondimensional frequency ω_r corresponding to $\omega_{i\,max}$ is 0.8. In contrast, the vortex with a small amount of swirl (q

= 0.1) is highly destabilized by the asymmetric $n = 1$ disturbance as shown in figure 3. Specifically, the growth rate curves depict a tripling effect when compared with the wake instability. In addition, there is nearly a 20% reduction in the instability's growth rate at $z = 320$ compared to the initial station $z = 0$. The effect of increased swirl on the $n = 1$ mode is displayed in figures 4–6. The instability's amplification factor peaks at $q = 0.2$ and there is a significant reduction in ω_i as the disturbance travels downstream. Increasing q beyond 0.2 has a stabilizing influence on the $n = 1$ mode. The growth rate for $q = 0.4$ is comparable to the values obtained for the wake disturbances (figure 2). At this q the $n = 1$ mode is unstable over a narrow band of frequencies. Moreover, the perturbation is stabilized rapidly as it moves in the axial direction and at a z location slightly greater than 70 becomes a stable mode.

Unlike the axisymmetric wake flow, the vortex is unstable with respect to higher azimuthal wave numbers. The amplification behavior of the $n = 2$ mode for values of $q = 0.1, 0.2, 0.3$, and 0.4 are shown in figures 7–10. At $q = 0.1$, the instability is growing at a lower rate than the $n = 1$ disturbances (figure 7). At $q = 0.2$, the growth rates for this mode become comparable to the $n = 1$ disturbance and are slightly lower only in the first few axial locations. On the other hand, the growth rate of the $n = 2$ mode virtually remains unchanged for large values of z. This behavior becomes more pronounced at higher swirl values. Thus, while the $n = 1$ disturbances may dominate the initial stages of the linear growth, it is the $n = 2$ modes that tend to dominate at farther locations downstream. Similar to the $n = 1$ perturbations, the growth rate for the $n = 2$ mode peaks at $q = 0.2$. Further increases in the swirl parameter provide a stabilizing effect up to a $q \approx 0.5$ where the vortex becomes totally stabilized with respect to this perturbation.

The vortex is also unstable with respect to larger azimuthal wavenumbers. We have mapped thoroughly the stability characteristics of the vortex for $n = 3$, and 4. Figure 11 displays the variation of ω_i vs the nondimensional frequency ω_r for the $n = 3$ mode at $q = 0.2$. Unlike the previous two modes, the maximum growth rate does not occur at the initial station. Rather, the instability attains its peak amplification rate at a downstream location of $z = 120$. Beyond this axial station the amplification rate diminishes at a very slow pace as the disturbance travels downstream. The growth rate for the $n = 4$ mode at a swirl ratio of $q = 0.2$ is shown in figure 12. The trends are similar to the $n = 3$ mode presented in the previous figure except this mode attains its peak growth rate even farther downstream at $z = 160$. The effect of increased rotation on these higher n modes is very similar to the $n = 2$ instability and therefore are omitted here. For our fixed Reynolds number of $Re = 30000$, the $n = 1$ mode attains the largest growth rate in the azimuthal wave number space. The absolute maximum growth rate is expected to shift to larger values of n if Re is increased.

For streamwise vortices, in addition to the primary unstable mode there are always higher modes of instability associated with each individual n. This is irrespective of azimuthal wave

number considered. As the Reynolds number is increased, the number of these higher modes tends to increase until in the limit of Re → ∞ there are an infinite number of unstable modes. Fortunately, the growth rates of these higher modes are much lower than those of the primary modes and therefore are less important.

The growth rate behavior of the first higher mode for the $n = 1$ instability at $q = 0.2$ is presented in figure 13. This particular mode displays a double hump peak growth rate. The second hump associated with the higher frequencies tends to stabilize much faster as the disturbance moves downstream. As mentioned above, overall the growth rate is significantly smaller than the primary mode (figure 4). The corresponding higher mode for the $n = 2$ instability is shown in figure 14. For the remainder of this report, we will omit the discussion on the higher modes.

5.1.1 *Viscous effects*

As discussed in the previous sections, the Reynolds number does not play a dominant role because an inviscid (centrifugal) mechanism is responsible for the instabilities. The effect of Reynolds number is even less important at the moderately high *Re* of most experiments. It is instructive, however, to show a sample computation where viscous effects are presented.

The inviscid nature of the helical unstable modes is shown in figure 15 where we have plotted the effect of Reynolds number on the $n = 1$ disturbances at two streamwise locations. For $Re < 10^2$ the instability is fully damped. As the Reynolds number is increased gradually, the primary mode is first destabilized and then after a period of rapid growth, its amplification factor ω_i asymptotes eventually to a constant level (inviscid limit). The second mode becomes destabilized once the Reynolds number is increased beyond $Re = 4,000$. The disturbance frequency, ω_r, for both modes remains fairly independent of the Reynolds number (not shown). The behavior of the $n = 2$, and 3 modes are essentially similar to that of the $n = 1$ perturbation, except that the high-Reynolds number behavior is shifted to higher Reynolds number. Based on these observed trends, we fixed the Reynolds number at the experimental value of 30,000 for the entire computational study.

5.1.2 *Compressibility effects*

The compressibility effects on the $n = 1$ mode for $q = 0.2$ are presented in figures 16–18. Three different Mach numbers $M_\infty = 1.6, 2,$ and 3 are considered. Results for $M_\infty = 2.49$ already were shown in figure 3. Increasing the Mach number has a stabilizing influence. At higher values of M_∞ there is a reduction in the growth rate of the disturbances. For example, at the location $z = 80$ the maximum growth rate for $M_\infty = 3.0$ shows nearly 40% drop relative to the peak growth rate at $M_\infty = 1.6$. Overall, this Mach number effect is consistent with the trends observed for free shear-layers without swirl.

5.2 Linear PSE

Using the parabolized stability equations, we now attempt to determine spatial evolution of the disturbance field. The linear PSE provides a quick way of mapping the underlying vortex stability characteristics and to isolate the effects of mean flow changes in the streamwise direction (non-parallel effects) on the disturbances. Once again the reference point for this vortex is the axisymmetric wake where $q = 0$.

The variation of the spatial growth rate $-\alpha_i$ vs frequency, for the $n = 1$ mode of the axisymmetric wake, at several streamwise locations is presented in figure 19. As in the case of the quasi-cylindrical analysis of the previous section, the instability maintains a nearly constant amplification rate along the streamwise direction. Similar curves for the $n = 1$ instability of the vortex at $q = 0.1$, 0.2, and 0.3 are plotted in figures 20a–20c. Initially, increasing the swirl parameter q is destabilizing and will provide higher growth rates up to $q = 0.2$. Beyond this point, rotation becomes a stabilizing force causing a lower growth rate for the instability. In addition, the growth rate diminishes much faster along the streamwise direction at higher q's (figure 20c). The corresponding plots for the azimuthal wave numbers $n = 2$, and 3 are shown in figures 21a–21c and 22a–22c respectively. The trends observed in these figures are identical to those described for the $n = 1$ instability. Overall, in the swirl parameter space, the absolute maximum growth rate occurs at $q = 0.2$ which corresponds to the values obtained from an analysis of Smart's et al (1994) experiment. Both $n = 1$ and $n = 2$ instability modes have comparable growth rates at this q with $n = 1$ being slightly higher. The value of q where this peak amplification occurs depends on the axial velocity deficit δ, which was chosen to be 0.35 to match the experiment. Obviously, changing δ would cause q to shift too. Nevertheless, the trends observed so far will re-emerge once a comparable ratio of q/δ is attained.

The eigenfunction variations across the vortex core for the $n = 1$, 2, and 3 modes are plotted in figures 23a–23c. The eigenfunctions were determined for frequencies corresponding to the respective instability maximum growth rates $-\alpha_{i\max}$. Furthermore, they are normalized with respect to the maximum axial velocity component, $w'_{\max}$. These helical disturbances are confined to the vortex core and lie very close to the axis of the vortex. In figure 23a, the $n = 1$ mode is the only mode with nonzero fluctuations on the vortex axis. This particular helical mode, usually called a flapping mode, plays a dominant role in the development of axisymmetric free-shear flows. For the $n \neq 0$ perturbations, the temperature fluctuation dominates. Figures 23a–23c show that as n is increased, the radial position where the eigenfunctions are centered also increases. In this respect, disturbances with relatively high azimuthal wave numbers may be regarded as becoming "ring" modes; that is, the perturbation's energy is concentrated in a narrow ring of fluid (thus the name "ring" mode) situated at the critical layer radial distance from the vortex axis. The pressure fluctuation is not plotted in figures 23a–23b for two reasons. First, the pressure

amplitude, based on the scale shown, is nearly zero. Second, the pressure decays very smoothly and has a nonoscillatory behavior as r becomes large, thus indicating that there is no energy radiation to farfield.

5.2.1 *Compressibility effects*

The variation of the growth rate $-\alpha_i$ vs frequency ω for the axisymmetric wake is presented in figure 24. Results were obtained for five distinct supersonic Mach numbers. The fully-developed-wake instability tends to be insensitive to the freestream Mach number. In contrast, the vortex disturbance field is quite sensitive to Mach number variations. Results for $n = 1, 2$, and 3 at $q = 0.2, z = 160$ are displayed in figures 25–27. Compared to the wake, vortex instabilities go through a significant reduction in their growth rate when the freestream Mach number is increased. There is also a noticeable reduction in the range of frequency where the instabilities are present. The severity of the compressibility effects is slightly more pronounced for the $n = 1$ mode as compared to the other two azimuthal wave numbers. This point is made more clear in figure 28 where the maximum amplification factor $-\alpha_{i,\max}$ is plotted vs Mach number. Notice at $M = 1.5$ the three disturbances have comparable growth rates. As the freestream M is increased, the maximum growth rate associated with the $n = 1$ disturbance (the curve with circles) diminishes at a faster rate than the corresponding curves for $n = 2$, and 3. There is a crossing between $n = 1$ and $n = 2$ that takes place at $M = 1.8$ while the crossing between $n = 2$ and 3 occurs at $M = 3.5$. As indicated earlier, the wake mode is virtually unaffected and remains nearly constant for the range of Mach number considered. Surprisingly, figure 28 suggests that for freestream Mach numbers greater than 4 there is a possibility that the growth rates associated with vortex instabilities will dip below that of an axisymmetric wake.

5.2.2 *Non-parallel effects*

The linear PSE formulation allows one to determine the effects of streamwise mean flow variation on the growth of the disturbance field. Unlike quasi-cylindrical flow (section 5.1), however, there is no unique streamwise wave number α in the nonparallel flow analysis. That is, depending on the path taken in r-z plane, one obtains a different rate of amplification. To circumvent this problem, in the nonparallel studies, the wave number can be designated as the "wave number based on a particular fluctuating quantity such as velocity, temperature or mass-flow rate." Usually the wave number is computed at the location in the shear layer where the flow fluctuations become maximum. For example, if we choose to compute the wave number α at the location where mass fluctuation peaks, α is obtained from the relation

$$\alpha(z) = \frac{1}{i(\rho w)_{max}} \left(\frac{\partial(\rho w)}{\partial z} \right)_{r=\bar{r}}$$ (5.1)

where $\bar{r}$ is the radical location of $(\rho w)_{max}$. Accordingly, the growth rate then is defined as

$$\Lambda = \text{Im ag} \left(\frac{i}{(\rho w)_{max}} \frac{\partial(\rho w)}{\partial z} \right).$$ (5.2)

The effect of the nonparallel mean flow on the $n = 1$ perturbation with $q = 0.2$ and $\omega = 1$ is shown in figure 29. We have chosen four different fluctuating quantities namely mass-flow rate, streamwise velocity, temperature, and kinetic energy to deduce the growth rates. In figure 29 the solid curve represents the quasi-cylindrical (parallel) flow analysis. Independent of the quantity considered, the computed nonparallel curves all follow the parallel curve and are virtually indistinguishable from it. The corresponding plots for $n = 2$, and 3 modes are shown in figures 30–31. For these azimuthal wave numbers the nonparallel curves show slightly smaller growth rates than the parallel flow curve. Overall the differences are not significant which suggests that nonparallel effects do not alter the stability characteristics of supersonic vortices.

5.3 Nonlinear PSE

The linear studies provided ample information to choose the most appropriate test cases. The mean flow conditions chosen for our study are $M_{\infty} = 2.49$, $Re = 30,000$, $Pr = 0.76$, $q = 0.2$ and $\delta = 0.35$. A possible scenario for laminar-turbulent transition is through interaction of the vortex with the first few helical modes. The initial growth of these disturbances will result in the emergence of organized large-scale structures. Through nonlinear interactions the helical modes generate other harmonics which lead to smaller scale structures and hence transition to turbulence.

For the present study, three cases were computed. For the first case, the vortex was perturbed by the helical mode $n = 1$ at a frequency $\omega = 1.0$. Because the Fourier expansion has the form $\exp(in\theta - im\omega t)$, we denote the corresponding mode as the (m, n) mode, hence the initial disturbances in the first case are associated with the (1, 1) mode. The second case involves the $n = 2$ mode which was introduced at a frequency of 1.3. This mode is designated (1, 2) with $\omega = 1.3$. The last case considered the modal interaction between $n = 1$, $n = 2$ and the vortex at $\omega = 1.3$. For this case the initial disturbances are the modes (1, 1) and (1, 2). For all three cases, the initial amplitude for the axial velocity perturbation was taken to be 0.1%. All the nonlinear computations were performed with expansions to $M = 5$ and $N = 5$ with M and N defined in Eq. 4.24.

5.3.1 *Case a: n=1 mode*

Figure 32 shows the streamwise evolution of the axial velocity fluctuation. Throughout the linear stage, the (1,1) mode dominates. The growth of the (1,1) mode follows the linear amplification up to $z \approx 28$; further downstream the growth rate departs from the linear solution and soon nonlinear saturation takes place. In the nonlinear stage the mean-flow distortion mode (0,0) generated by nonlinear interaction overtakes the (1,1) mode and rises to very large amplitudes (greater than 7%) before it too saturates. Prior to $z \approx 38$, the higher harmonics do not attain large enough amplitudes to be of any significance.

The various components of the mean-flow distortion mode (radial, tangential, and axial velocities and temperature) are plotted in figures 33a–33d. The radial velocity (figure 33a) is relatively small and does not change much in the streamwise direction. The tangential velocity (figure 33b) shows moderate growth. On the other hand both axial velocity and temperature (figures 33c–33d) show significant levels of distortion in the streamwise direction, in particular during the saturation stage. The axial velocity distortion tends to reduce the wake velocity deficit. Meanwhile, the temperature distortion mode reduces the temperature excess in the vortex core. The axial velocity contour plots in the r -z plane are shown in figure 34. Towards the end of the linear stage, at $z \approx 26$, the instability begins to modulate the vortex core, which results in the appearance of a large scale coherent structure. At the same location, the reduction in the wake velocity deficit starts to accelerate. The contour plots in the $r - \theta$ plane at $z = 1$, 28, and 38 are displayed in figures 35a–35c. In these figures the solid horizontal line is the branch cut in θ highlighting $\theta = 0$ line. At $z = 1$, the vortex is fully axisymmetric and the contours are concentric. At $z = 28$, the evolution of the disturbance has displaced the vortex core resulting in a slight eccentricity of the velocity contours. Near the end of saturation stage at $z = 38$, the core is displaced significantly and is no longer axisymmetric.

The disappearance of the axial velocity deficit in the core is best shown in figure 36 where we have plotted the iso-surface of velocity at a constant value of 0.74. Recall that the initial starting velocity has a 35% deficit. Figure 36 shows the initial twisting and shrinking of the core as the disturbance amplifies. During the saturation stage the wake is broken into little islands of low axial velocity until it finally disappears. For the sake of completeness, the velocity vectors in the cross plane at $z = 1$ and 39 are presented in figures 37a and 37b. The velocity vectors at the initial streamwise station show the vortex in its axisymmetric state while at $z = 39$ they show the complex asymmetric nature of the velocity field before breakdown occurs.

In figure 38 the contour plot for the temperature field in r-z plane is displayed. Similar to the velocity, the temperature field also clearly shows the undulation of the vortex core by the disturbance and subsequent generation of large-scale coherent structures. Notice the vortex starts with a temperature excess of 70%. During the final nonlinear stage the core temperature starts to

drop significantly in the streamwise direction. The hotter fluid shows up in smaller regions off of the centerline in the middle of the large structures. The corresponding contour plots in the $r-\theta$ plane at $z = 1$, 28, and 38 are presented in figures 39a–39c. Note how the initial axisymmetric temperature field becomes eccentric and finally develops into an asymmetric complex distorted field. At the $z = 38$ location, the circular core has been deformed into a strip structure which is identified by the contour levels F and E. Once again the breakdown of the hot vortex core is best shown by the iso-surface of temperature displayed in figure 40 for a constant level of 1.54. In this figure the growth of the instability and the resulting flapping of the core is very clear. As in the case of the velocity field (figure 36), during the final nonlinear stage the core breaks down into smaller segments.

Finally, the iso-surface of axial vorticity at a value of 0.078 is shown in figure 41. Initially, the axial vorticity resides entirely in a small region inside of the core. Due to the $1/r$ behavior of the tangential velocity, the flowfield surrounding the core is basically devoid of any axial vorticity. Figure 41 shows that axial vorticity follows a helical path in accordance with the instability wave form. Towards the beginning of the saturation stage, the shape of the surface starts to deviate from a clean, well-defined wave form. Due to nonlinear interactions, smaller scale structures begin to appear, indicating the end of the organized core.

5.3.2 *Case b:* n = 2 *mode*

The evolution of the axial velocity fluctuation for this helical mode is shown in figure 42. The forced (1,2) mode grows linearly up to $z = 34$ and is the dominant mode. The mean-flow distortion mode (0,0) begins with a much smaller amplitude but amplifies at a higher growth rate. Towards the beginning of the nonlinear stage, the (0,0) mode overtakes (1,2) while the latter mode goes through saturation. The mean flow distortion mode grows to a very large amplitude (more than 10%) before the computation was stopped due to lack of convergence. The higher harmonics never attain a large enough amplitude to be of any significance.

The evolution of various components of the mean flow distortion mode are presented in figures 43a–43d. As in the case of the $n = 1$ perturbation, the axial velocity and temperature fields show the highest levels of modification. Unlike $n = 1$ mode, however, the maximum distortion here occurs off the vortex centerline at a radial distance of $r = 0.25$ and 0.6.

The axial velocity contour plots in the r-z plane are displayed in figure 44. Unlike the $n = 1$ disturbance, the vortex core remains on the centerline albeit deformed in shape. The large scale structures inside the core appear at $z = 38$ and grow rapidly downstream. The wake velocity deficit also is reduced beyond this axial location but not as severely as in the case of the $n = 1$ disturbance. The velocity contours in the $r-\theta$ plane at $z = 30$ and 50 are shown in figures 45a and 45b. The contours at the initial station $z = 1$ are identical to those presented in figure 35a and therefore are

not repeated here. Figure 45a shows the contours towards the end of the linear growth. As mentioned above, the core is deformed but not displaced from the centerline $r = 0$. Downstream, due to nonlinear interaction, the core is severely deformed and develops into an s shape. In other words, the vortex core is being deformed into a two-lobed structure. This pattern becomes typical for disturbances with $n > 1$. That is, had we perturbed the vortex with $n = 3$ mode, the core would have deformed into three lobes and so on. Figure 46 shows the iso-surface of axial velocity at a value of 0.8. The appearance of the disturbance, its subsequent growth, and the development of a two-lobed core structure is clearly demonstrated in this figure. Notice towards the end of nonlinear saturation, the surface has become jagged which indicates the formation of smaller scale structures.

In figures 47–49 the corresponding results for the temperature field are plotted. The trends just described for the axial velocity not only are prevalent for the temperature field but actually show up in a more pronounced way. Finally, the iso-surface of axial vorticity at a value of 0.0795 is displayed in figure 50. The axial vorticity shows the presence of two large structures that grow in the downstream direction. The structures which behave as two distinct intertwined waves start out as thin vorticity sheets. As the disturbance amplifies downstream, the vorticity sheets grow in size and become thicker.

5.3.3 *Case c: Interaction of* n *= 1, and 2 Modes*

In this case both $n = 1$ and 2 modes were forced at a $\omega = 1.3$. The initial forcing level was kept to 0.1% for the axial velocity. Figure 51 presents the downstream evolution of various Fourier modes. The two forced modes (1,1) and (1,2) amplify in the linear stage with nearly identical growth rates and remain dominant. As the nonlinear stage sets in, the (1,1) mode saturates at a lower amplitude and after a distance of six core radii downstream, its amplitude starts to drop off. On the other hand, the (1,2) mode saturates and levels off at a slightly higher amplitude. Similar to the previous cases, the (0,0) mean flow distortion mode begins at a fairly small amplitude. Towards the end of the linear stage ($z = 28$), the distortion mode overtakes both forced modes and reaches very high amplitudes (greater than 10%). Also note the presence and importance of (0,1) and (1,0) modes in this case. Both of these harmonics attain higher amplitudes than the (1,1) forced mode in the nonlinear regime. The (1,0) mode represents an axisymmetric traveling wave.

Figures 52a–52d display the streamwise evolution of the mean flow distortion mode. Relatively speaking, the radial and tangential velocities remain small. As before, most of the distortion is related to the axial velocity and temperature fields with temperature modifications reaching very high levels. The axial velocity contour plots in the r-z plane are shown in figure 53. The undulation of the vortex core and wake deficit reduction begins near $z = 28$. Further downstream, the undulation loses its cohesiveness and other structures start to form. The contour

plots in the $r - \theta$ plane at two streamwise locations $z = 30$ and 40 are presented in figures 54a and 54b. Note that by $z = 40$, the vortex core has evolved into a complex structure that neither resembles the $n = 1$ mode eccentric shape (figure 35c) nor does it have the s shape feature of the $n = 2$ mode (figure 45b). The above point is made more clear in figure 55 where we have plotted the iso-surface of axial velocity at a value of 0.74. The shape of the surface indicates that neither of the two forced modes (1,1) and (1,2) dominate the evolution of axial velocity.

The temperature contours in the r-z plane is shown in figure 56. The growth of instability waves on the vortex core and subsequent formation and manifestation of large scale coherent structures is more evident in this figure than in figure 53. The contour plots in the $r - \theta$ plane are displayed in figures 57a and 57b. At $z = 30$, the hotter fluid in the core has been displaced off the centerline and is deformed into a crescent shape. At $z = 40$, the hotter fluid region is deformed even more and resides farther away from the centerline. In addition, multiple other regions containing warmer fluid have appeared. The corresponding iso-surface for the temperature is shown in figure 58. Contrary to the axial velocity iso-surface (figure 55), the temperature field shows a remarkable resemblance to the iso-surface of the $n = 1$ helical mode (figure 40). The distortion of the vortex core into a corkscrew figure is apparent. Also apparent is the breakdown of the core in the nonlinear stage into smaller segments of hotter fluid.

In figure 59 we have plotted the iso-surface of axial vorticity. In the linear stage, the distortion of the vorticity surface initially follows a path similar to that observed for the $n = 1$ disturbance (figure 41). In the nonlinear stage, however, the interaction between the two forced modes has altered the surface somewhat with the smaller scale features being more prominent.

6.   Conclusions

Quasi-cylindrical linear stability analysis was used to thoroughly map the stability characteristics of supersonic streamwise vortices. Important trends such as viscous and compressibility effects were studied. Based on linear analysis, the unstable disturbances were found to be inviscid in nature. Except for relatively low Reynolds numbers, viscous forces were found to be unimportant. In contrast, compressibility manifests itself as a stabilizing force. Increasing the Mach number significantly suppressed the growth rate of the helical unstable modes. The reduction was more pronounced for the first helical mode $n = 1$.

Non-parallel and nonlinear effects on the evolution of the disturbance field were studied using linear and nonlinear Parabolized Stability Equations (PSE) formulations. Streamwise mean flow variation was determined to have no significant effect on the amplification of the instabilities. For the nonlinear analysis, three distinct cases namely a) $n = 1$ mode, b) $n = 2$ mode, and c) $n = 1$, and 2 modal interaction were considered. In all three cases, nonlinear growth of the disturbance field resulted in the appearance of coherent large scale motion and significant mean

flow distortion in the axial velocity and temperature fields. The resulting mean flow modifications tend to reduce the vortex axial velocity deficit and temperature excess in the core. The disappearance of axial velocity deficit has a significant implication on the vortex stability. Based on past and present investigations, the presence of unstable modes in the vortex core is determined almost exclusively by the ratio of the swirl parameter q to the velocity deficit (or excess) δ. The present PSE analysis suggests that during nonlinear evolution of unstable disturbances, δ is reduced while q remains unaffected. This tends to increase q/δ ratio. The apparent increase in the swirl level provides a strong stabilizing force which will revert the vortex core back towards stability and a laminar state. This result seems to support conclusions drawn by Ragab and Sreedhar (1995) from their large-eddy simulation of incompressible streamwise vortices.

Relevant References

Ash, R. L. and Khorrami, M. R., 1995 "Vortex stability," Chapter 8 in Fluid Vortices (editor Sheldon I. Green), Kluwer Academic Publishers.

Batchelor, G. K., 1964 "Axial flow in the trailing line vortices," *J. Fluid Mech.*, Vol. 20, 645–658.

Bertolotti, F. P., 1991 "Compressible boundary layer stability analyzed with the PSE equations," AIAA Paper 91–1637.

Bertolotti, F. P., Herbert, Th. and Spalart, P. R., 1992 "Linear and nonlinear stability of the Blasius boundary layer," *J. Fluid Mech.* **242**, 441–447.

Broadbent, E. G. and Moore, D. W., 1979 "Acoustic destabilization of vortices," *Proc. R. Soc. Lond.*, Vol. 290, 353–371.

Broadbent, E. G., 1984 "Stability of a compressible two-dimensional vortex under a three-dimensional perturbation," *Proc. R. Soc. Lond.*, Vol. A392, 279–299.

Brown, G. L. and Roshko, A., 1974 "On density effects and large structure in turbulent mixing layers," *J. Fluid Mech.*, Vol. 64, 775–816.

Cattafesta, L. N. III, 1992, "An experimental investigation of shock-wave/vortex interaction," Ph.D. Dissertation, The Pennsylvania State University, Dept. of Mechanical Engineering, University Park, PA.

Chan, W. M., Shariff, K., and Pulliam, T. H., 1993 "Instabilities of two-dimensional compressible vortices," *J. Fluid Mech.*, Vol. 253, 173–209.

Chang, C. -L., Malik, M. R., 1994 "Oblique-mode breakdown and secondary instability in supersonic boundary layers," *J. Fluid Mech.* **273**, 323–359.

Chang, C. -L., Malik, M. R., Erlebacher, G. and Hussaini, M. Y., 1991 "Compressible stability of growing boundary layers using parabolized stability equations," AIAA Paper 91–1636.

Crow, S. C. and Champagne, F. H., 1971 "Orderly structure in jet turbulence," *J. Fluid Mech.*, Vol. 48, 547–591.

Cutler, A. D. and Levey, B. S., 1991 "Vortex breakdown in a supersonic jet," AIAA Paper 91–1815.

Cutler, A. D., Levey, B. S., and Kraus, D. K., 1993 "An experimental investigation of supersonic swirling jets," AIAA Paper 93–2922.

Eckert, E. R. G. and Hartnett, J. P., 1955 "Experimental study of the velocity and temperature distribution in a high velocity vortex type flow," University of Minnesota Heat Transfer Laboratory Technical Report No. 6, September.

Gans, R. F., 1975 "On the stability of shear flow in a rotating gas," *J. Fluid Mech.*, Vol. 68, 403–412.

Herbert, Th., 1991 "Boundary-layer transition -- Analysis and prediction revisited," AIAA Paper 91–0737.

Howard, L. N. and Gupta, A. S., 1962 "On the hydrodynamic and hydromagnetic stability of swirling flows," *J. Fluid Mech.*, Vol. 14, 463–476.

Howard, L. N., 1973 "On the stability of compressible swirling flow," *Stud. Appl. Math.*, Vol. LII, 39–43.

Hultgren, L. S., 1988 "Stability of swirling gas flows," *Phys. Fluids*, Vol. 31, 1872–1876.

Khorrami, M. R., 1991a "Stability of a compressible swirling jet," AIAA Paper 91–1770.

Khorrami, M. R., 1991b "On the viscous modes of instability of a trailing line vortex," *J. Fluid Mech.*, Vol. 225, 197–212.

Khorrami, M. R., 1991c "A Chebyshev spectral collocation method using a staggered grid for the stability of cylindrical flows," *Int. J. Num. Methods Fluids*, Vol. 12, 825–833.

Khorrami, M. R., 1995 "Stability of a compressible axisymmetric swirling jet," *AIAA J.*, Vol. 33, 650–658.

Lalas, D. P., 1975 "The 'Richardson' criterion for compressible swirling flows," *J. Fluid Mech.*, Vol. 69, 65–72.

Lay, J. E., 1959a "An experimental and analytical study of vortex-flow temperature separation by superposition of spiral and axial flows: Part 1," *J. Heat Trans.*, August, 202–212.

Lay, J. E., 1959b "An experimental and analytical study of vortex-flow temperature separation by superposition of spiral and axial flow: Part 2," *J. Heat Trans.*, August, 213–222.

Leibovich, S., 1984 "Vortex stability and breakdown: survey and extension," *AIAA J.*, Vol. 22, 1192–1206.

Lessen, M., Singh, P. J. and Paillet, F., 1974 "The stability of a trailing line vortex. Part 1. inviscid theory," *J. Fluid Mech.*, Vol. 63, 753–763.

Macaraeg, M. G., Streett, C. L., and Hussaini, M. Y., 1988 "A spectral collocation solution to the compressible stability eigenvalue problem," NASA Technical Paper 2858.

Malik, M. R. and Chang, C. -L., 1997 "PSE applied to supersonic jet instability," AIAA Paper 97–0758.

Mankbadi, R. R., 1992 "Dynamics and control of coherent structure in turbulent jets," Applied Mechanics Reviews, Vol. 45, 219–248.

Mayer, E. W. and Powell, K. G., 1992a "Viscous and inviscid instabilities of a trailing vortex," *J. Fluid Mech.*, Vol. 245, 91–114.

Mayer, E. W. and Powell, K. G., 1992b "Similarity solutions for viscous vortex cores," *J. Fluid Mech.*, Vol. 238, 487–507.

Naughton, J., Cattafesta, L. N., and Settles, G., 1989 "An experimental study of the effect of streamwise vorticity on supersonic mixing enhancement," AIAA Paper 89–2456.

Ragab, S. and Sreedhar, M., 1995 "Numerical simulation of vortices with axial velocity deficits," *Phys. Fluids*, Vol. 7, No. 3, 549–558.

Smart, M. K., Kalkhoran, I. M., and Bentson, J., 1994 "Measurements of supersonic sing tip vortices," AIAA Paper 94–2576.

Stott, J. A. K. and Duck, P. W., 1994 "The stability of a trailing-line vortex in compressible flow," *J. Fluid Mech.*, Vol. 269, 323–351.

Thompson, K. W., 1987 "Time dependent boundary conditions for hyperbolic systems," *J. Comput. Phys.* **68**, 1–24.

Table I. Flow conditions and parameters used in the present study.

Free-stream static temperature, η_∞	$130°$ K
Free-stream Reynolds number, $Re = W_\infty r_0 / v_\infty$	$\approx 30{,}000$
Free-stream Mach number, $M_\infty = W_\infty / a_\infty$	$1.5 \leq M_\infty \leq 3.5$
Prandtl number, $Pr = v_\infty Cp / \kappa_\infty$	0.76
Swirl parameter, q	$0 \leq q \leq 0.4$
Axial velocity deficit, δ	0.35
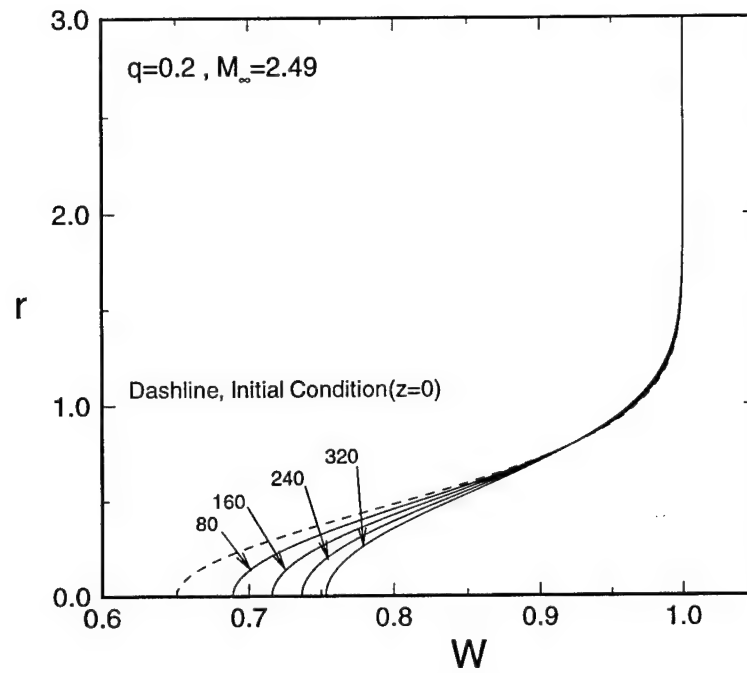
(a) axial velocity vs. radial distance

Fig. 1.   Evolution of the mean flowfield in the streamwise direction using Smart et al.'s (1994)
experimental data as the initial condition.
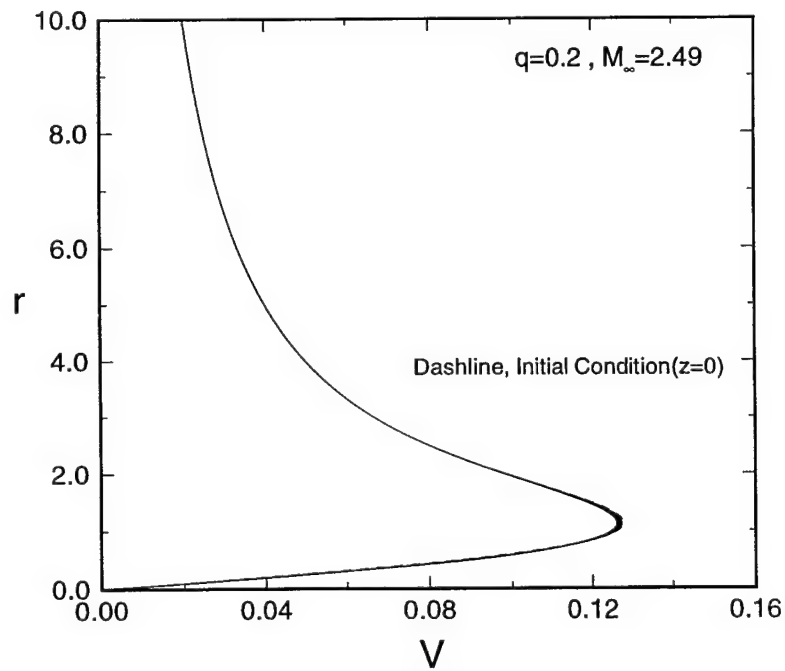
Fig. 1b. Tangential velocity.
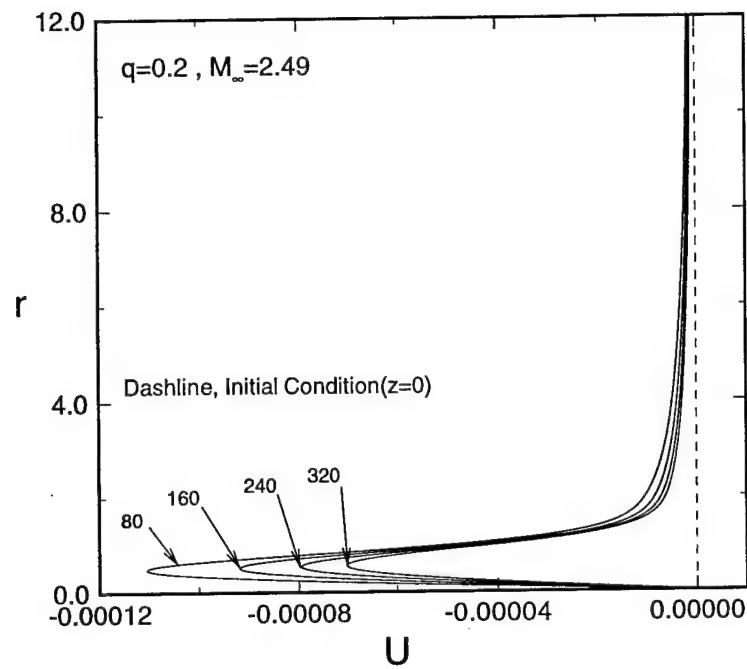
Fig. 1c. Radial velocity.
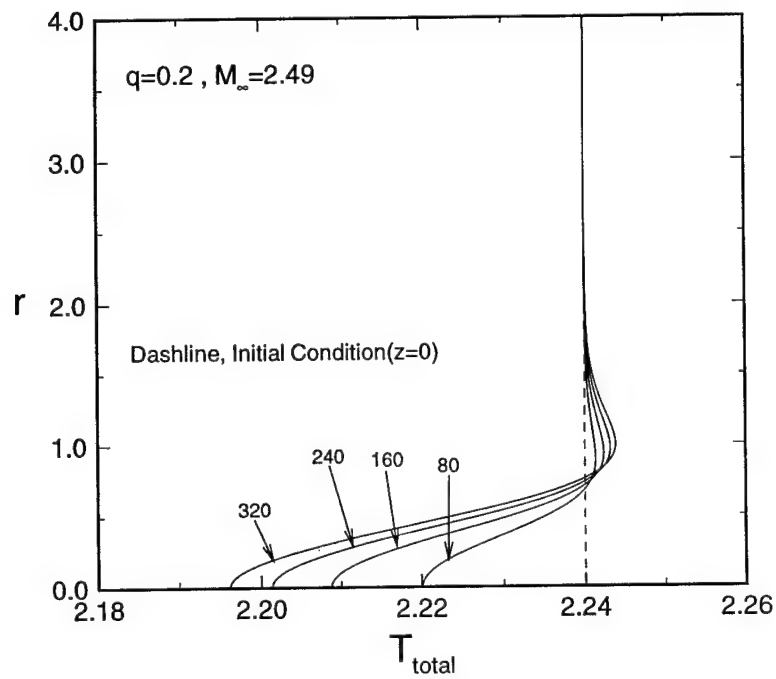
Fig. 1d. Total temperature.
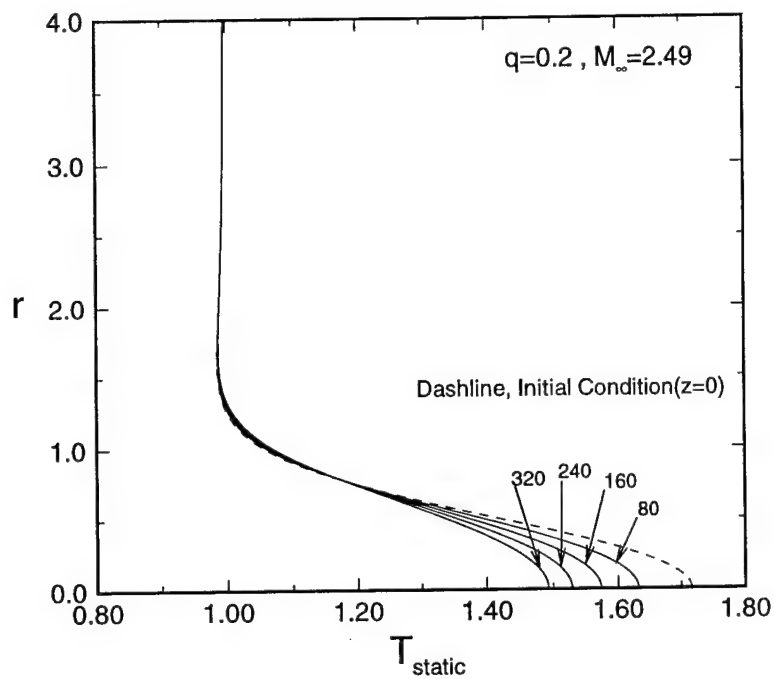
Fig. 1e. Static temperature.
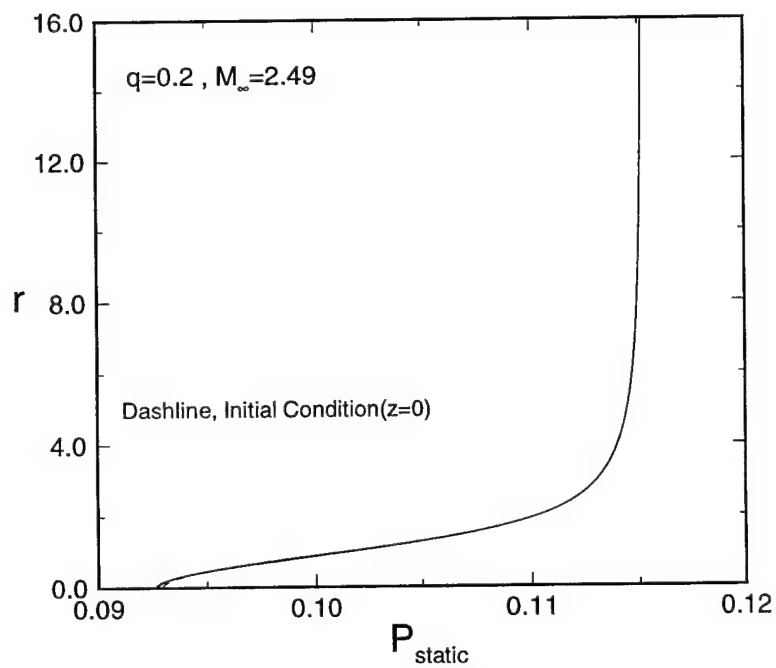
Fig. 1f. Static pressure.
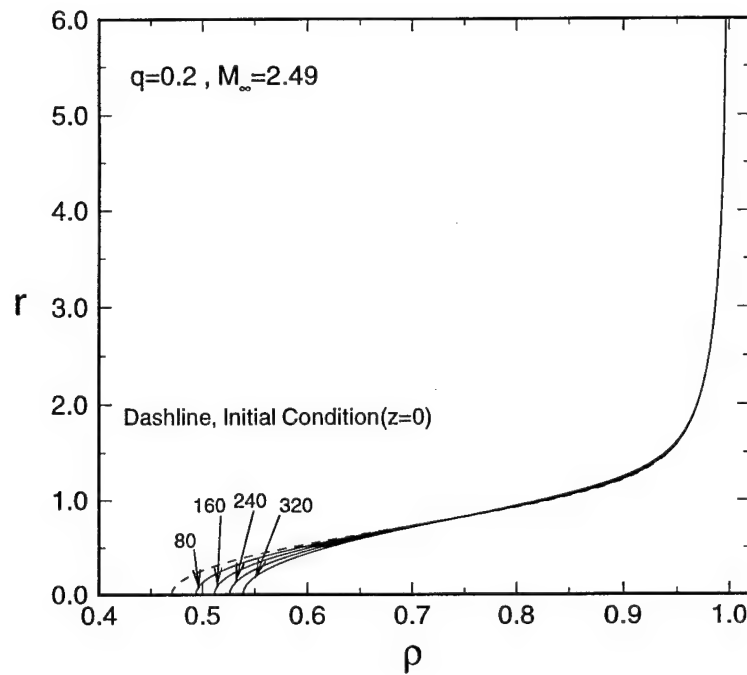
Fig. 1g. Density.
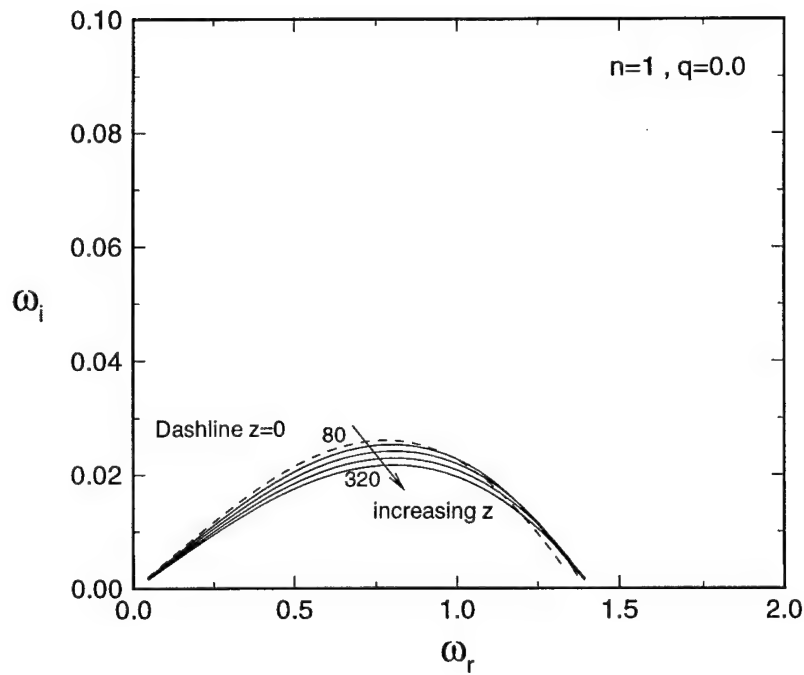
Fig. 2. Variation of the perturbation growth rate vs. frequency for the axisymmetric wake flow with $M_\infty = 2.49$, $Pr = 0.76$, and $Re = 3\times10^4$.
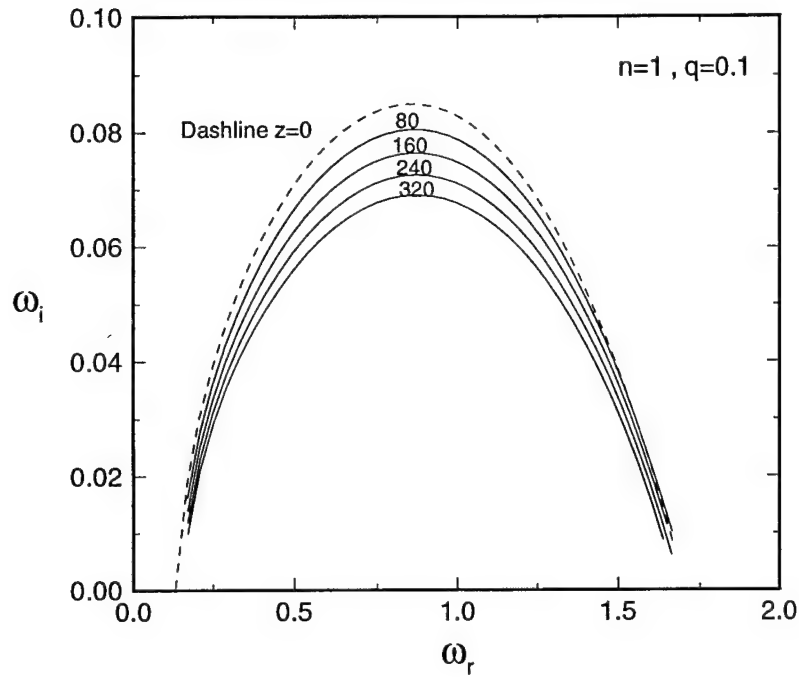
Fig. 3.   Variation of the vortex instability growth rate vs. frequency with $M_\infty = 2.49$, $Pr = 0.76$, and $Re = 3 \times 10^4$.
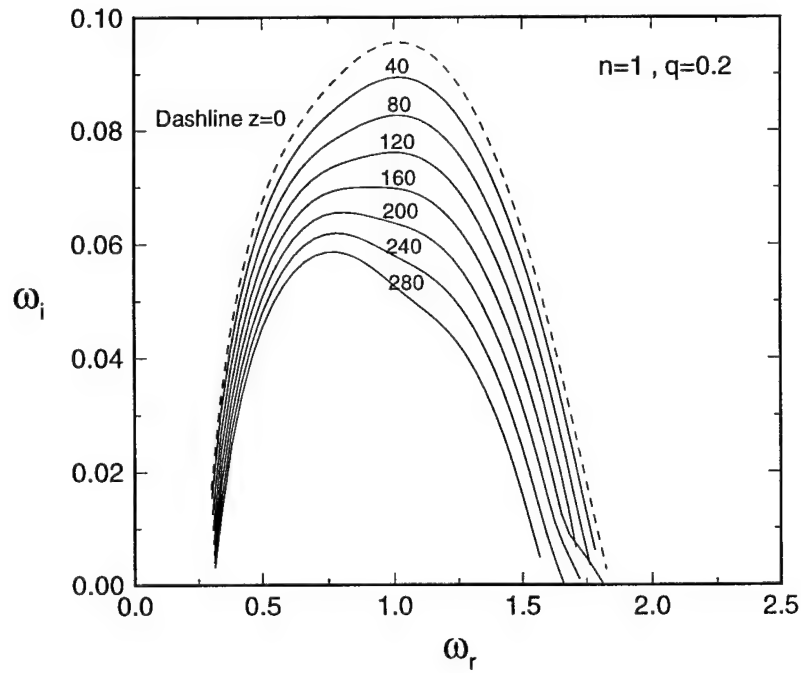
Fig. 4.   Variation of the vortex instability growth rate vs. frequency for $M_\infty = 2.49$, $Pr = 0.76$, and $Re = 3 \times 10^4$.
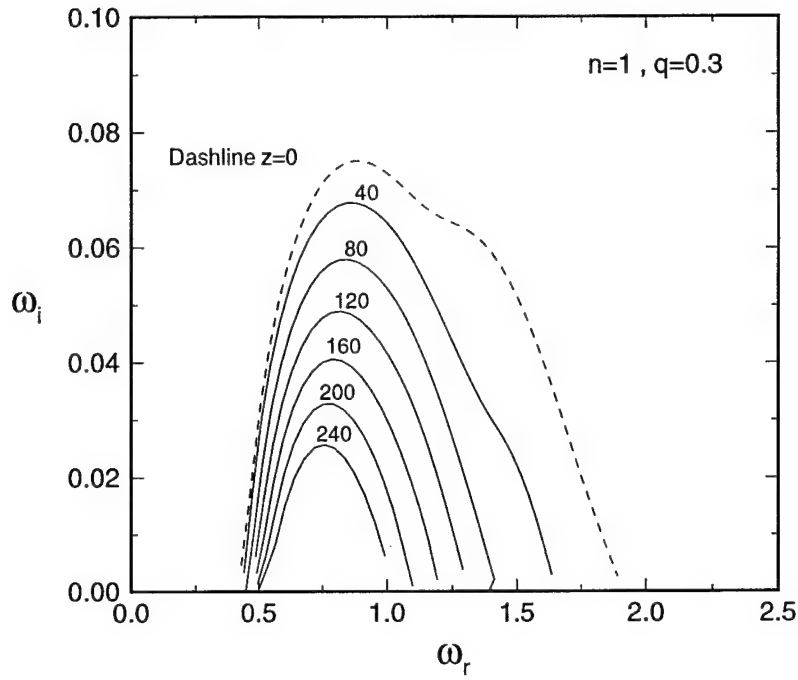
Fig. 5.   Variation of the vortex instability growth rate vs. frequency for $M_\infty = 2.49$, $Pr = 0.76$, and $Re = 3 \times 10^4$.
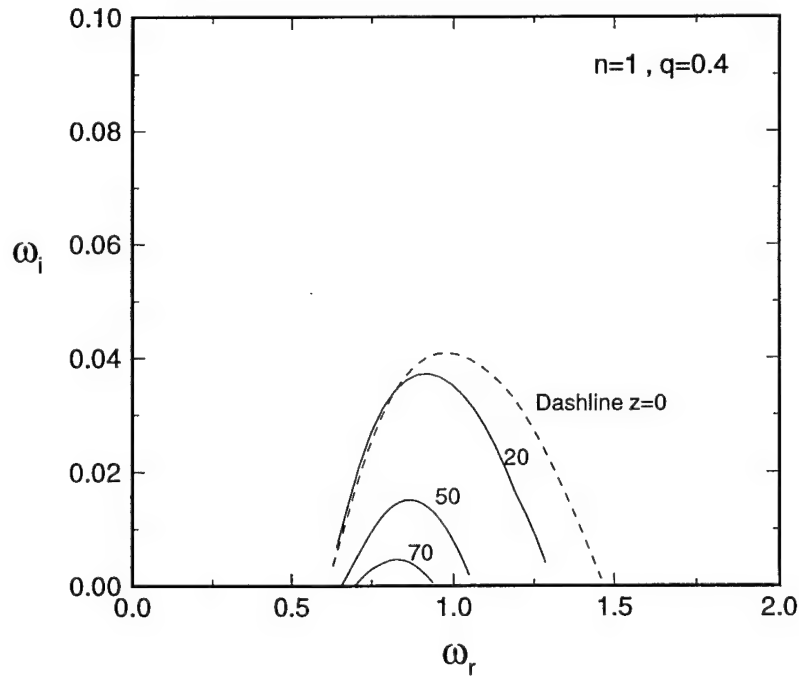
Fig. 6.   Variation of the vortex instability growth rate vs. frequency for $M_\infty = 2.49$, $Pr = 0.76$, and $Re = 3 \times 10^4$.

41
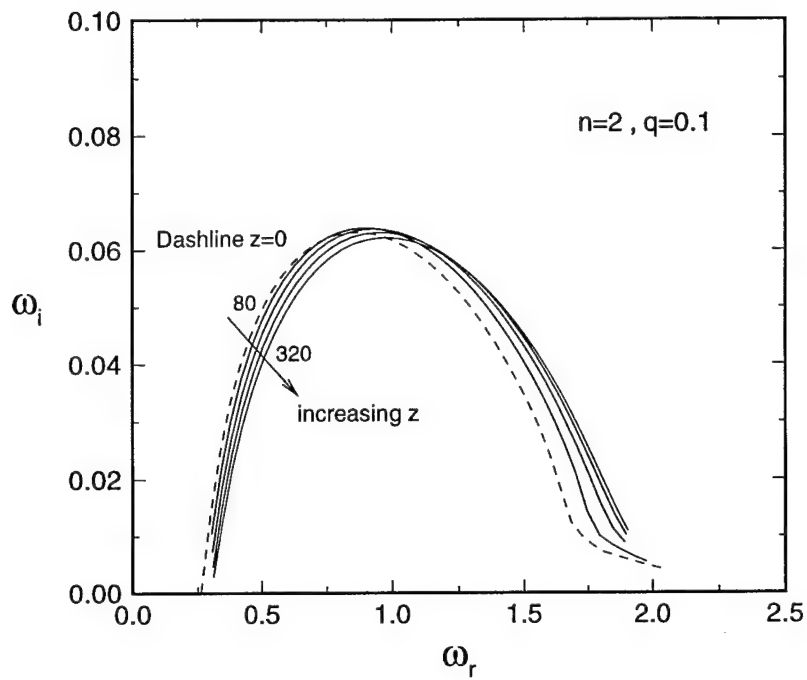
Fig. 7.   Variation of the vortex instability growth rate vs. frequency for $M_\infty = 2.49$, $Pr = 0.76$, and $Re = 3 \times 10^4$.
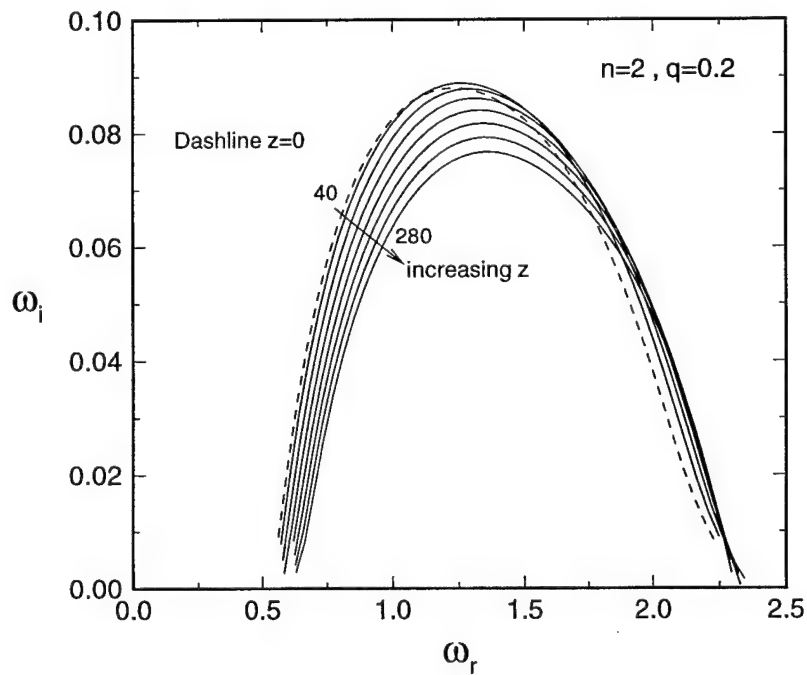
Fig. 8.   Variation of the vortex instability growth rate vs. frequency for $M_\infty = 2.49$, $Pr = 0.76$, and $Re = 3 \times 10^4$.
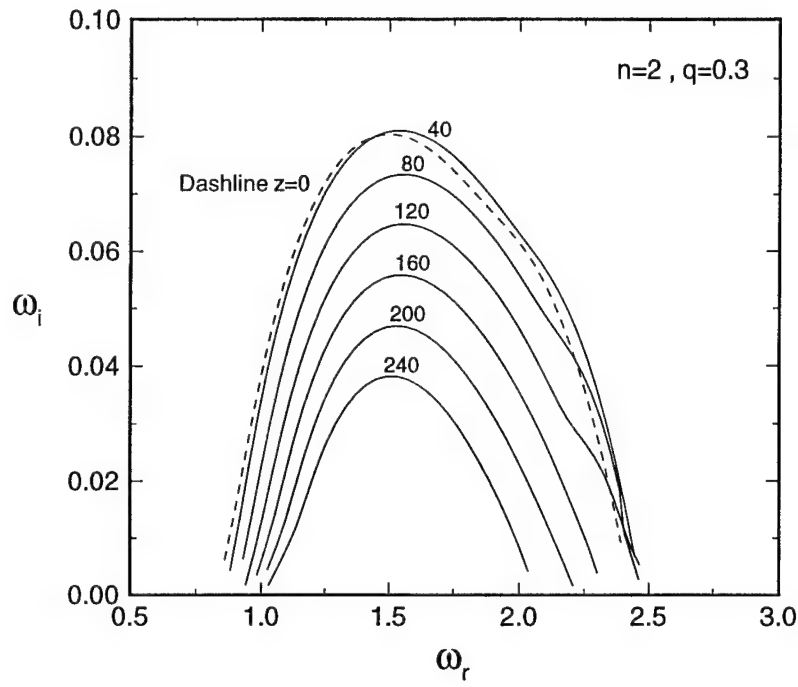
Fig. 9.   Variation of the vortex instability growth rate vs. frequency for $M_\infty = 2.49$, $Pr = 0.76$, and $Re = 3 \times 10^4$.
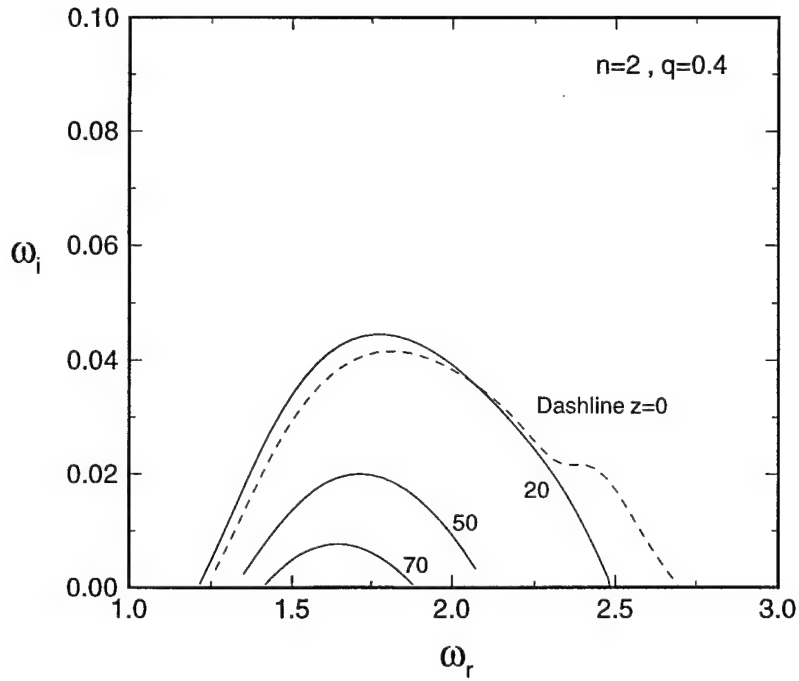
Fig. 10.   Variation of the vortex instability growth rate vs. frequency for $M_\infty = 2.49$, $Pr = 0.76$, and $Re = 3 \times 10^4$.
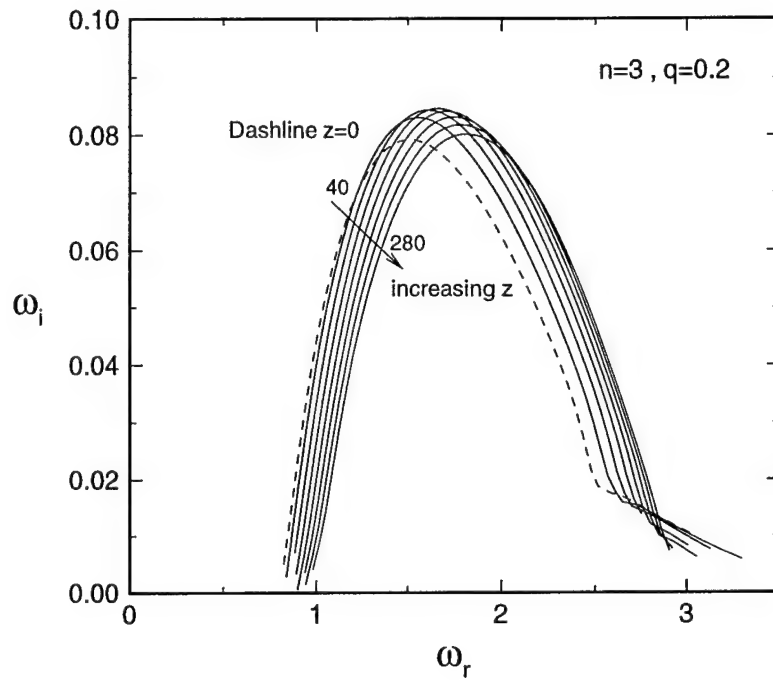
Fig. 11.   Variation of the vortex instability growth rate vs. frequency for $M_\infty = 2.49$, $Pr = 0.76$, and $Re = 3 \times 10^4$.
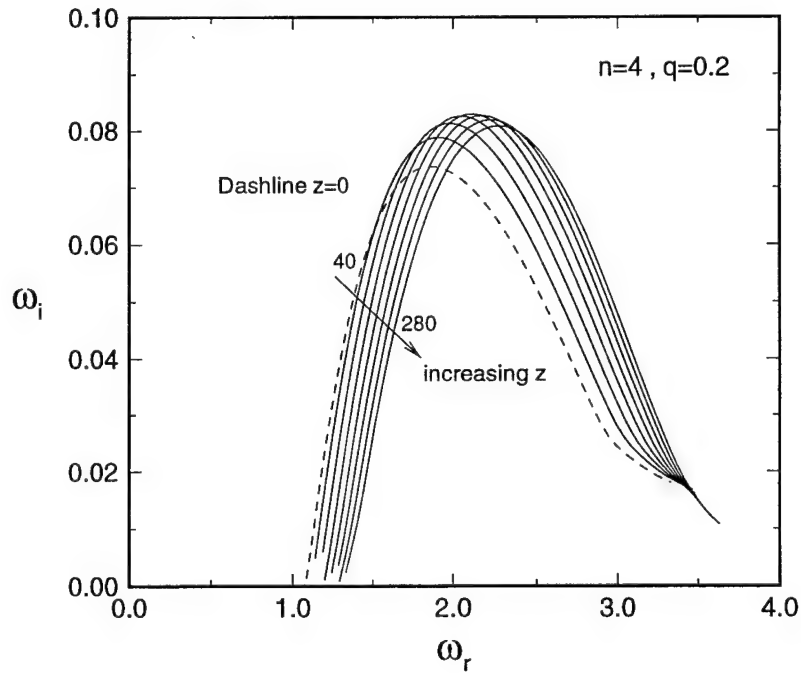
Fig. 12.   Variation of the vortex instability growth rate vs. frequency for $M_\infty = 2.49$, $Pr = 0.76$, and $Re = 3 \times 10^4$.
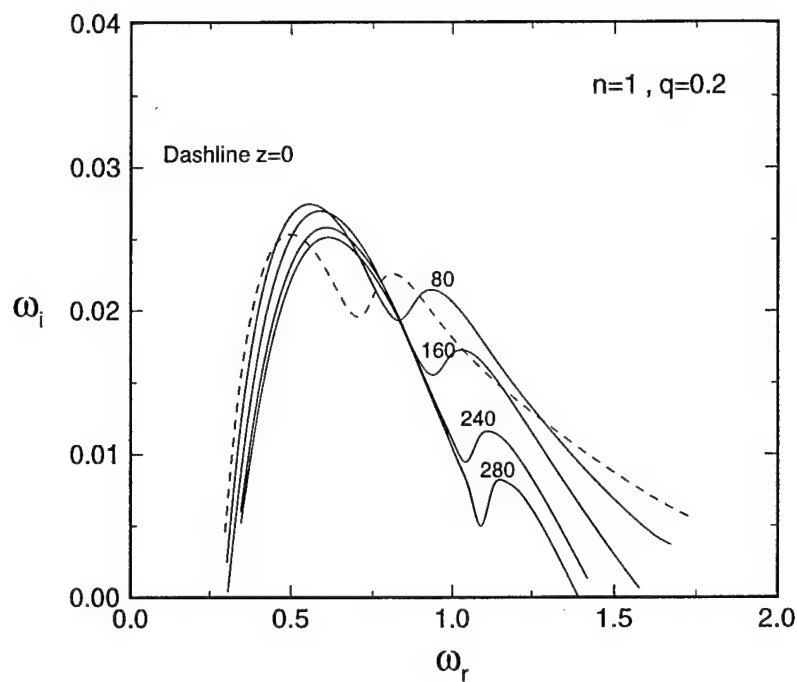
Fig. 13.   Growth rate behavior of higher unstable mode vs. frequency for $M_\infty = 2.49$, $Pr = 0.76$, and $Re = 3 \times 10^4$.
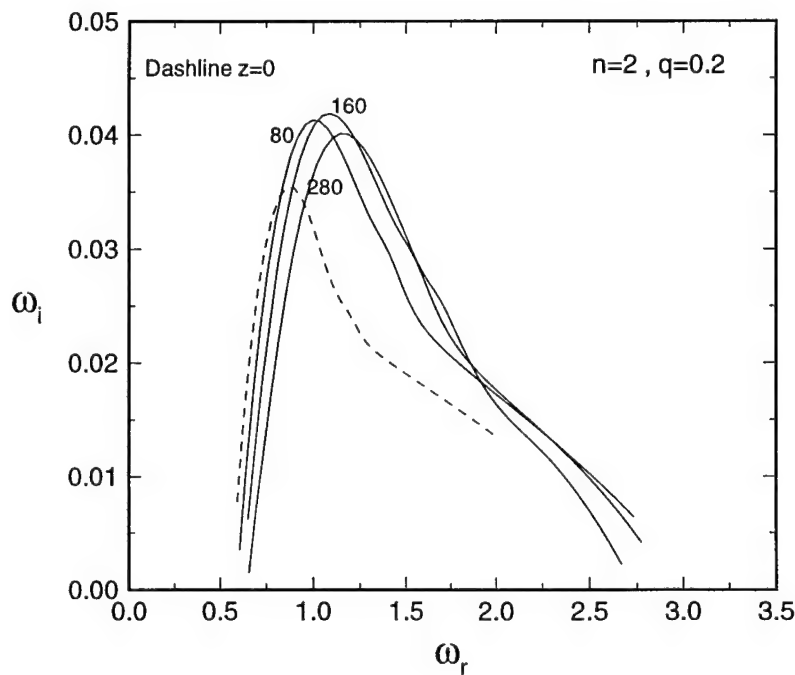
Fig. 14.   Growth rate behavior of higher unstable mode vs. frequency for $M_\infty = 2.49$, $Pr = 0.76$, and $Re = 3 \times 10^4$.
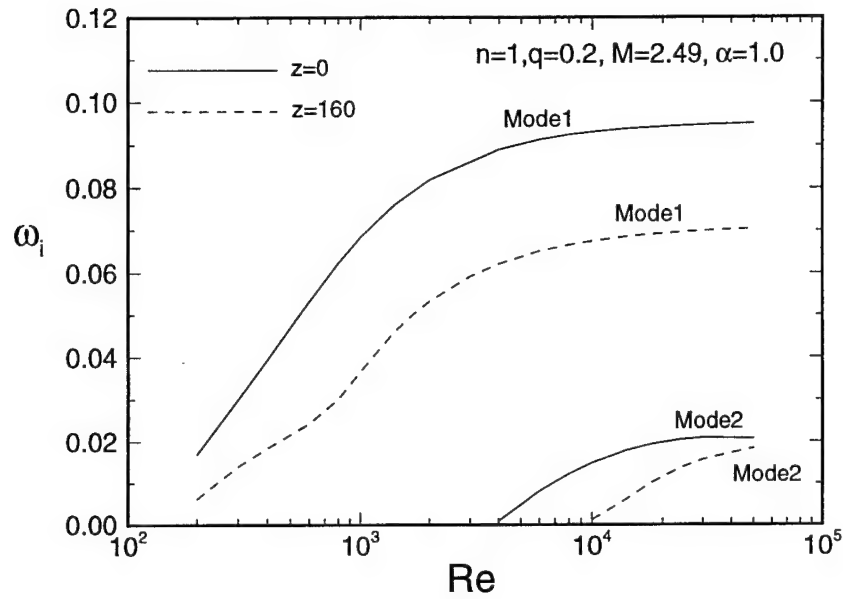
Fig. 15.   The effect of increasing the Reynolds number on the growth rate of the $n = 1$ unstable helical mode.
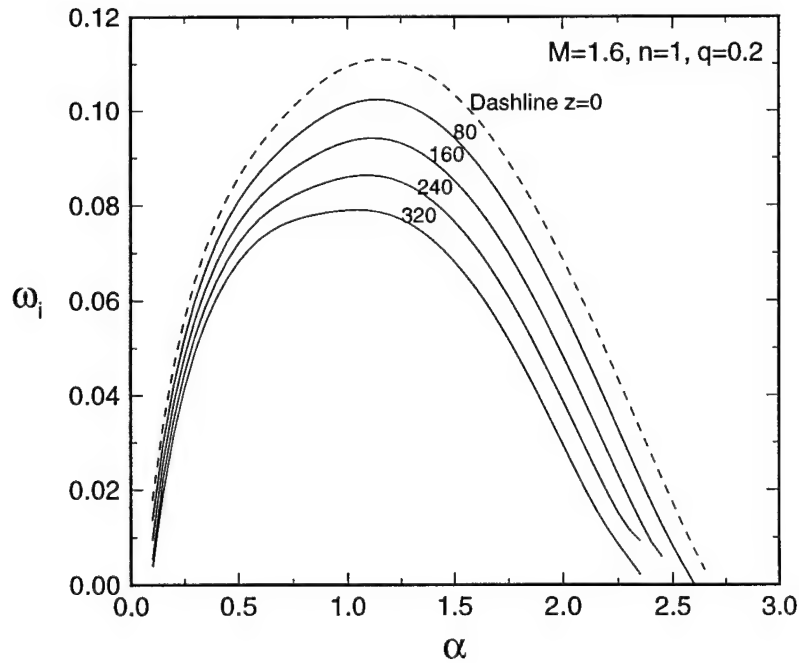
Fig. 16.   Variation of the vortex instability growth rate vs. frequency with $Pr = 0.76$ and $Re = 3\times10^4$.
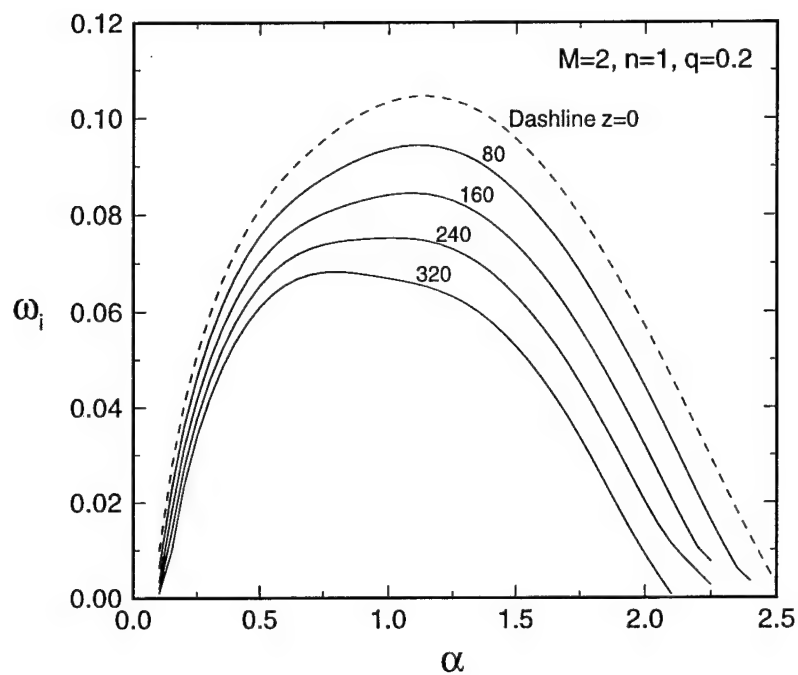
Fig. 17.   Variation of the vortex instability growth rate vs. frequency with $Pr = 0.76$ and $Re = 3 \times 10^4$.
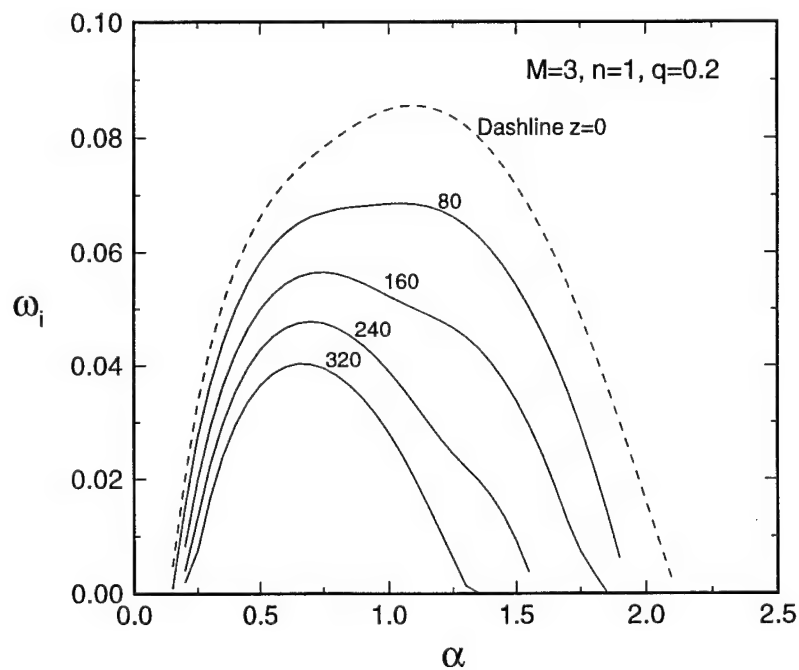
Fig. 18.   Variation of the vortex instability growth rate vs. frequency with $Pr = 0.76$ and $Re = 3 \times 10^4$.
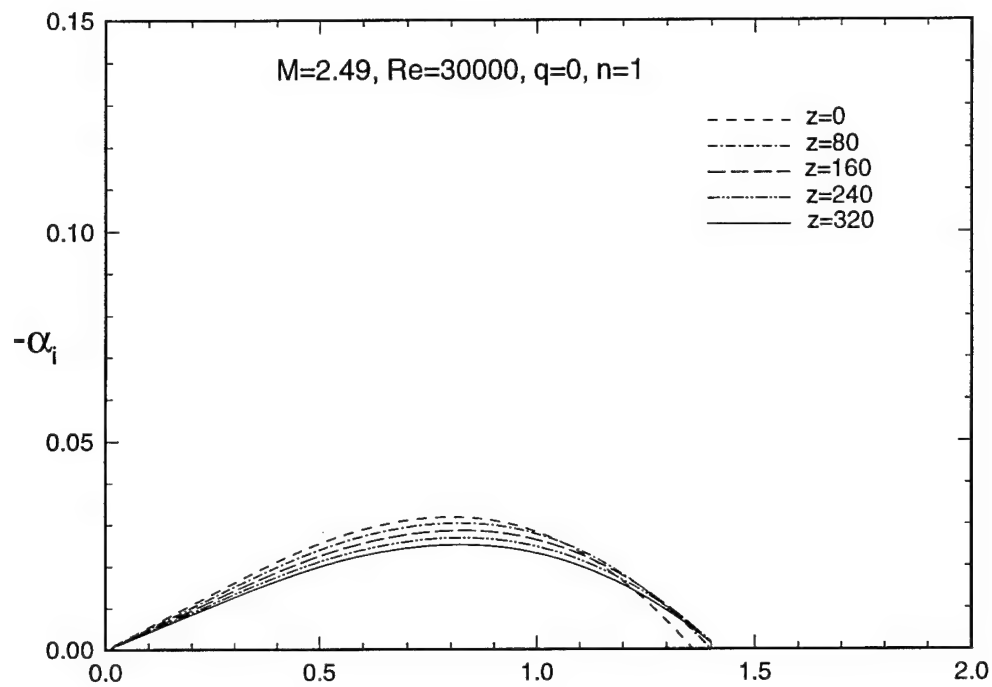
Fig. 19.   Variation of the disturbance spatial growth rate vs. frequency for the axisymmetric wake flow.
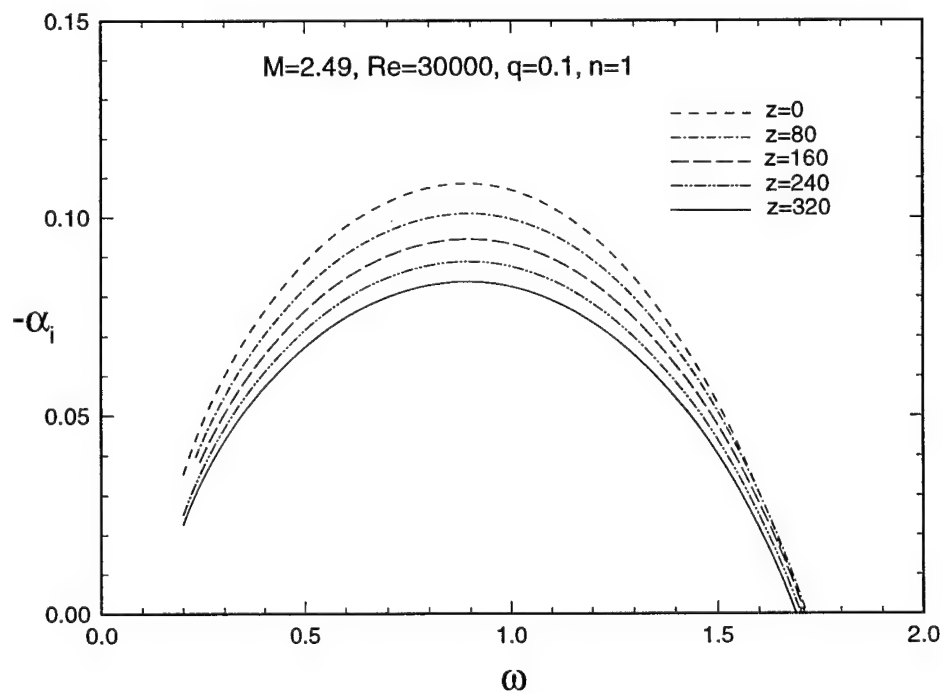
(a) Low swirl

Fig. 20.   Variation of the spatial growth rate of the first helical mode vs. frequency for different values of swirl parameter q.
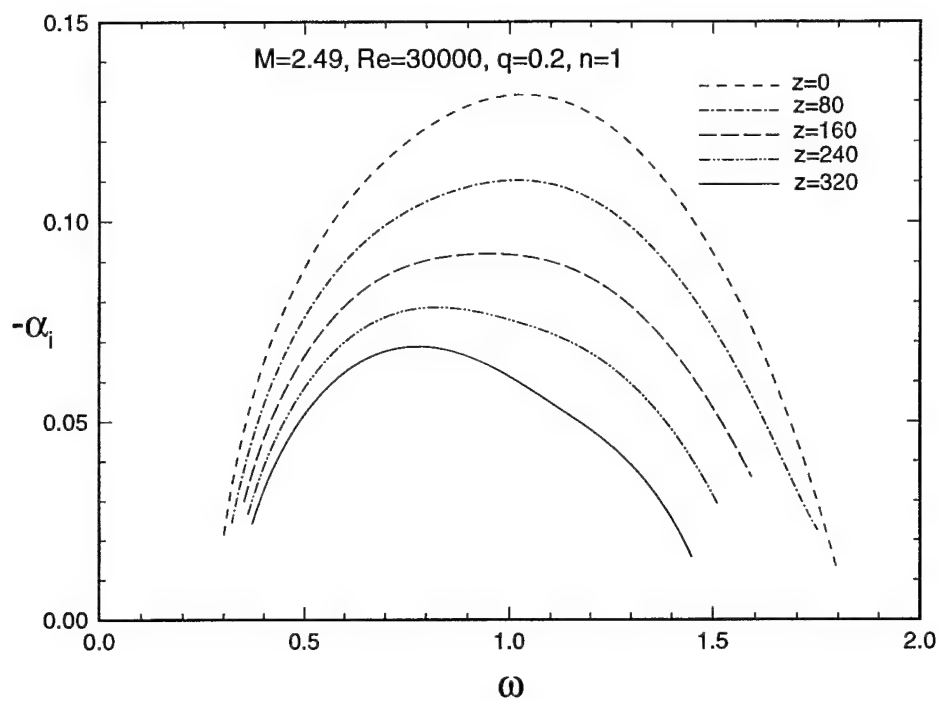
Fig. 20b.   Moderate swirl.
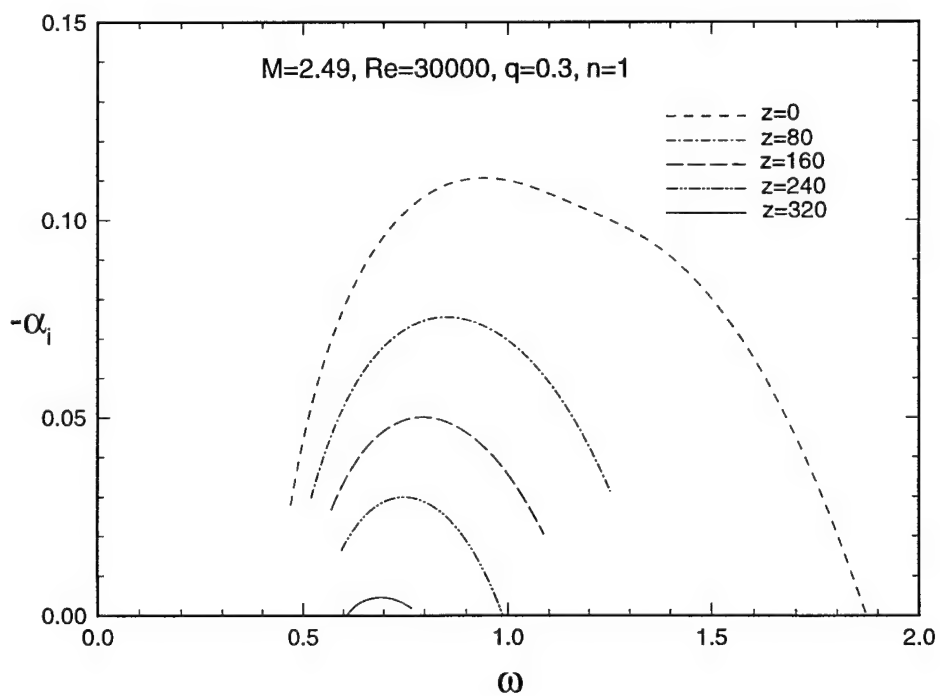
Fig. 20c.   High swirl.
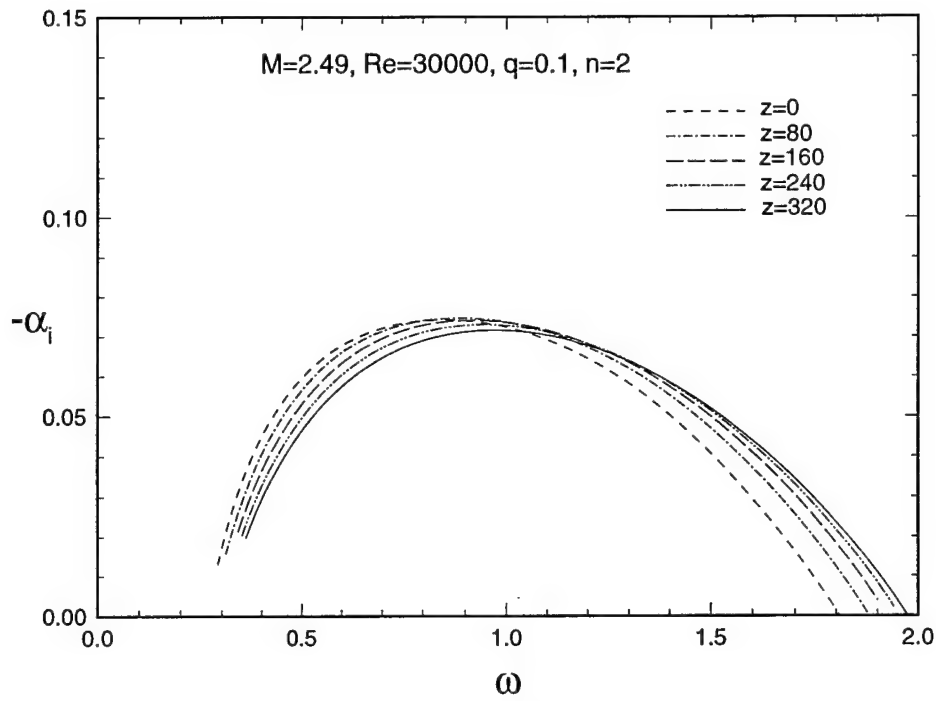
(a) Low swirl

Fig. 21.   Variation of the spatial growth rate of the second helical mode vs. frequency for different values of swirl parameter q.
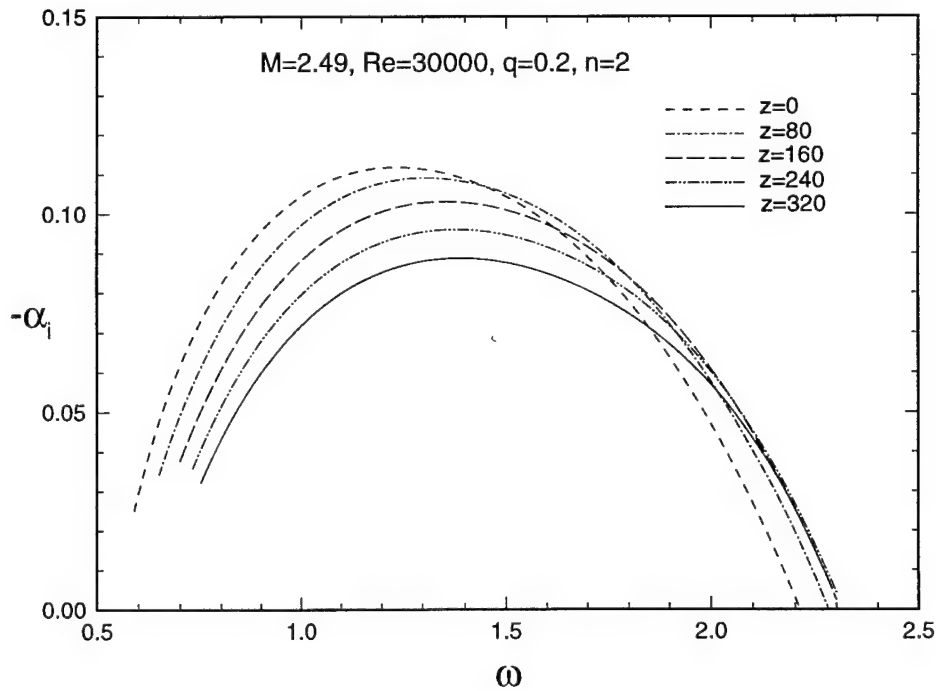
Fig. 21b.   Moderate swirl
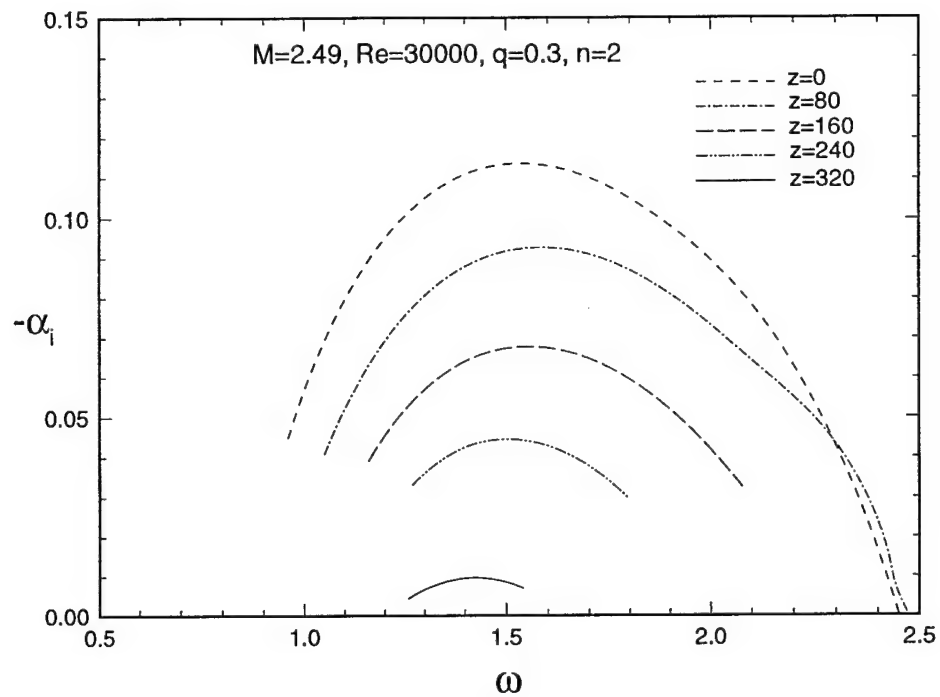
Fig. 21c. High swirl
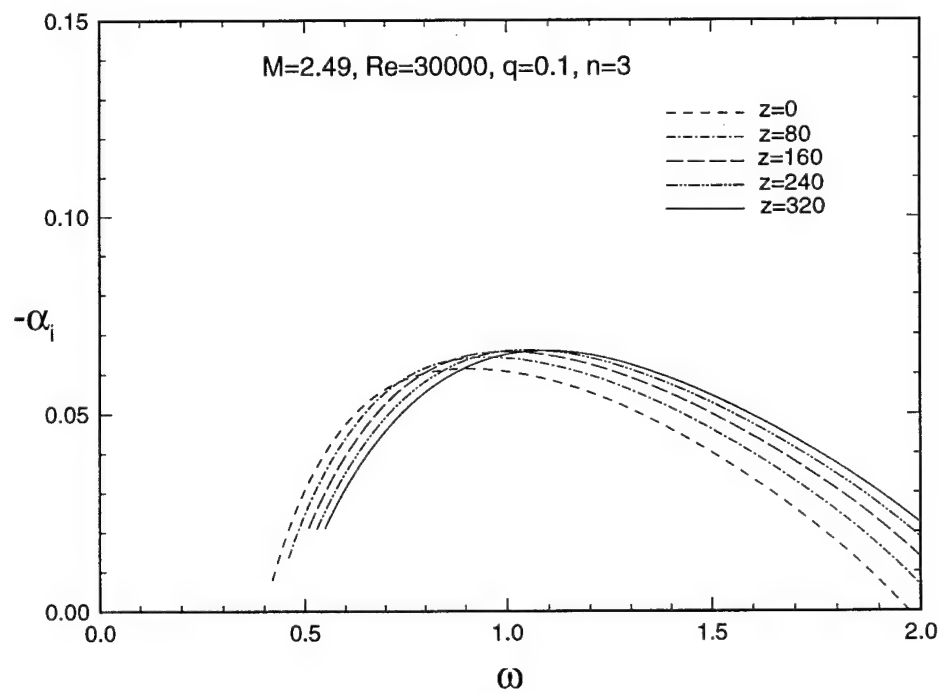
(a) Low swirl

Fig. 22.   Variation of the spatial growth rate of the third helical mode vs. frequency for different values of swirl parameter q.
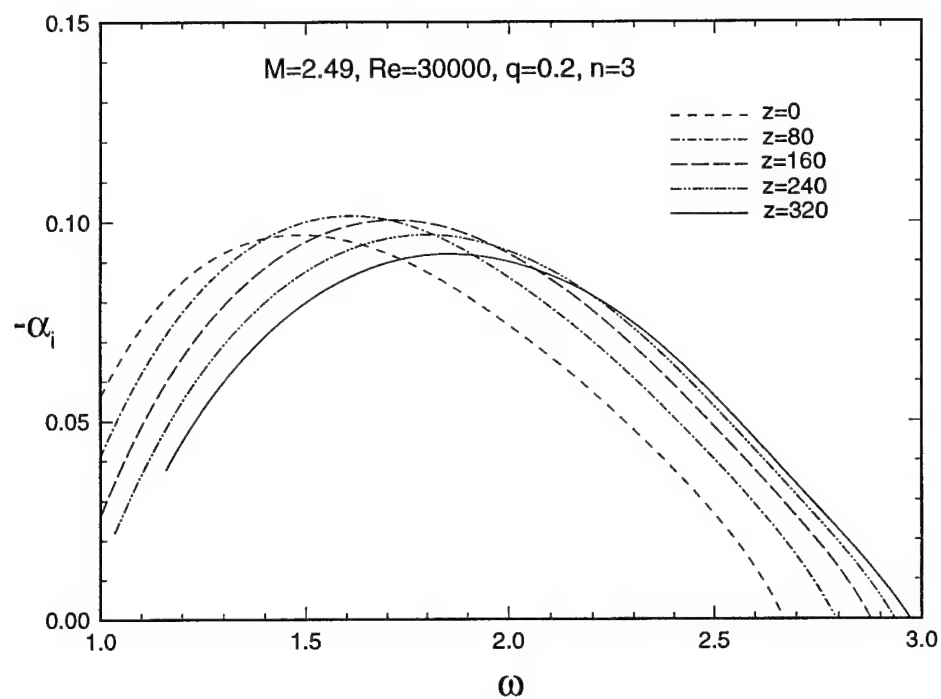
Fig. 22b.   Moderate swirl.
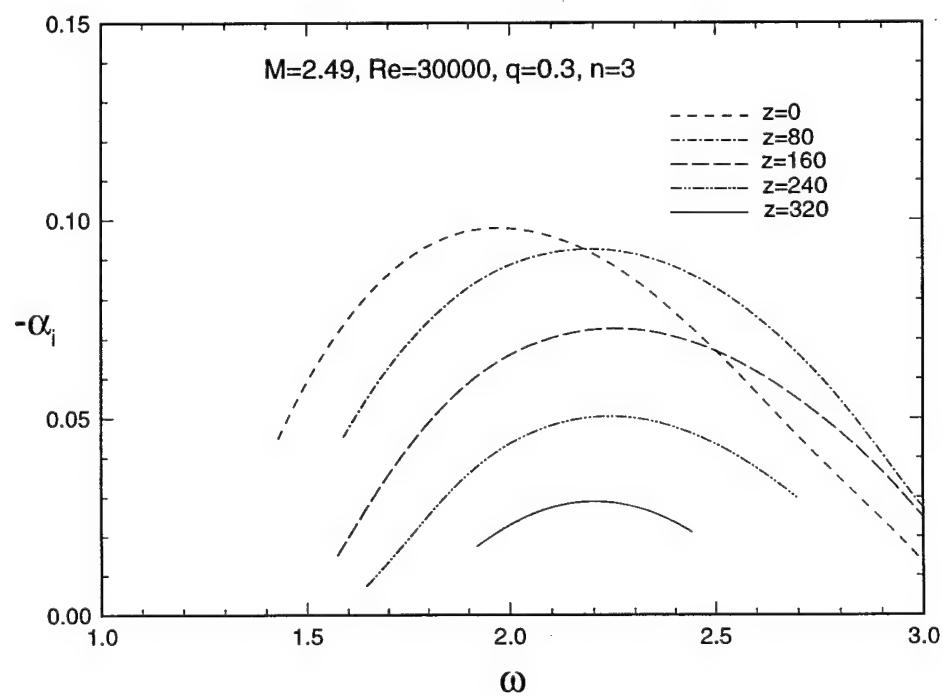
Fig. 22c.   High swirl.
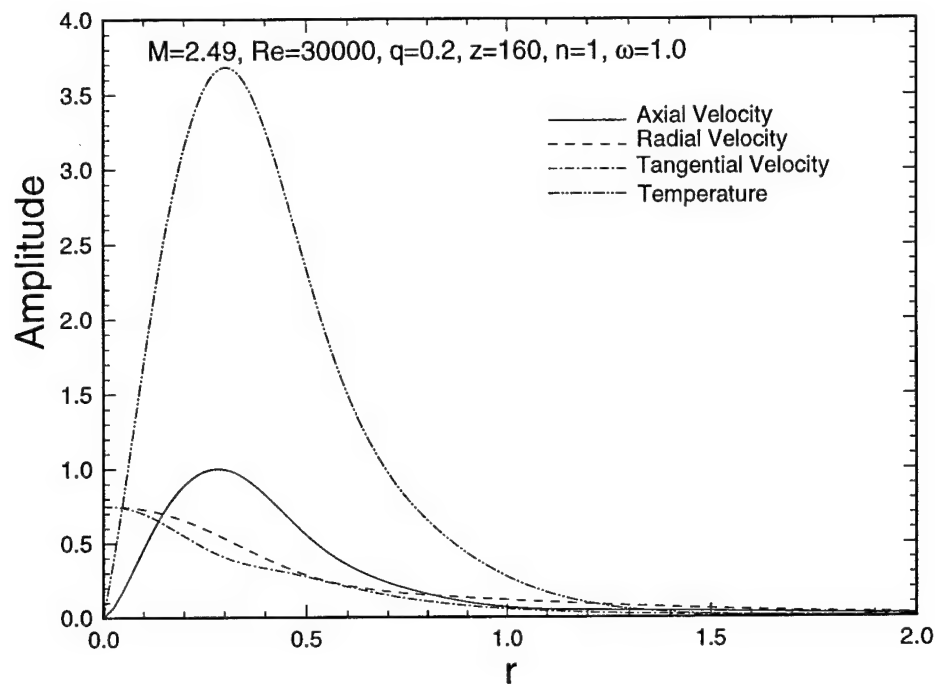
(a) first helical mode

Fig. 23. Radial distribution of the eigenfunctions for the first three helical unstable modes of the vortex.
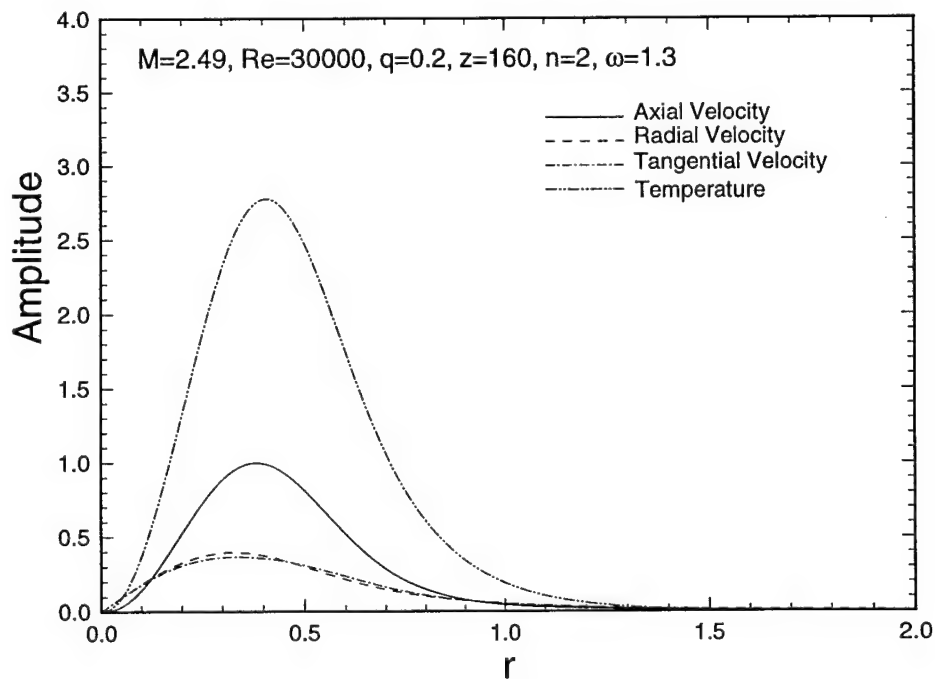
Fig. 23b. Second helical mode.
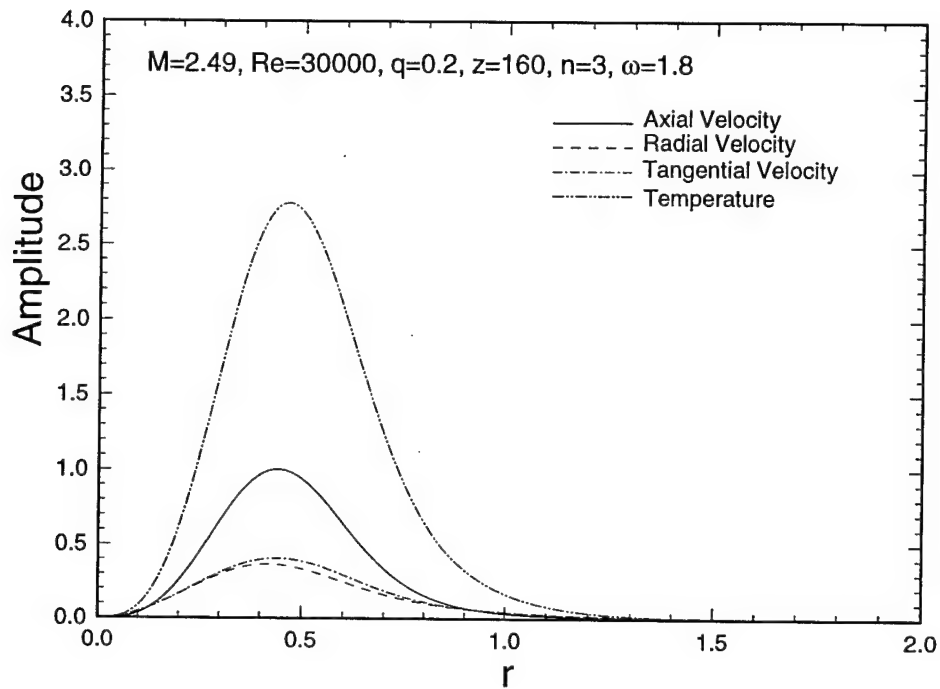
Fig. 23c.   Third helical mode.
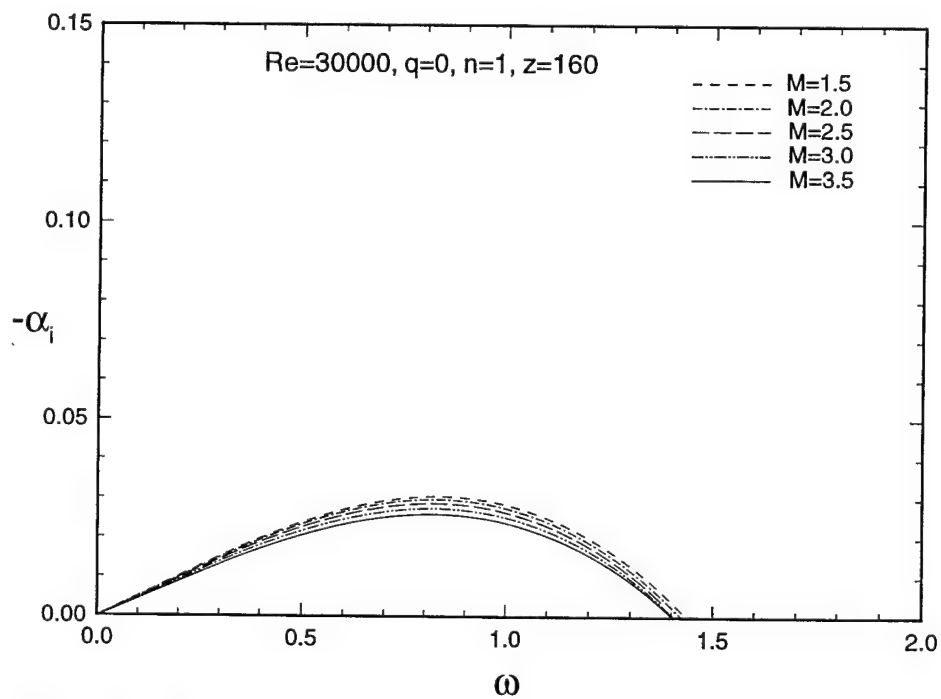
Fig. 24.   The effect of increasing the Mach number on the spatial growth rate of the wake's unstable mode.
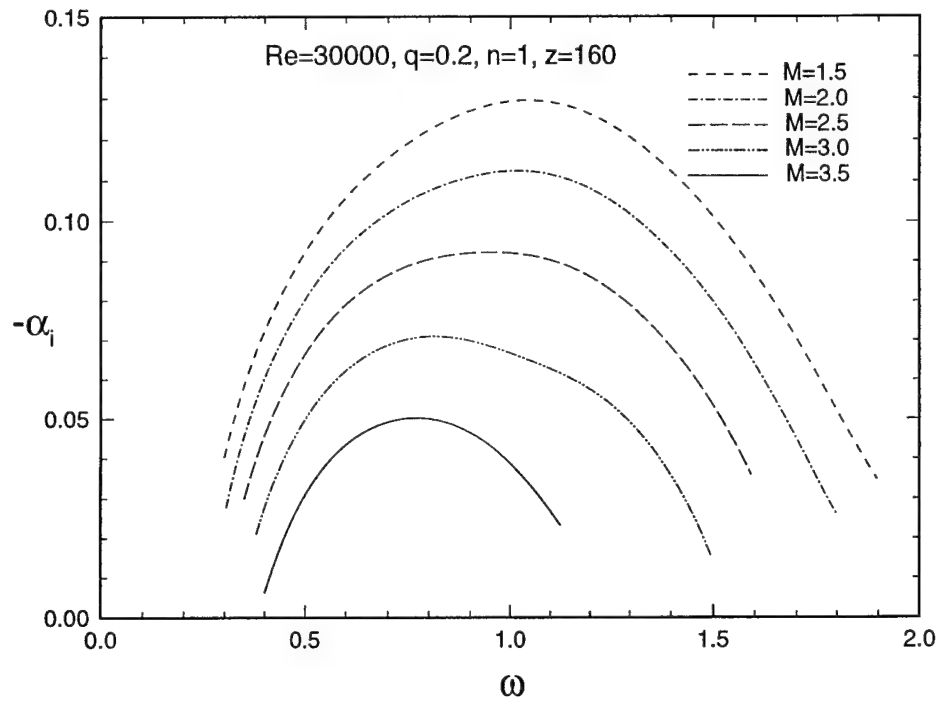
Fig. 25.   The effect of increasing the Mach number on the growth rate of the first helical instability mode.
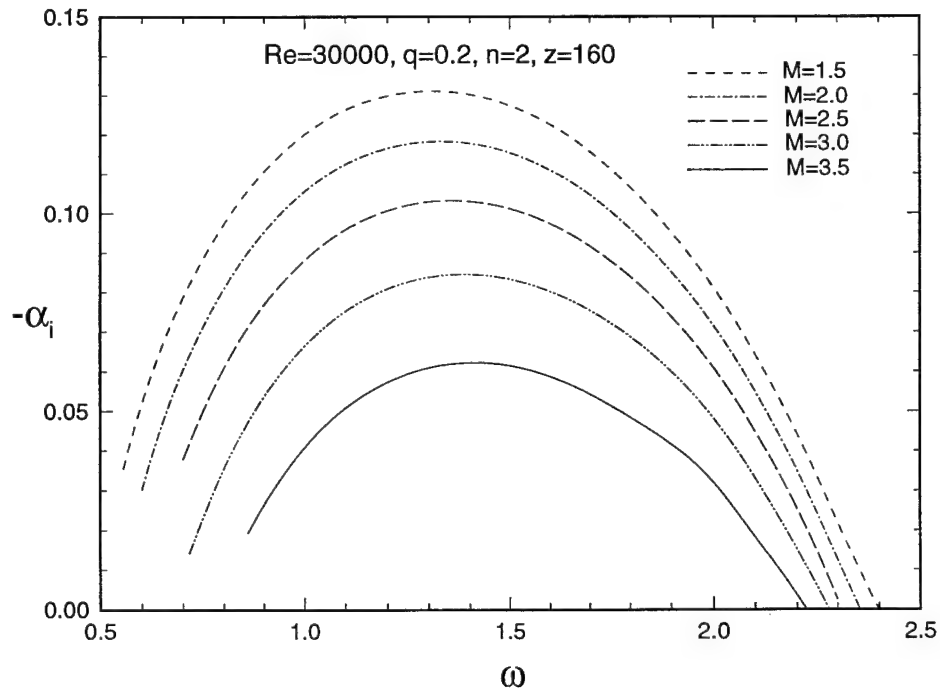
Fig. 26.   The effect of increasing the Mach number on the growth rate of the second helical instability mode.
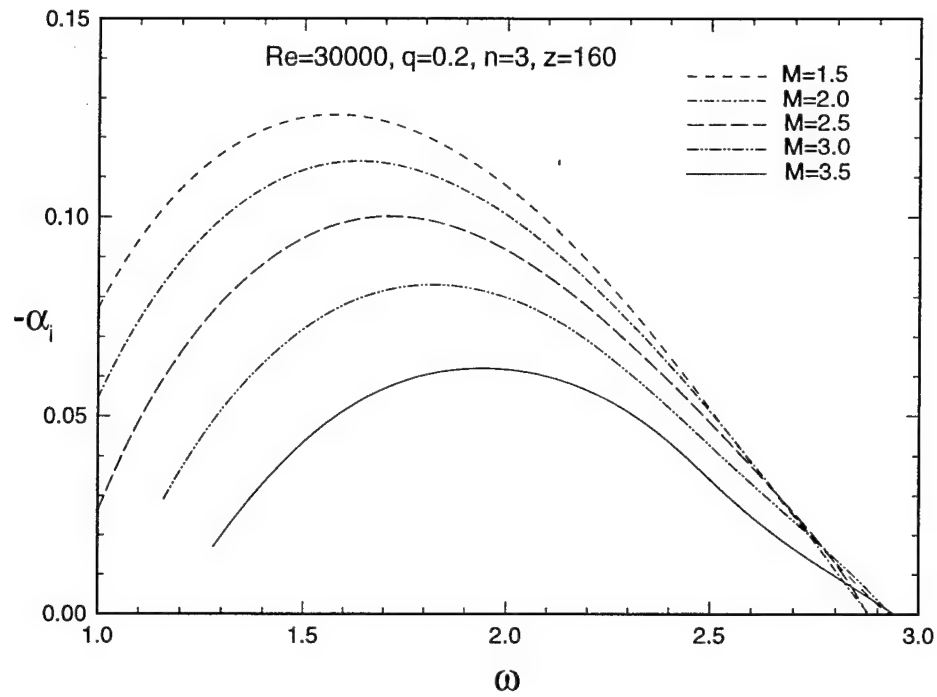
Fig. 27. The effect of increasing the Mach number on the growth rate of the third helical instability mode.
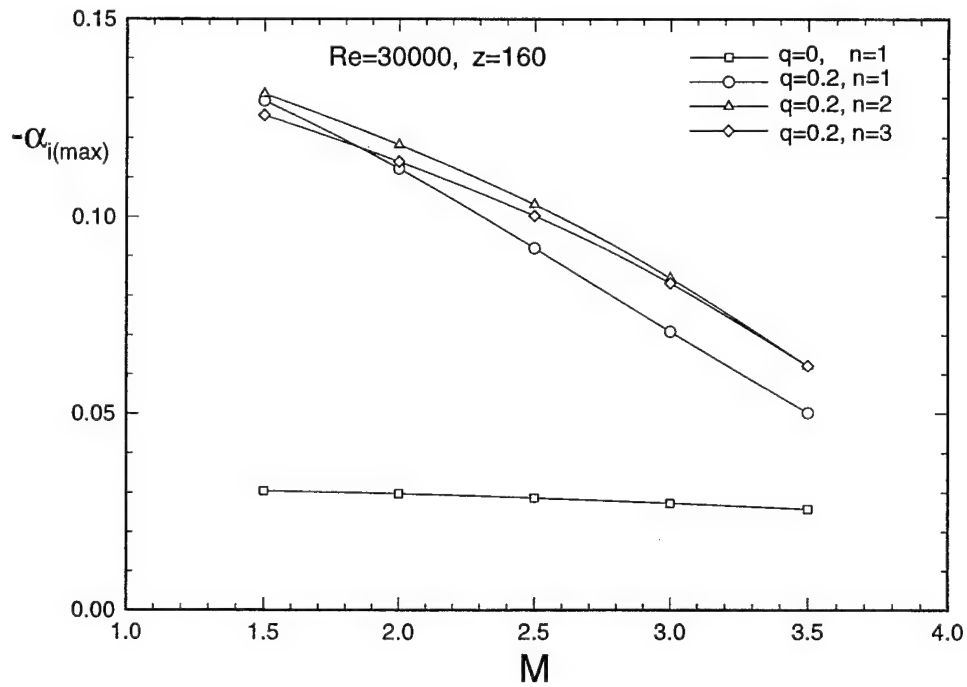
Fig. 28. Peak spatial growth rate at different freestream Mach number.
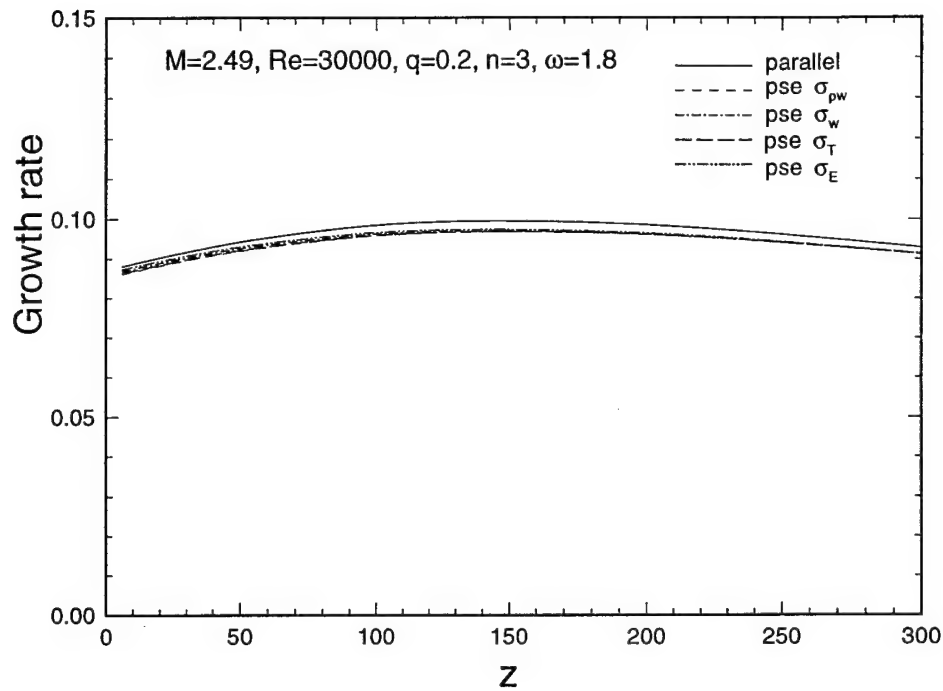
Fig. 31.   The effect of streamwise meanflow variation on the growth rate of the third helical mode.
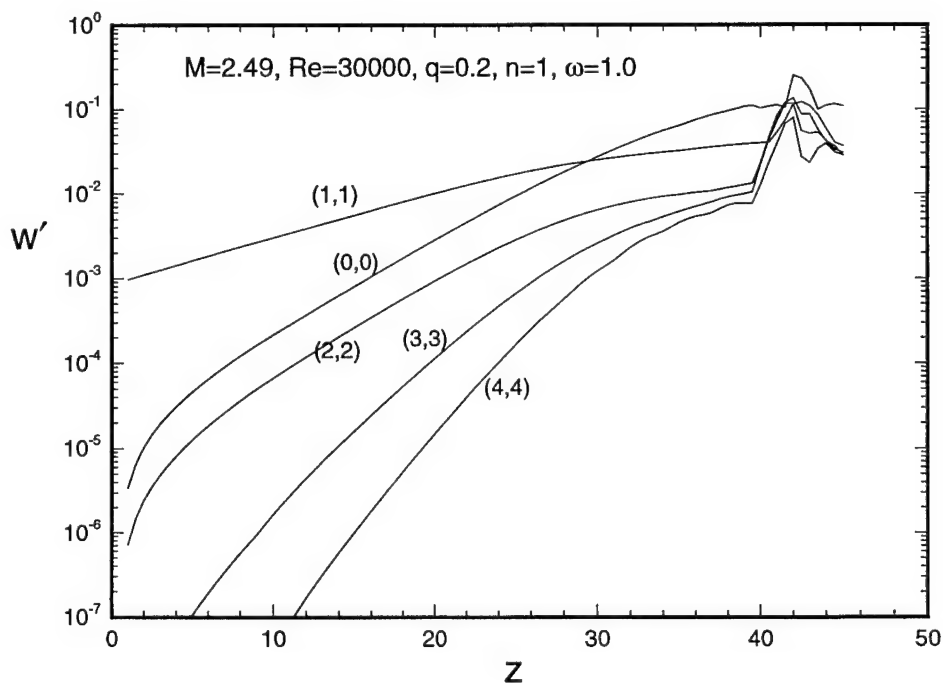
Fig. 32.   Evolution of axial velocity fluctuations with axial distance showing the dominant helical (1,1) mode along with other Fourier harmonic waves.
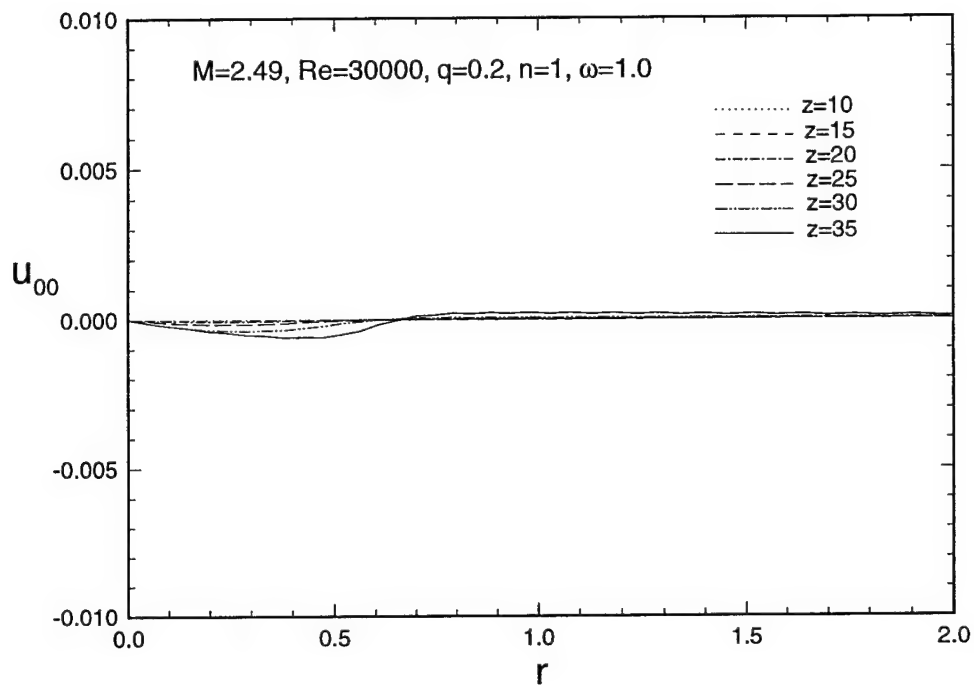
(a) Radial velocity

Fig. 33. Distribution of various components of meanflow distortion (0,0) mode in the radial direction.
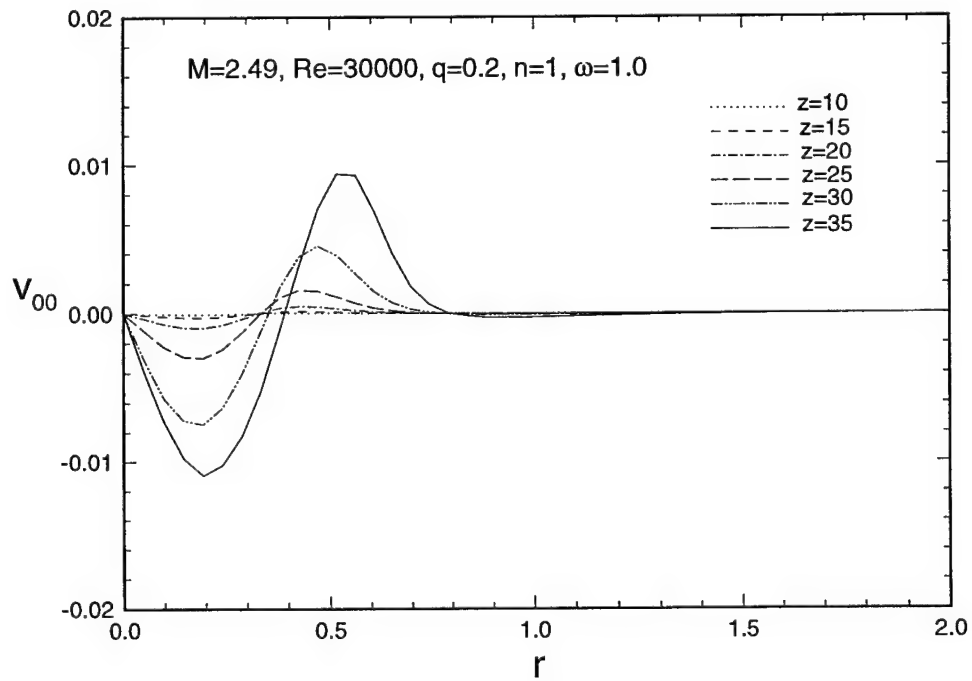
Fig. 33b. Tangential velocity.

59
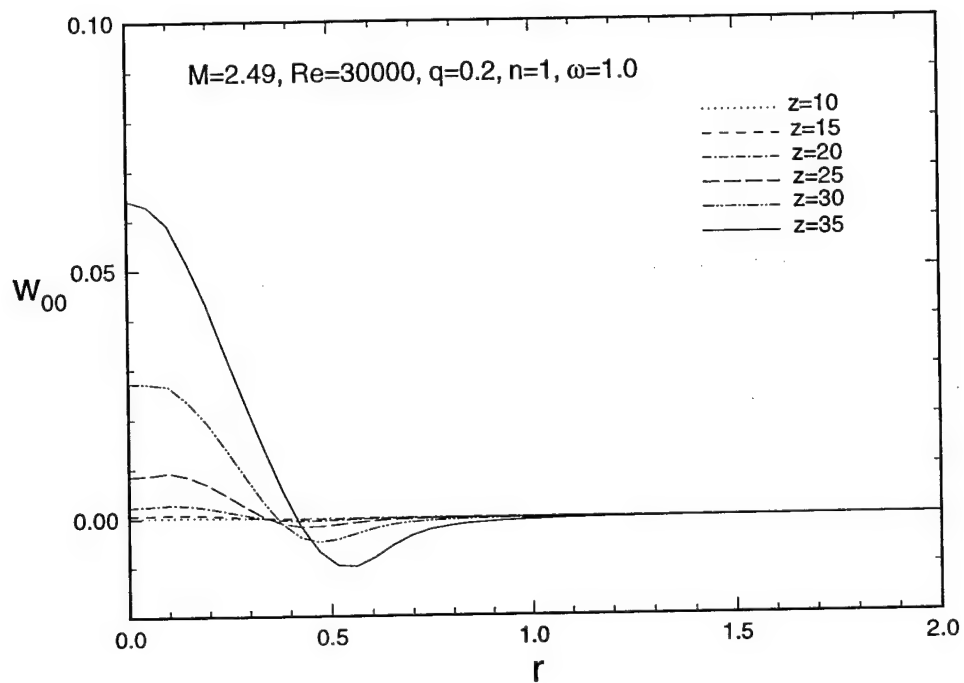
Fig. 33c.   Axial velocity.
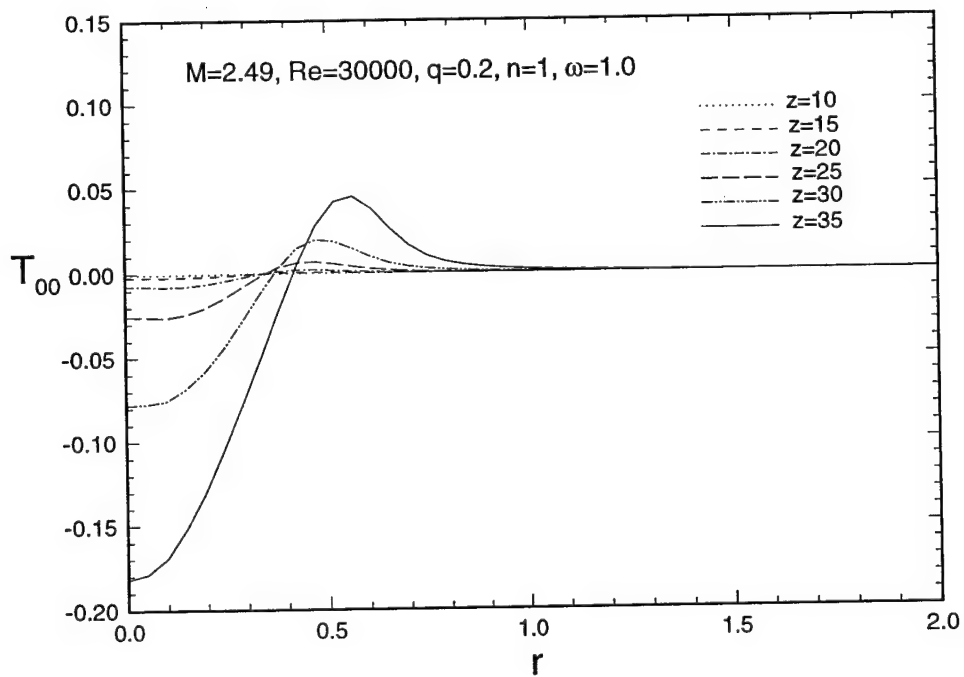
Fig. 33d.   Temperature.
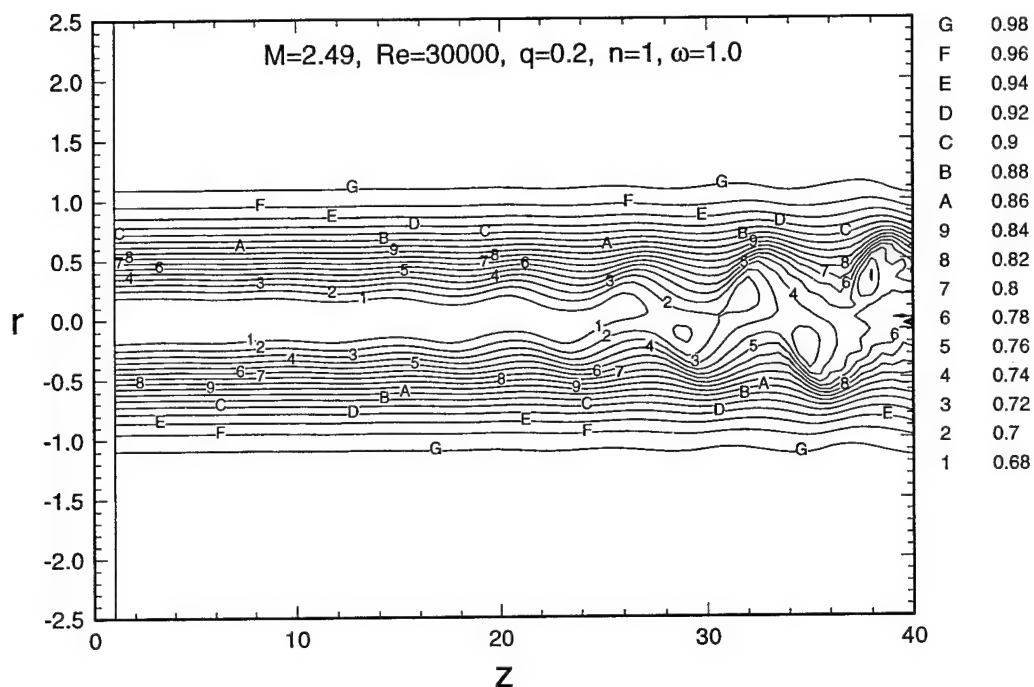
Fig. 34.   Axial velocity contour plots in the r-z plane showing the emergence of large scale coherent structures in the nonlinear stage.
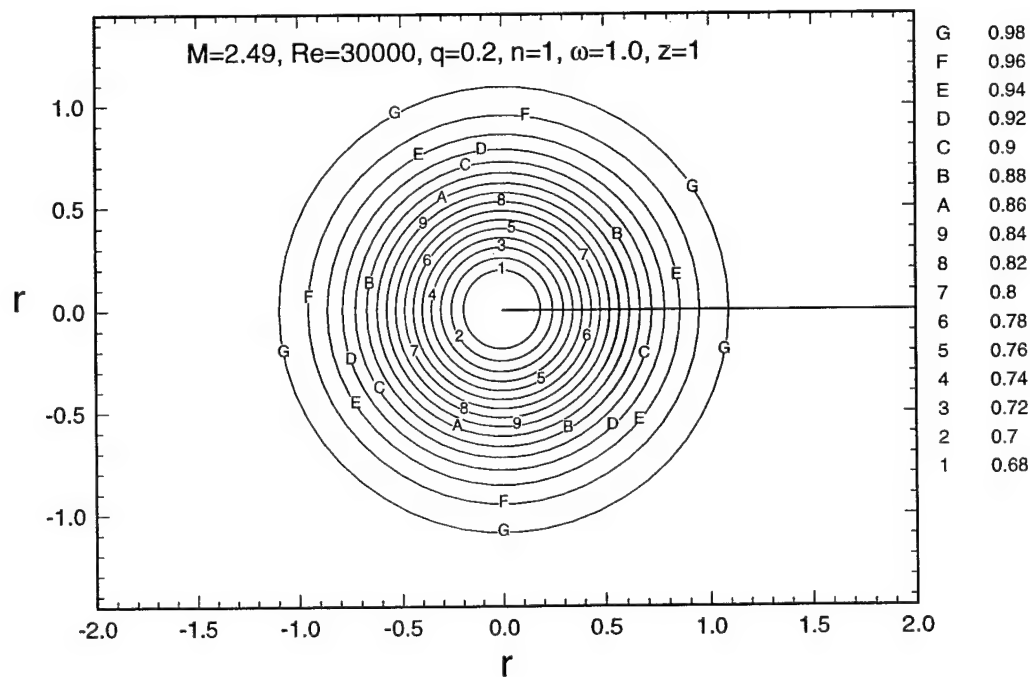
(a) $z = 1$

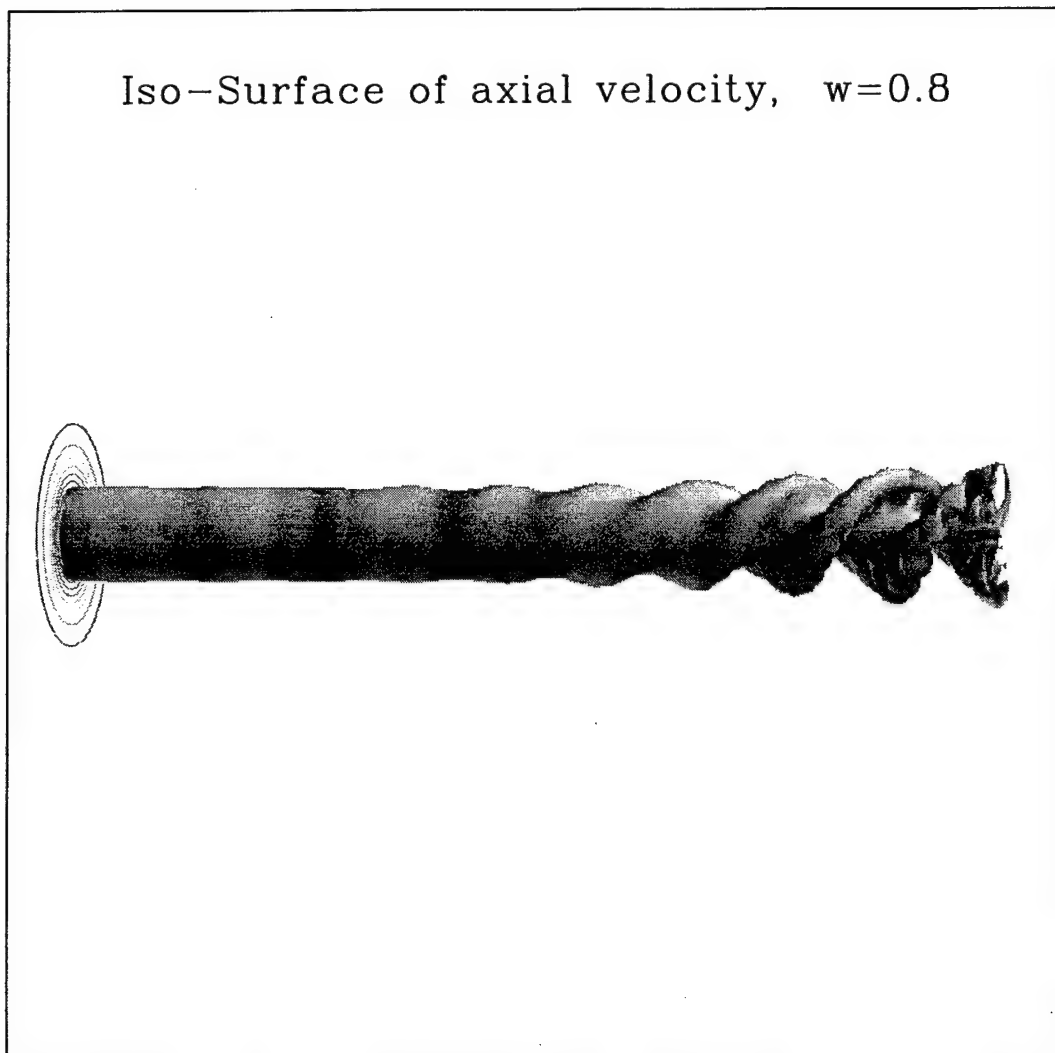Fig. 35.   Axial velocity contour plots in the $r - \theta$ plane at different streamwise locations.
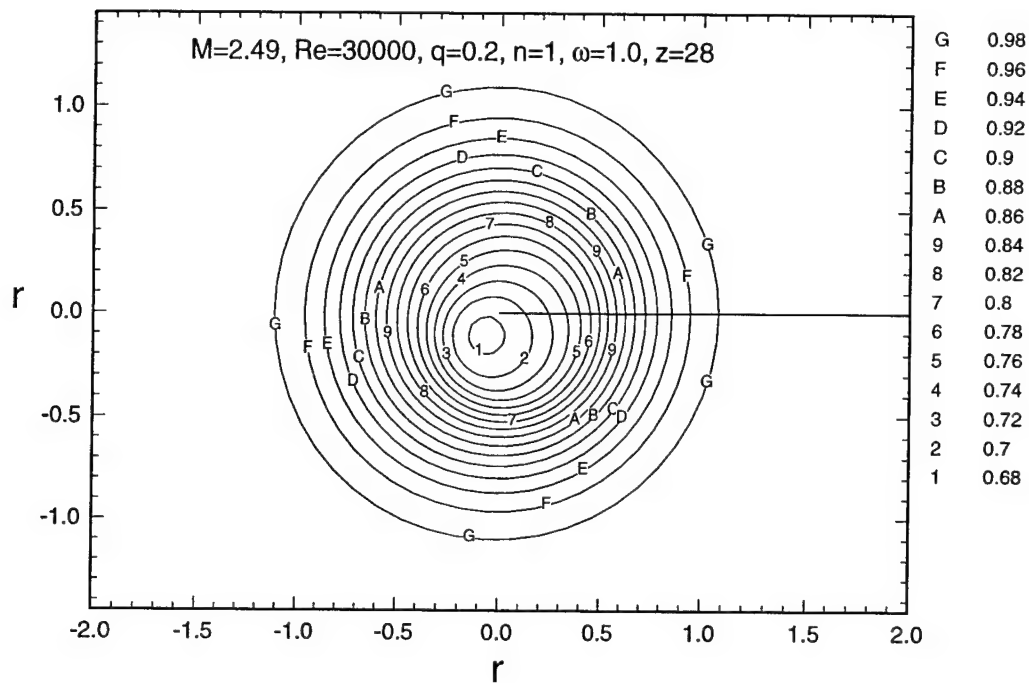
Fig. 35b. $z = 28$
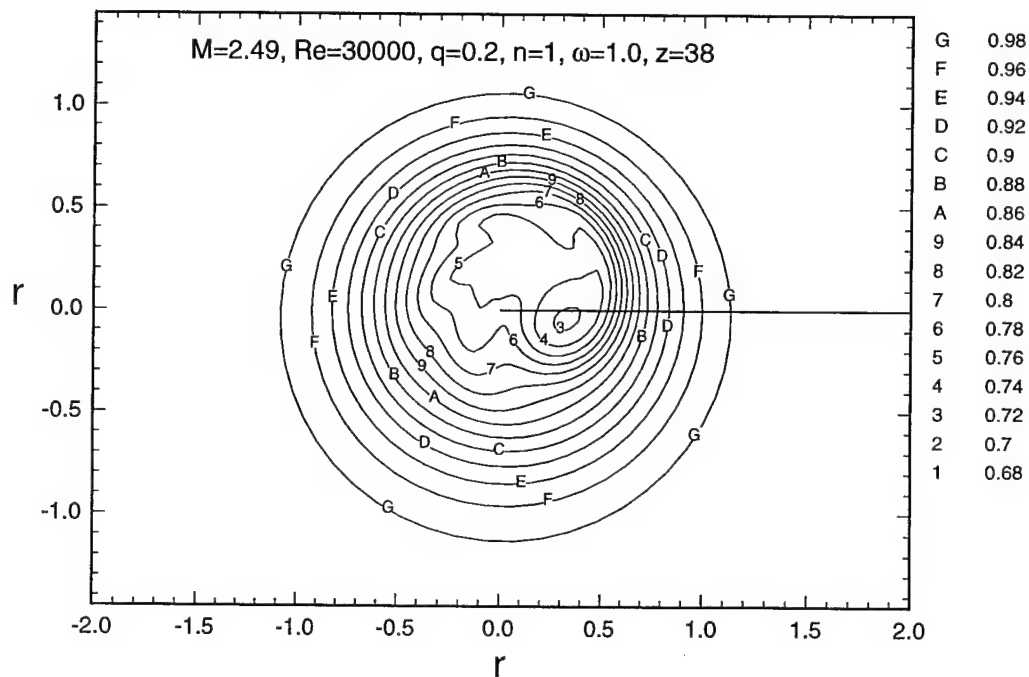
Fig. 35c. $z = 38$
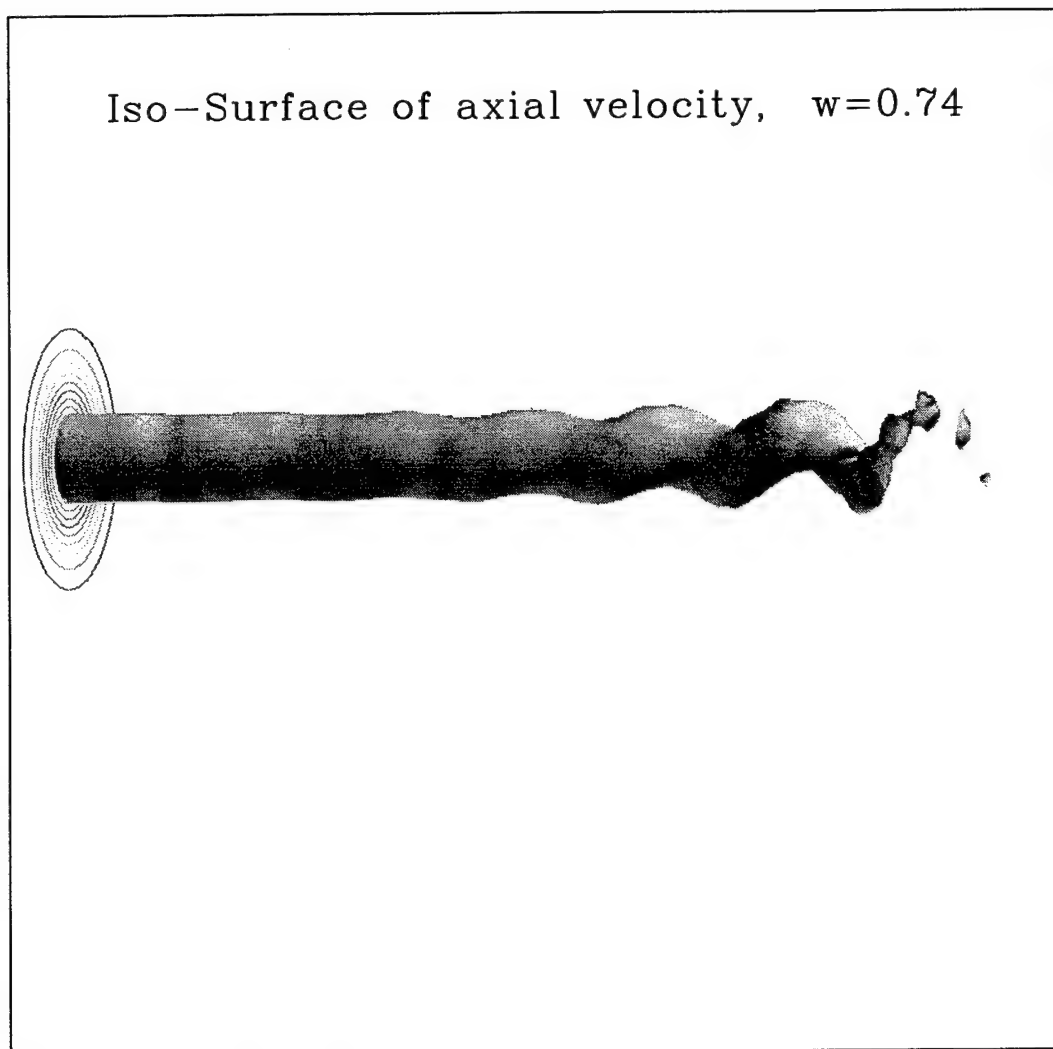
Fig. 36.   Iso-surface of axial velocity showing streamwise evolution of vortex core in the presence
of the instability mode and the disappearance of the wake velocity deficit.

Velocity Vectors in Cross Plane at z=1
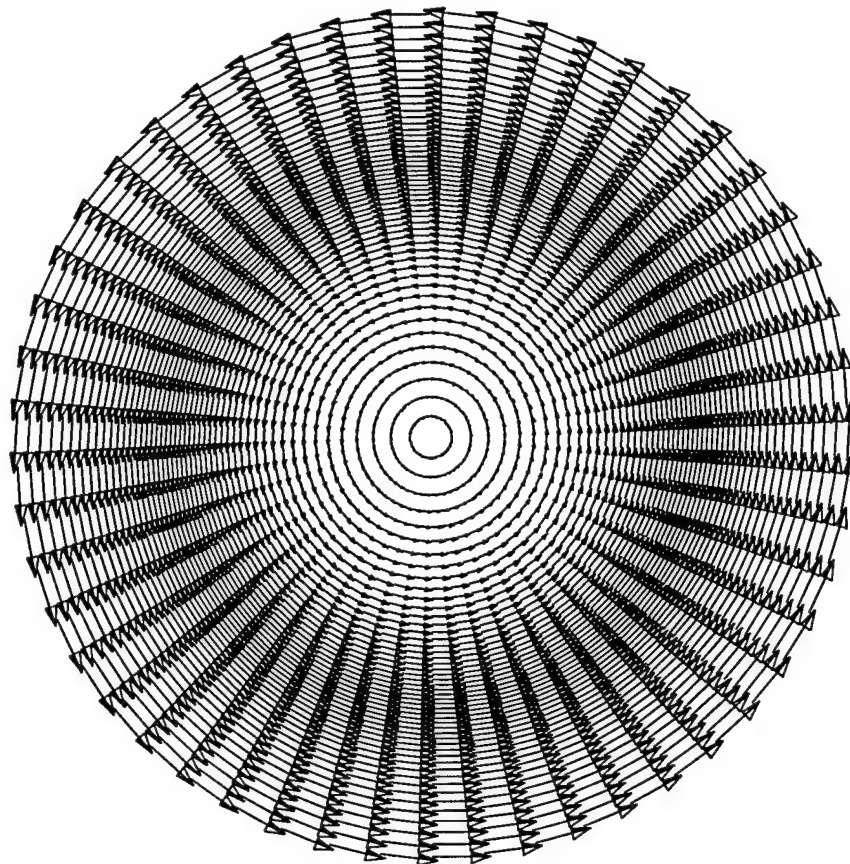
(a) Initial field.

Fig. 37.   Cross plane velocity vectors showing the initial axisymmetric flowfield and the end of nonlinear saturation stage.

Velocity Vectors in Cross Plane at z=39
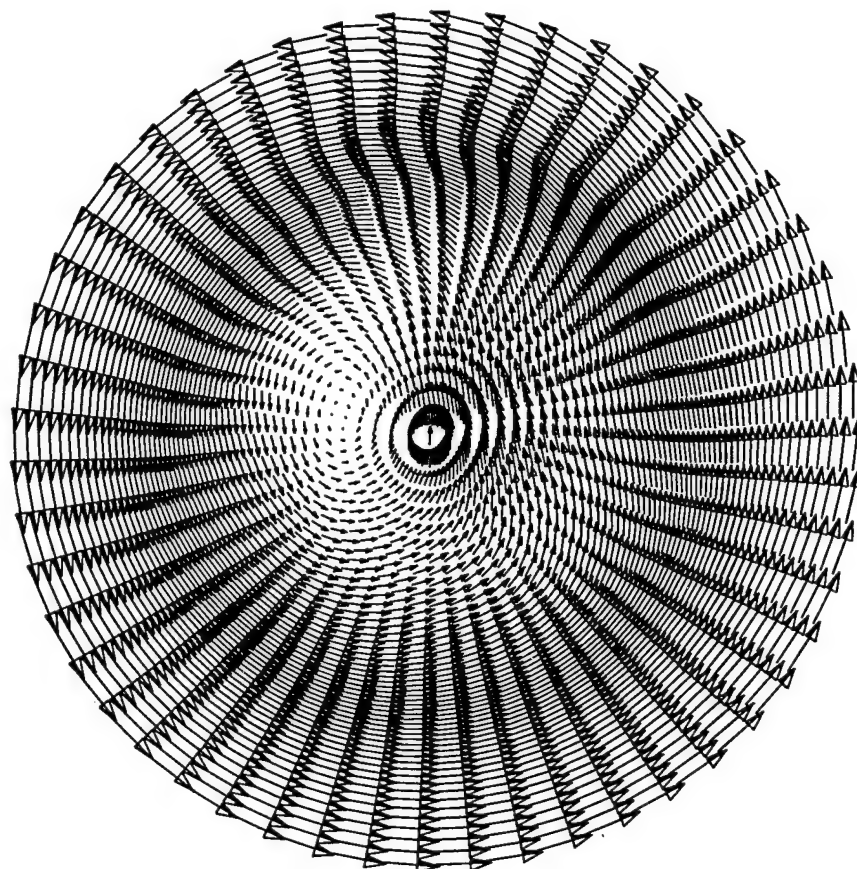
Fig. 37b.   Nonlinear saturation stage.
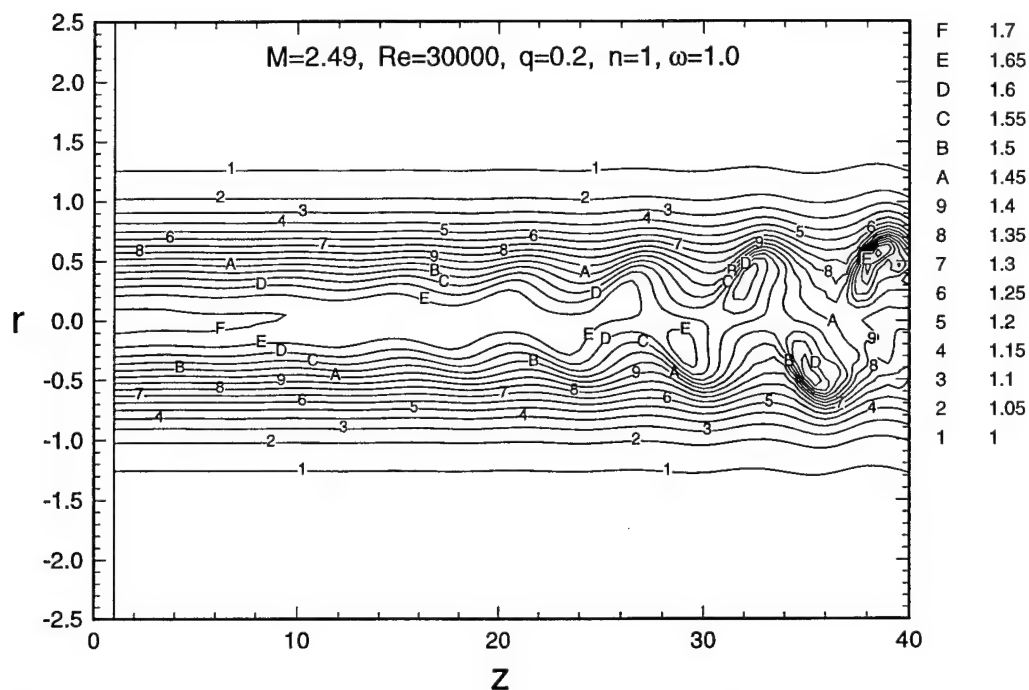
Fig. 38. Temperature contour plots in the r-z plane showing the appearance of large scale coherent structures in the nonlinear stage.
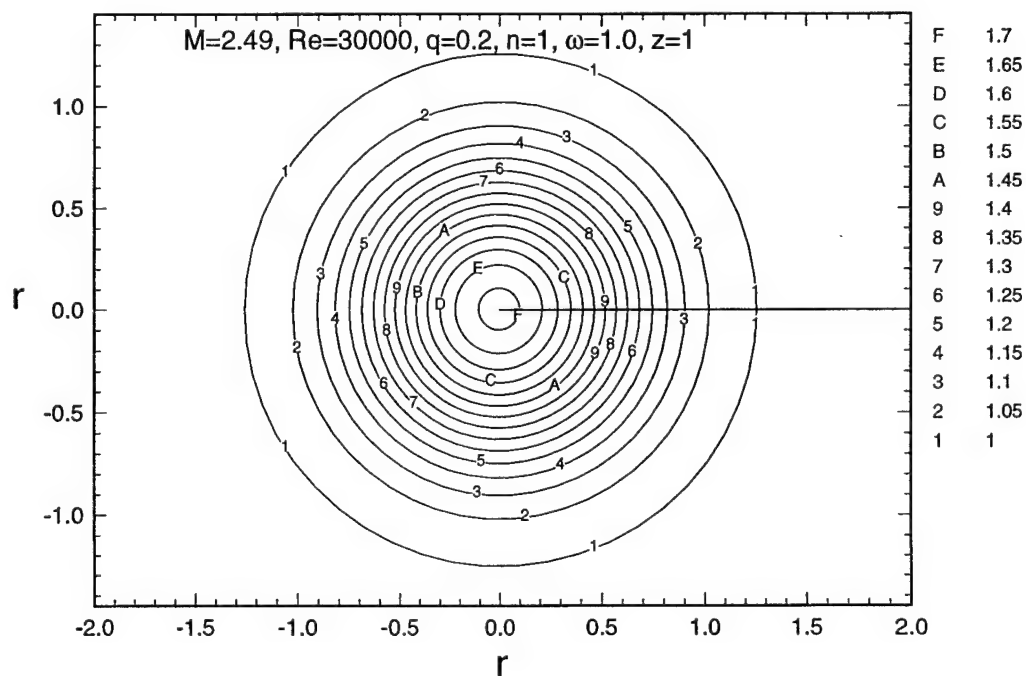
(a) $z = 1$

Fig. 39. Temperature contour plots in the $r - \theta$ plane showing the loss of axisymmetry as the instability evolves downstream.
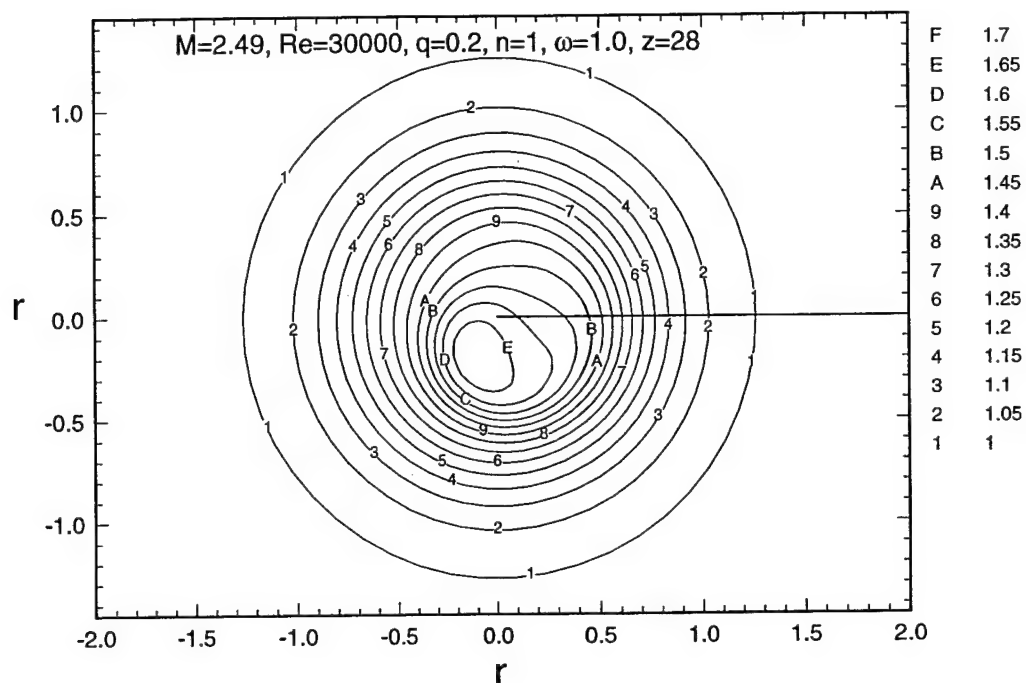
Fig. 39b. $z = 28$
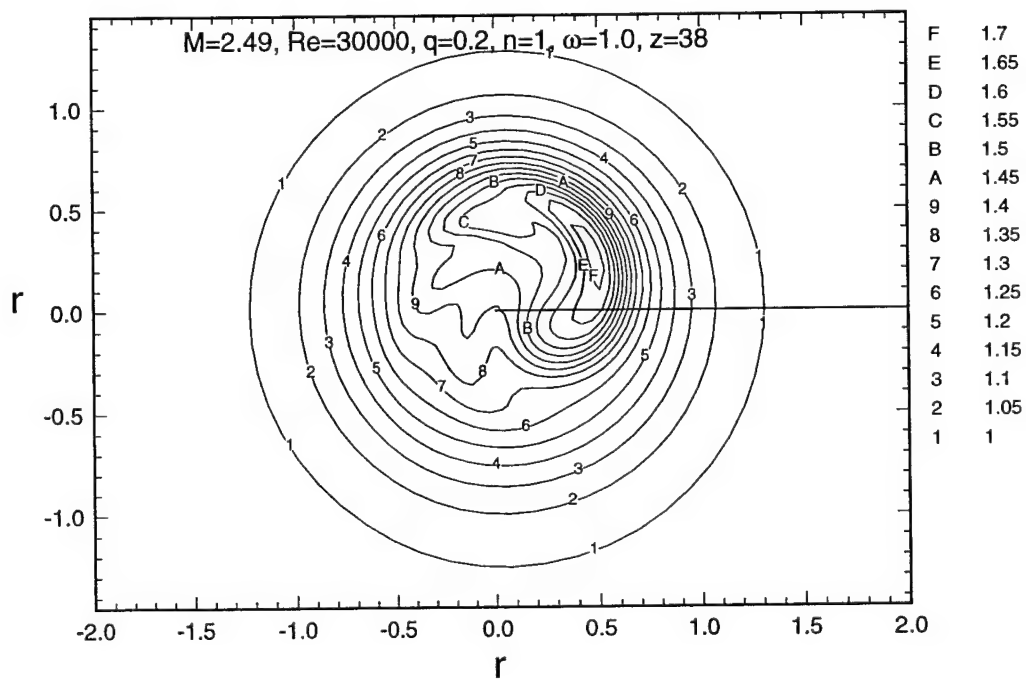
Fig. 39c. $z = 38$
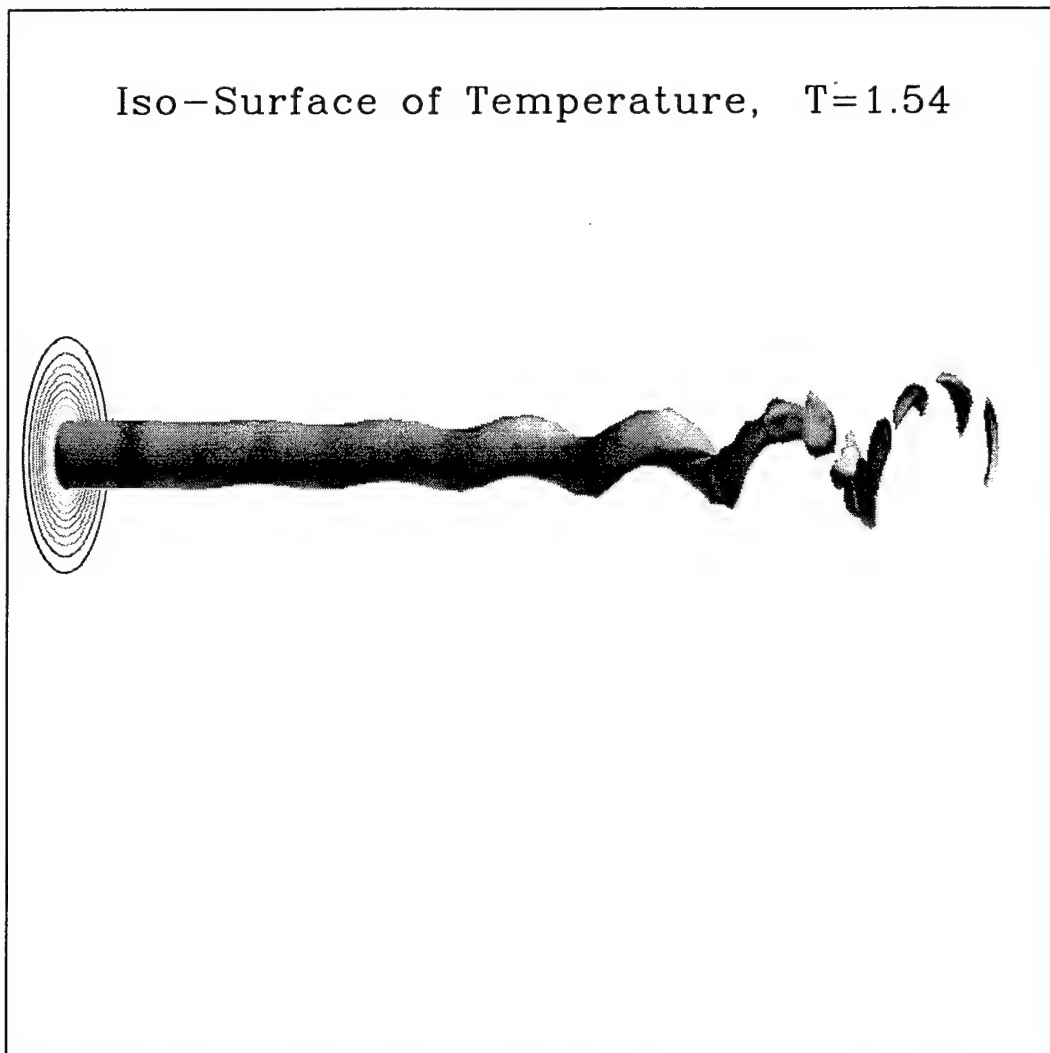
Fig. 40.   Iso-surface of temperature showing evolution of the vortex core in the streamwise direction and its subsequent breakdown into smaller segments of hotter fluid.

Iso−Surface of axial vorticity,   OMEGA_z=0.078
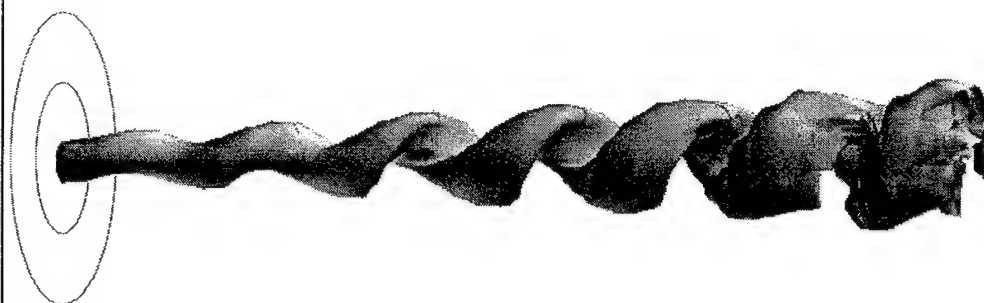
Fig. 41.   Iso-surface of axial vorticity showing the evolution of vorticity field in the vortex core.
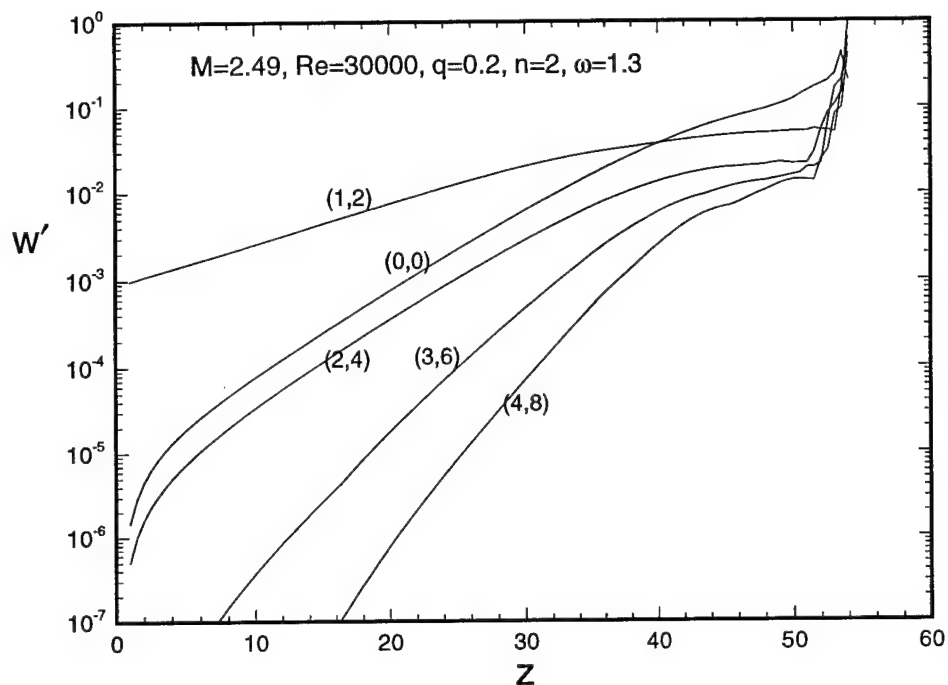
Fig. 42.   Evolution of axial velocity fluctuations with axial distance showing the dominant helical (1,2) mode along with other Fourier harmonic waves.
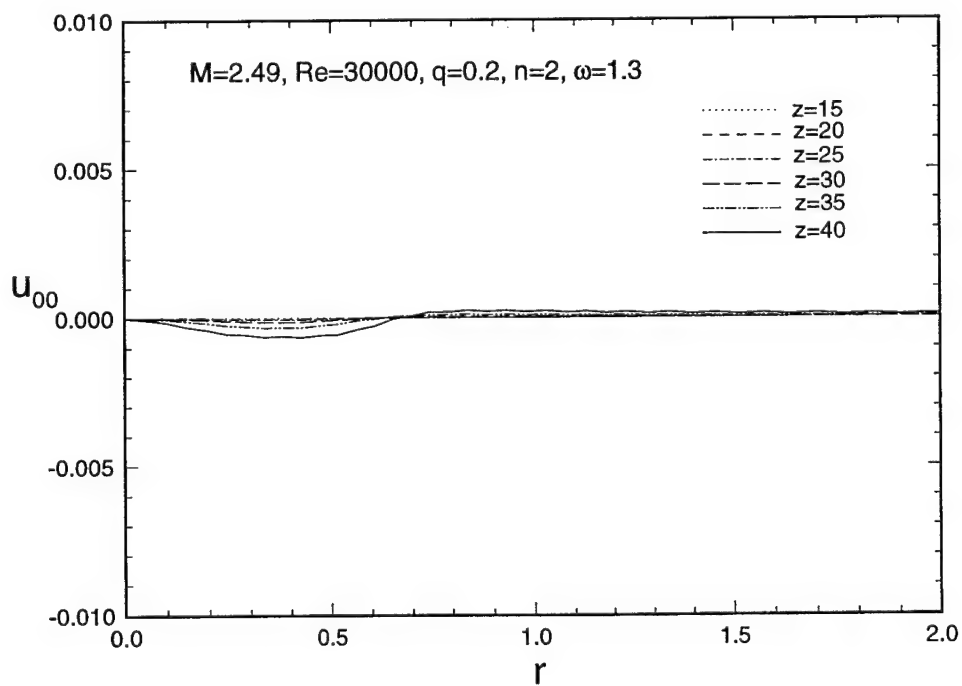
(a) Radial velocity

Fig. 43.   Distribution of various components of meanflow distortion (0,0) mode in the radial direction.
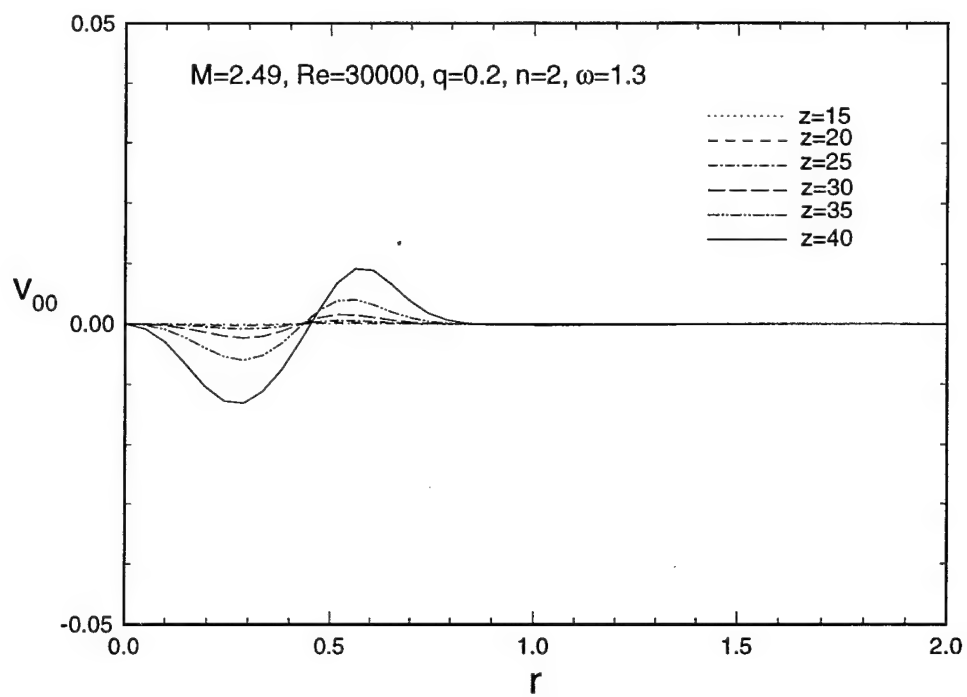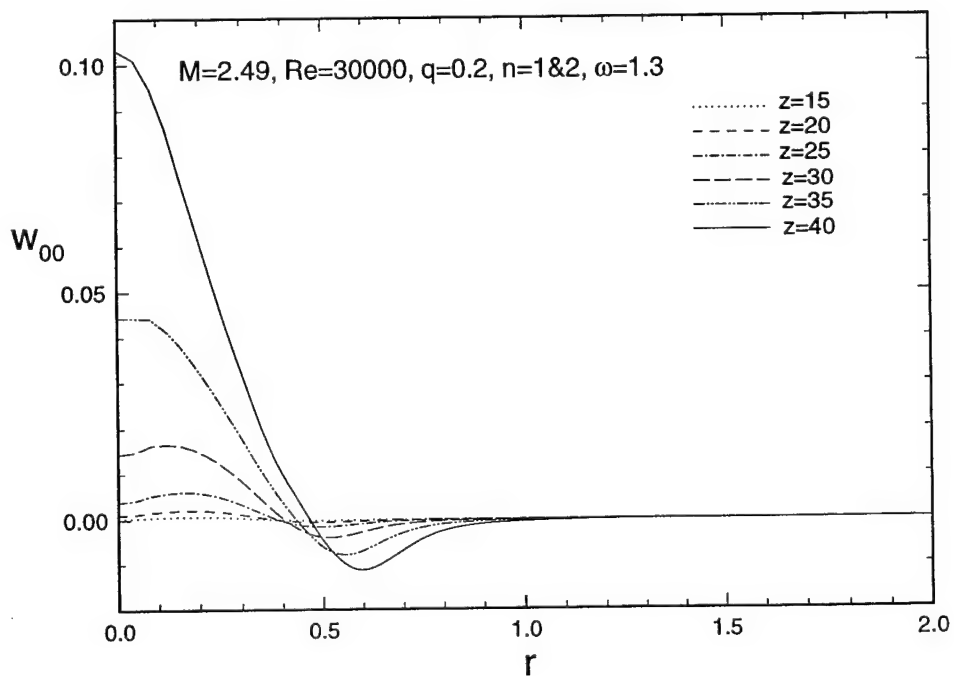
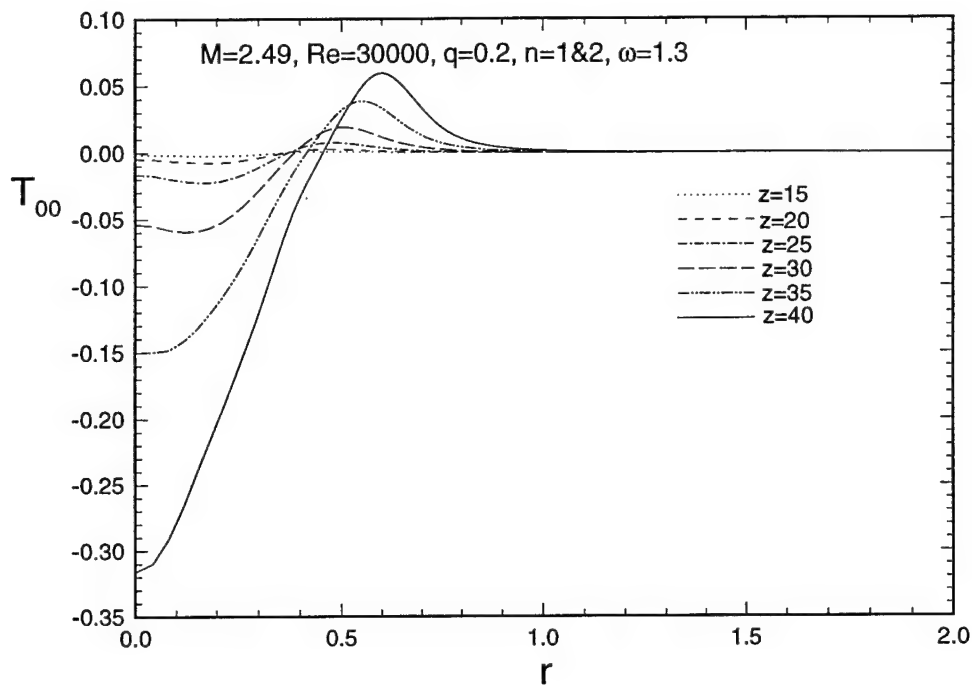Fig. 43b.   Tangential velocity.
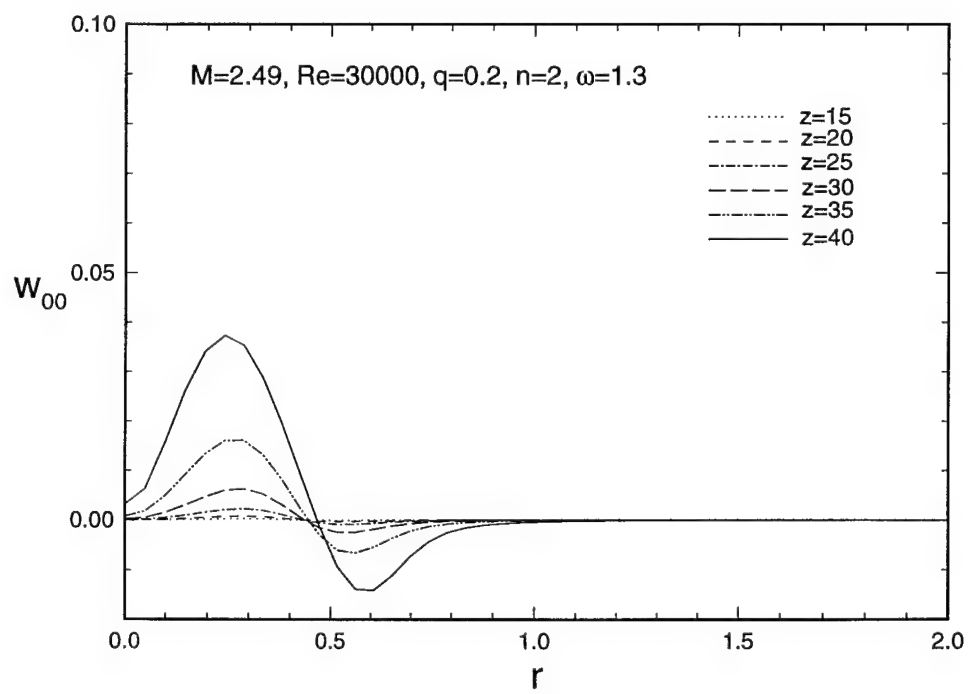
Fig. 43c.   Axial velocity.
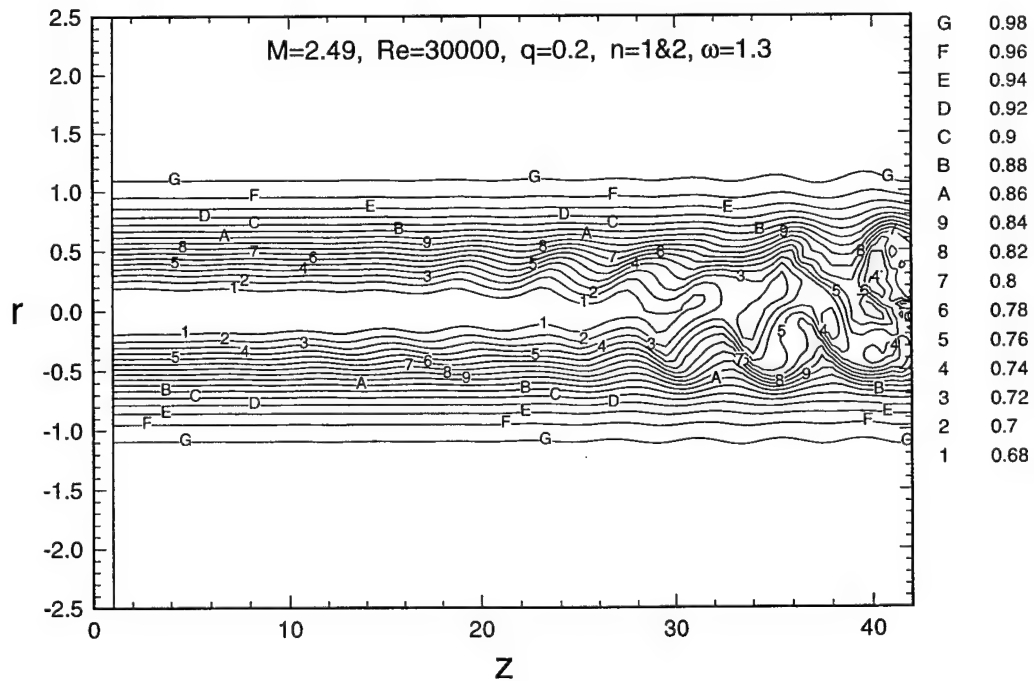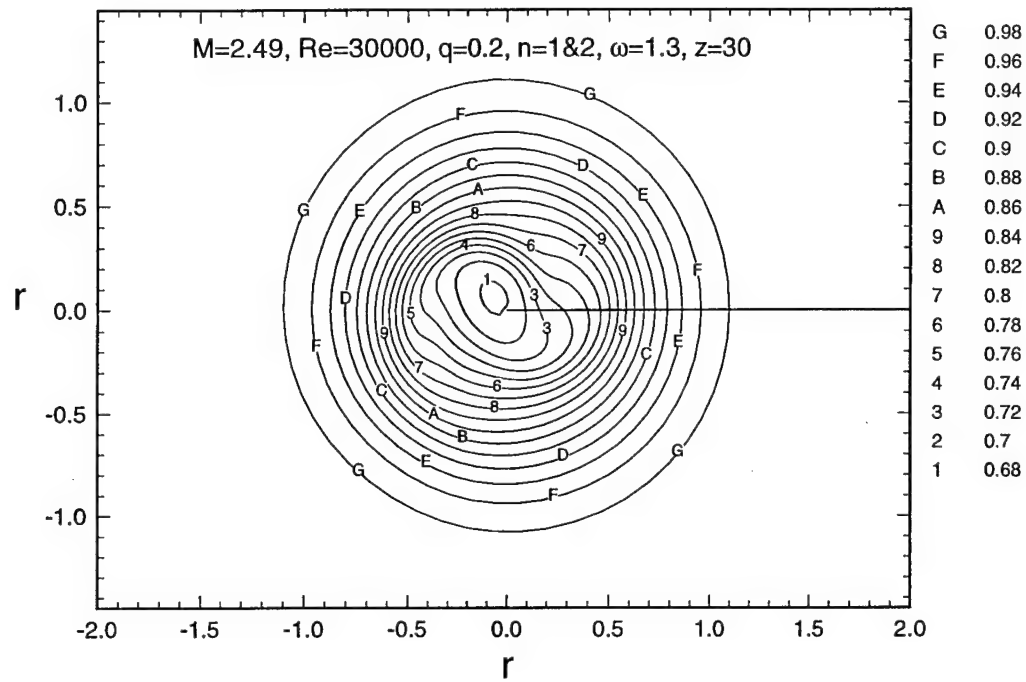
71
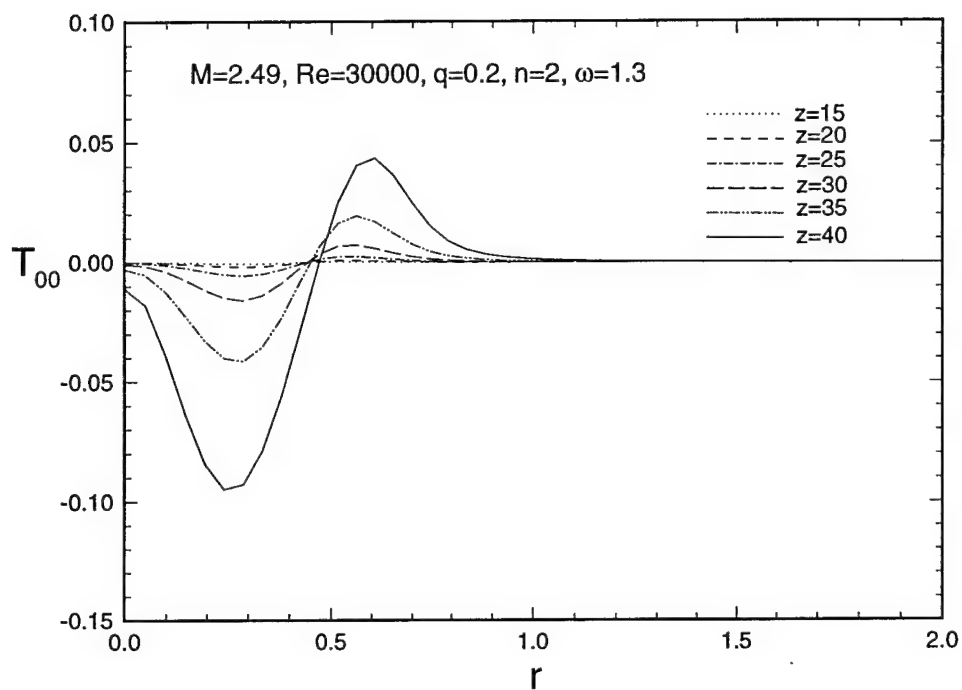
Fig. 43d.   Temperature.
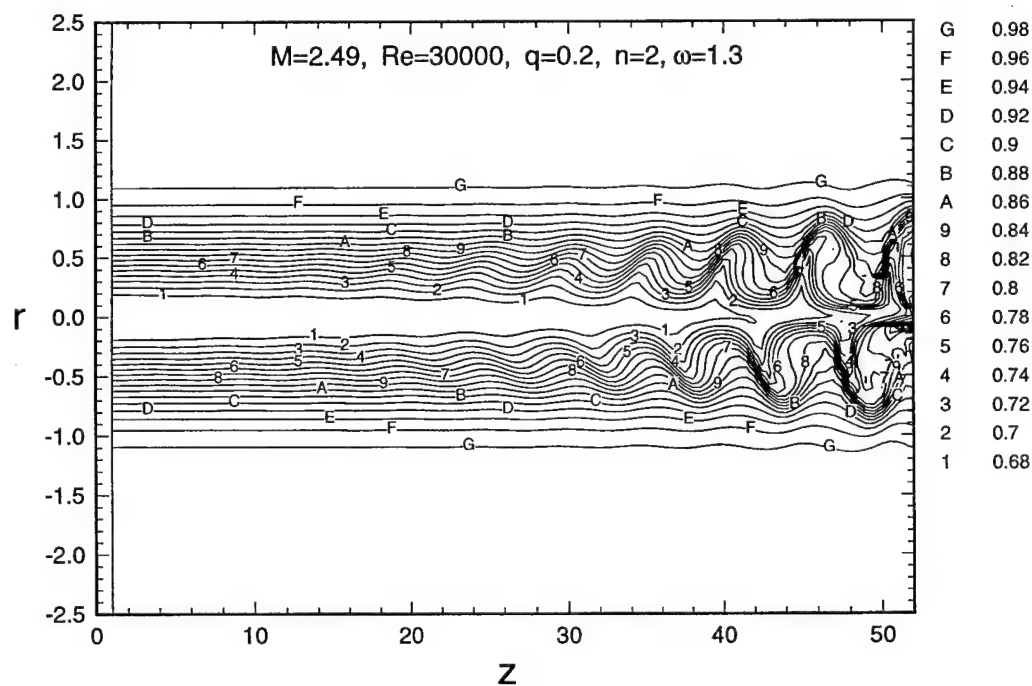
Fig. 44.   Axial velocity contour plots in the r-z plane showing the emergence of large scale coherent structures in the nonlinear stage.
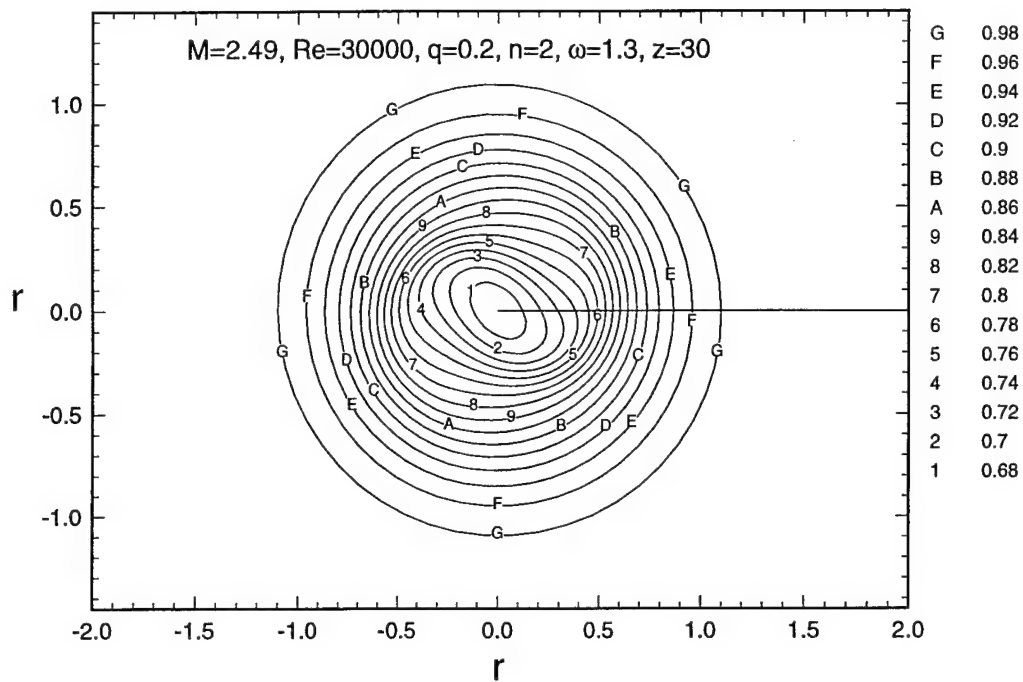
(a) $z = 30$

Fig. 45. Axial velocity contour plots in the $r - \theta$ plane at different streamwise locations.
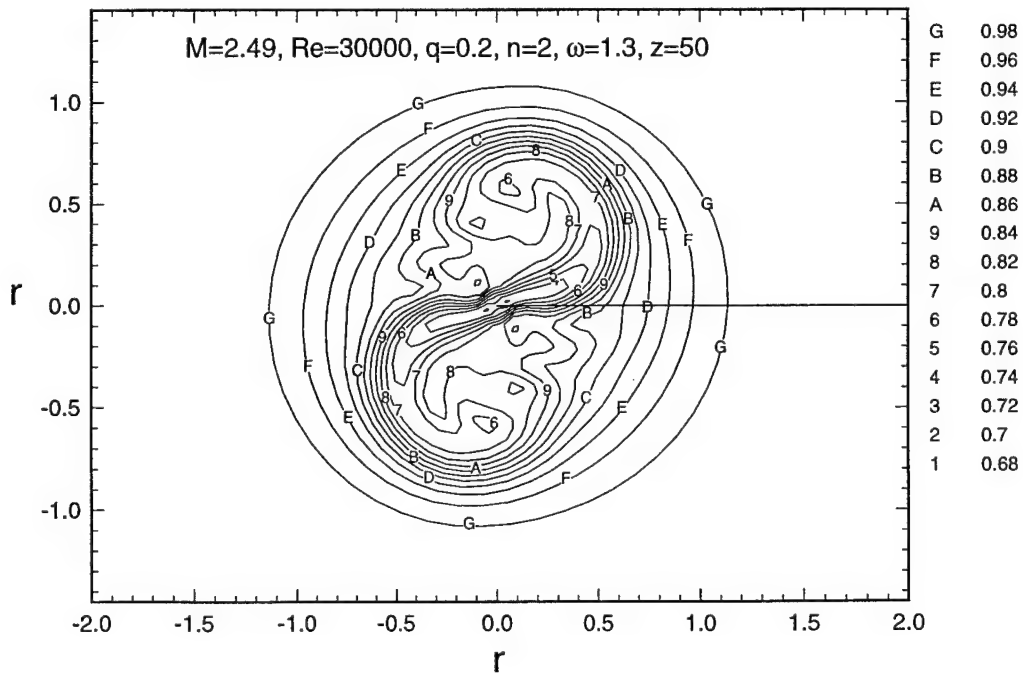
Fig. 45b. $z = 50$

Fig. 46.   Iso-surface of axial velocity showing streamwise evolution of vortex core in the presence of the instability mode.
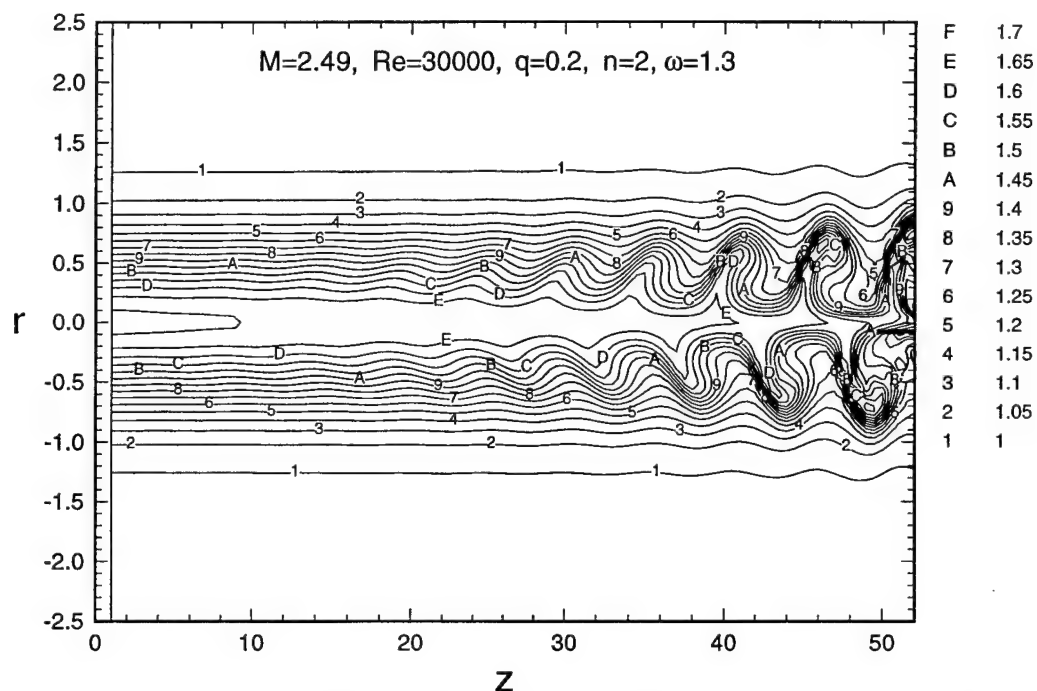
Fig. 47. Temperature contour plots in the *r-z* plane showing the appearance of large scale coherent structures in the nonlinear stage.
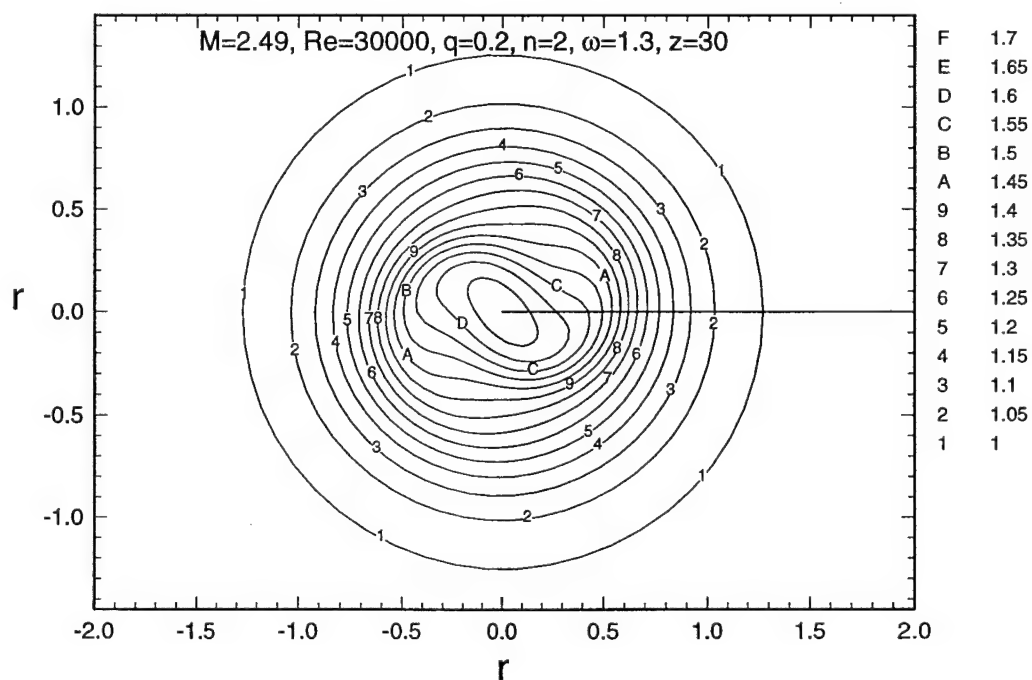
(a) *z* = 30

Fig. 48. Temperature contour plots in the *r − θ* plane showing the loss of axisymmetry as the instability evolves downstream.
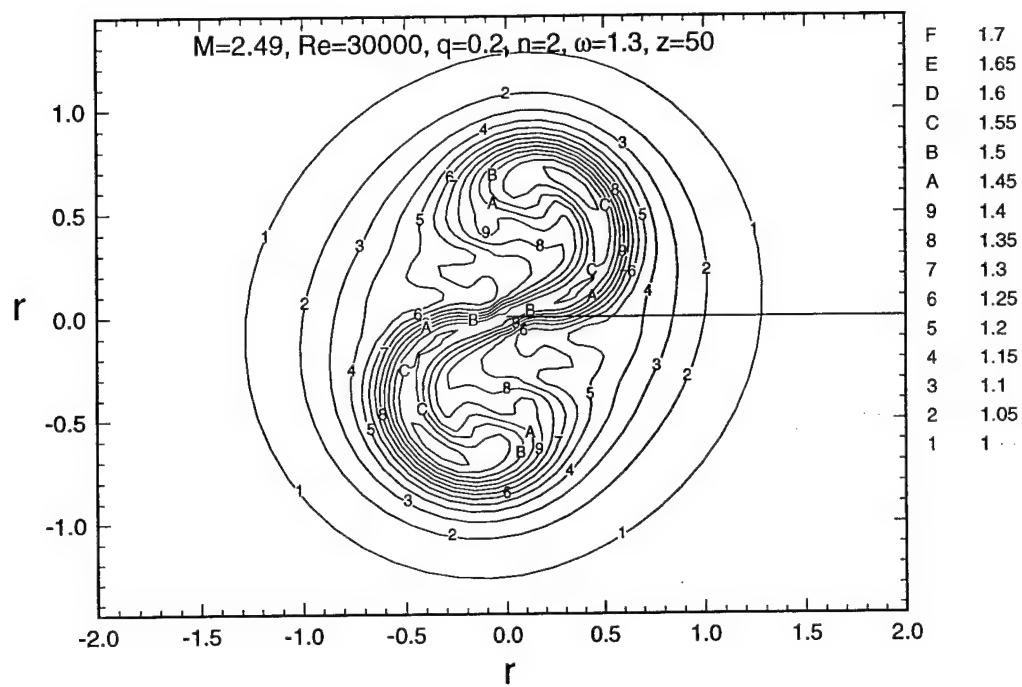
Fig. 48b. $z = 50$
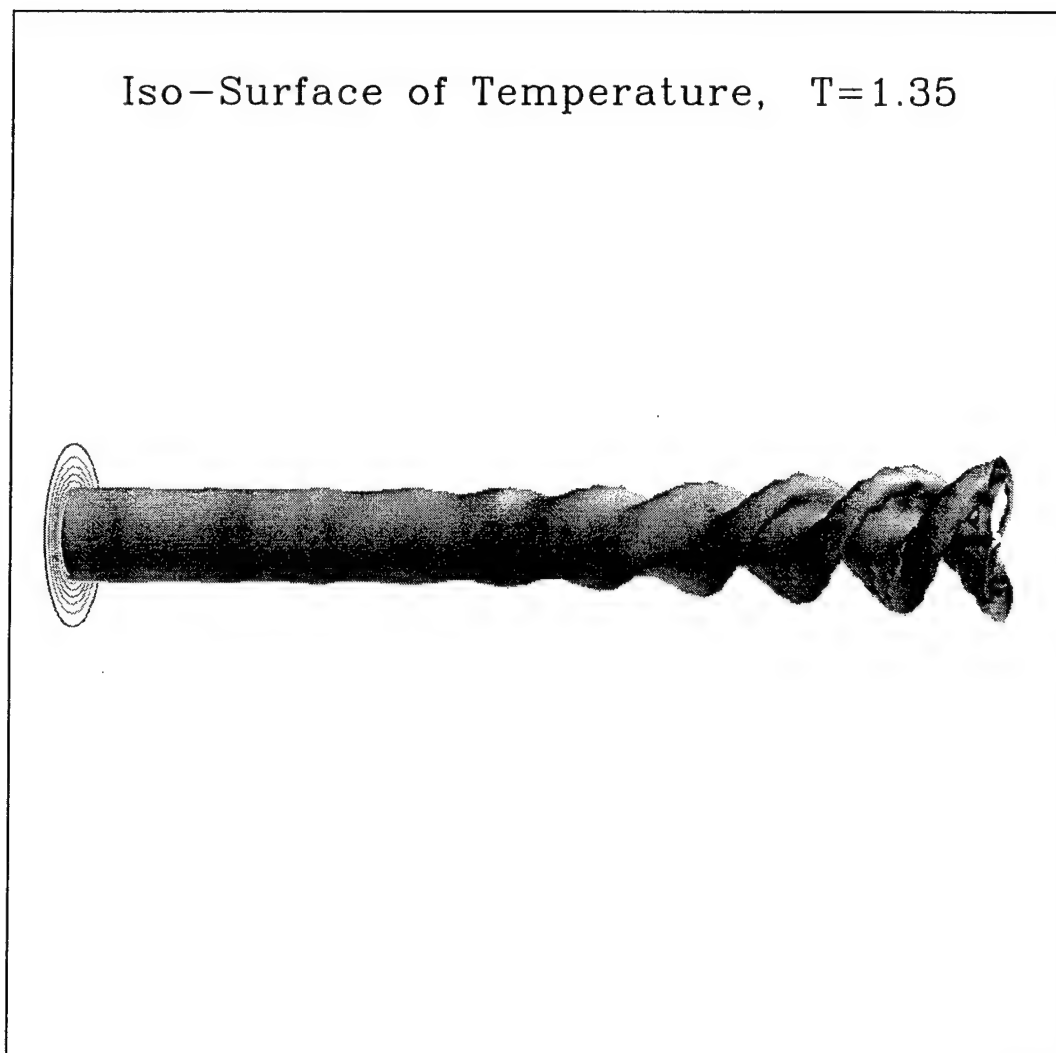
Fig. 49.   Iso-surface of temperature showing the evolution of the vortex core in the streamwise direction.

Fig. 50.   Iso-surface of axial vorticity showing streamwise evolution as two distinct intertwined vorticity sheets.
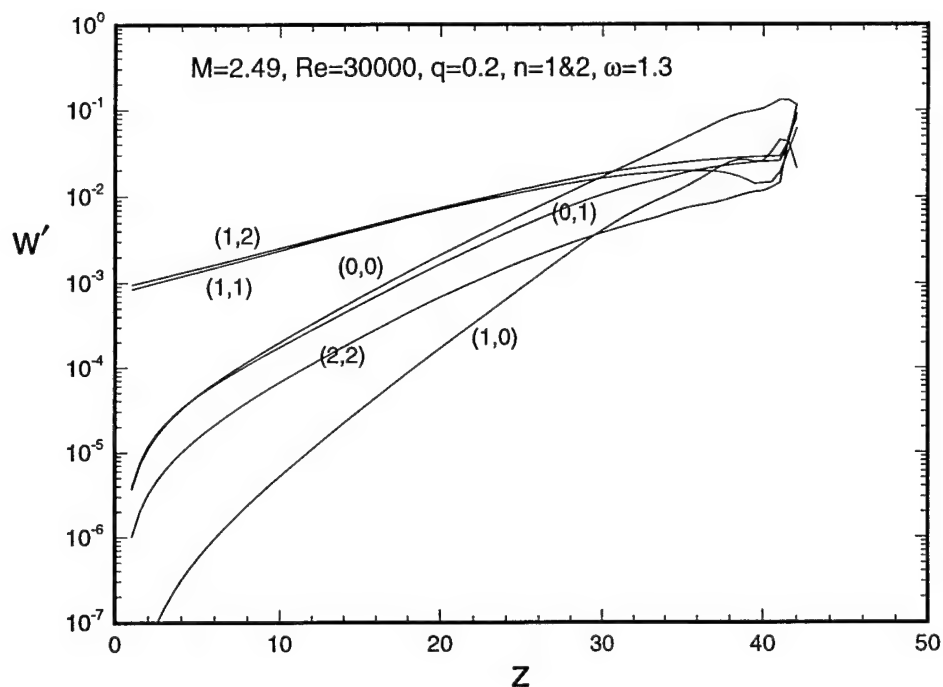
Fig. 51.   Evolution of axial velocity fluctuations with axial distance showing the dominant helical (1,1) and (1,2) modes along with other Fourier harmonic waves.
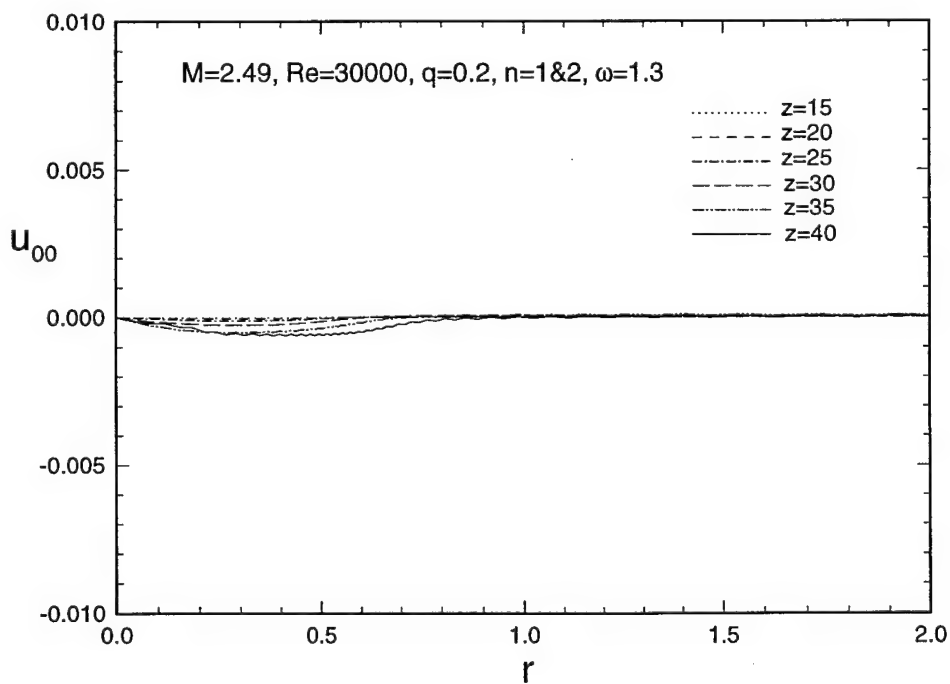
(a) Radial velocity

Fig. 52.   Distribution of various components of meanflow distortion (0,0) mode in the radial direction.
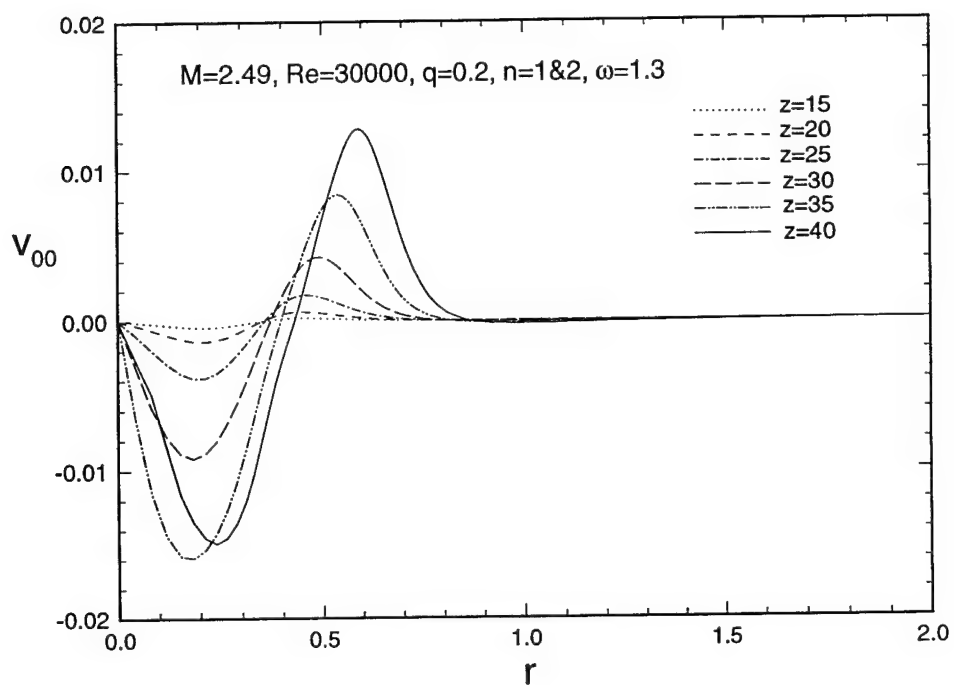
Fig. 52b.   Tangential velocity.

Fig. 52c.   Axial velocity.

Fig. 52d.   Temperature.

Fig. 53.   Axial velocity contour plots in the r-z plane showing the evolution of vortex core in the streamwise direction.

(a) $z = 30$

Fig. 54.   Axial velocity contour plots in the $r - \theta$ plane at different streamwise locations.
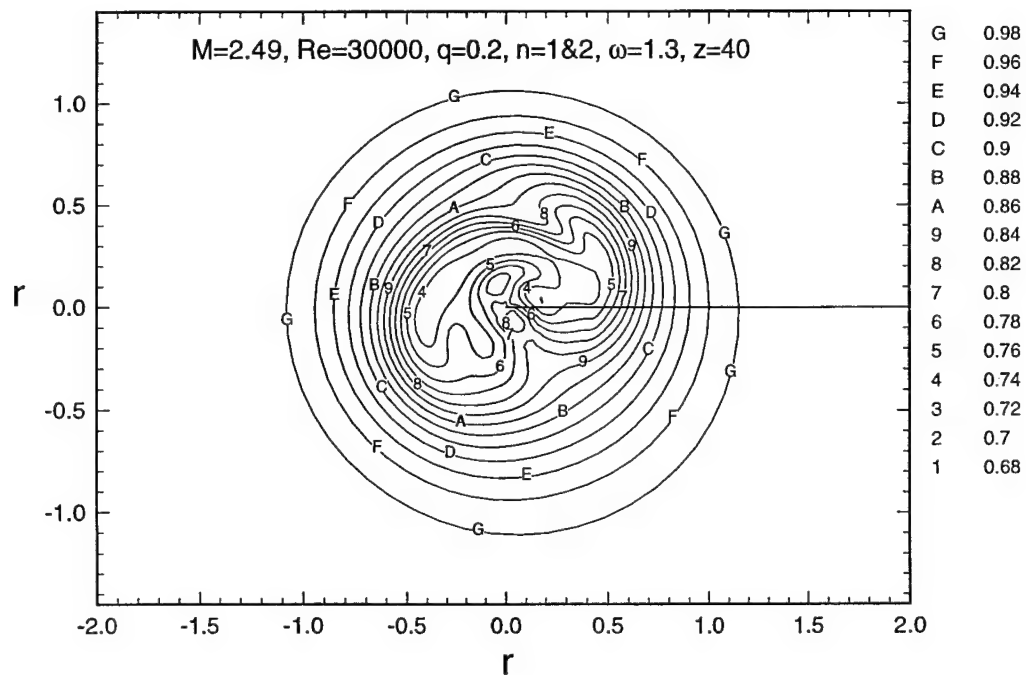
Fig. 54b. $z = 40$
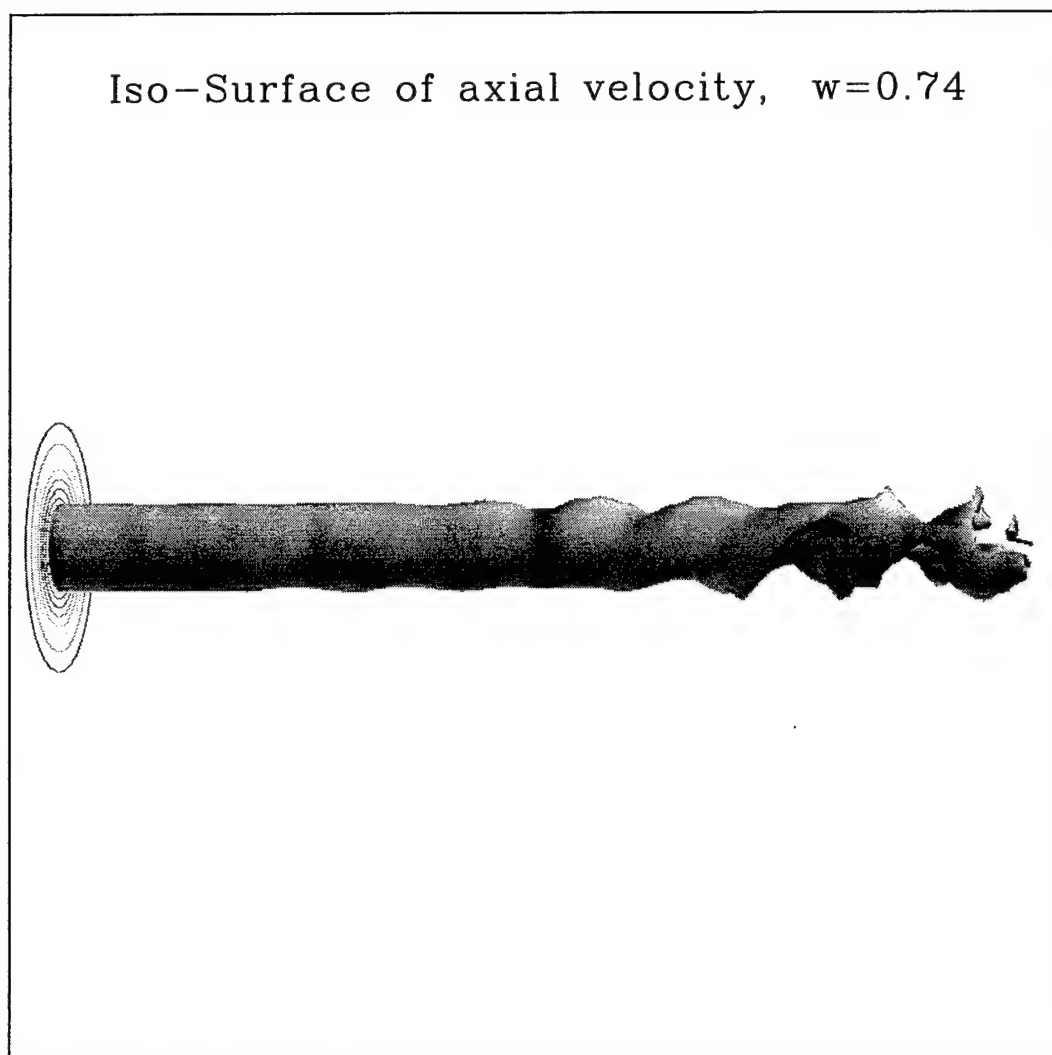
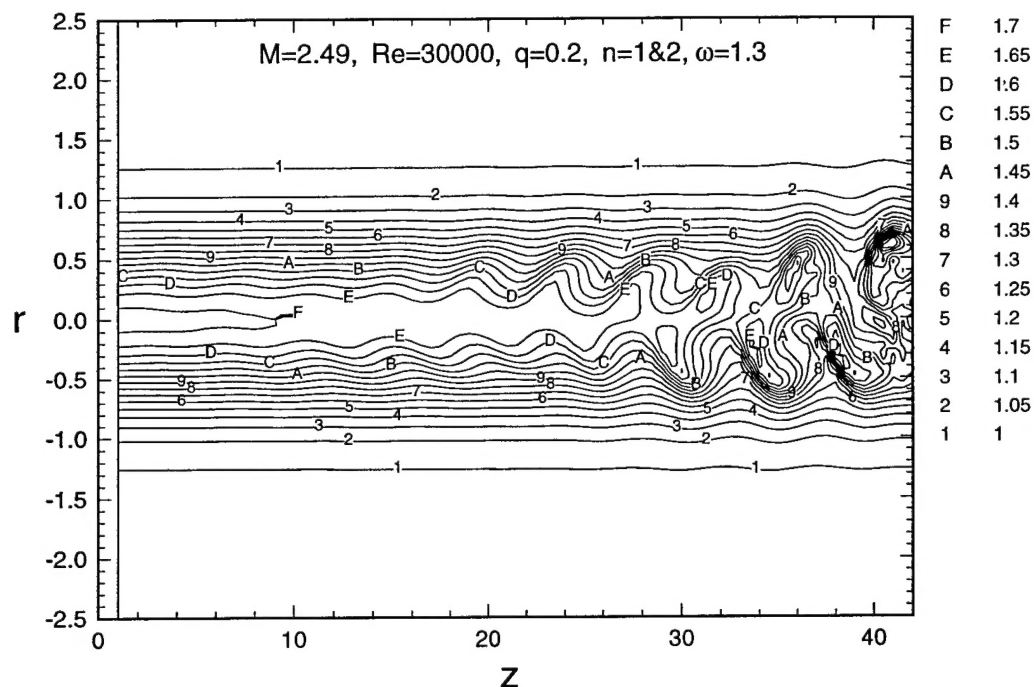Fig. 55.   Iso-surface of axial velocity showing streamwise evolution of vortex core due to nonlinear
interaction between (1,1) and (1,2) modes.

Fig. 56. Temperature contour plots in the *r-z* plane showing the appearance of large scale coherent structures in the nonlinear stage.
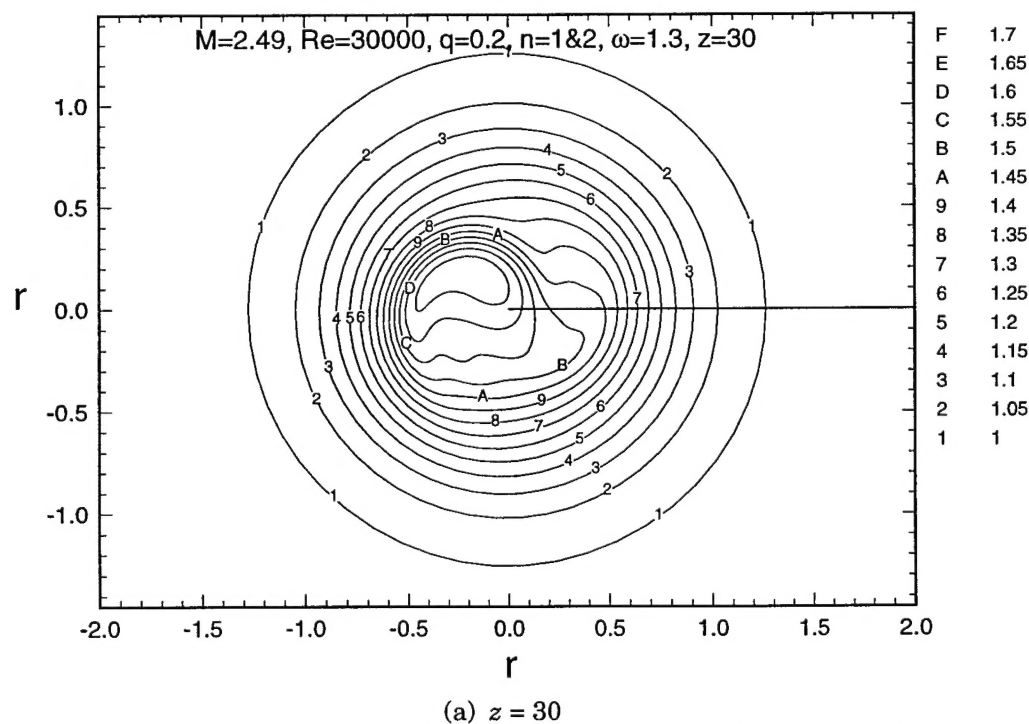

(a) $z = 30$

Fig. 57. Temperature contour plots in the $r-\theta$ plane showing the loss of axisymmetry as the instability evolves downstream.
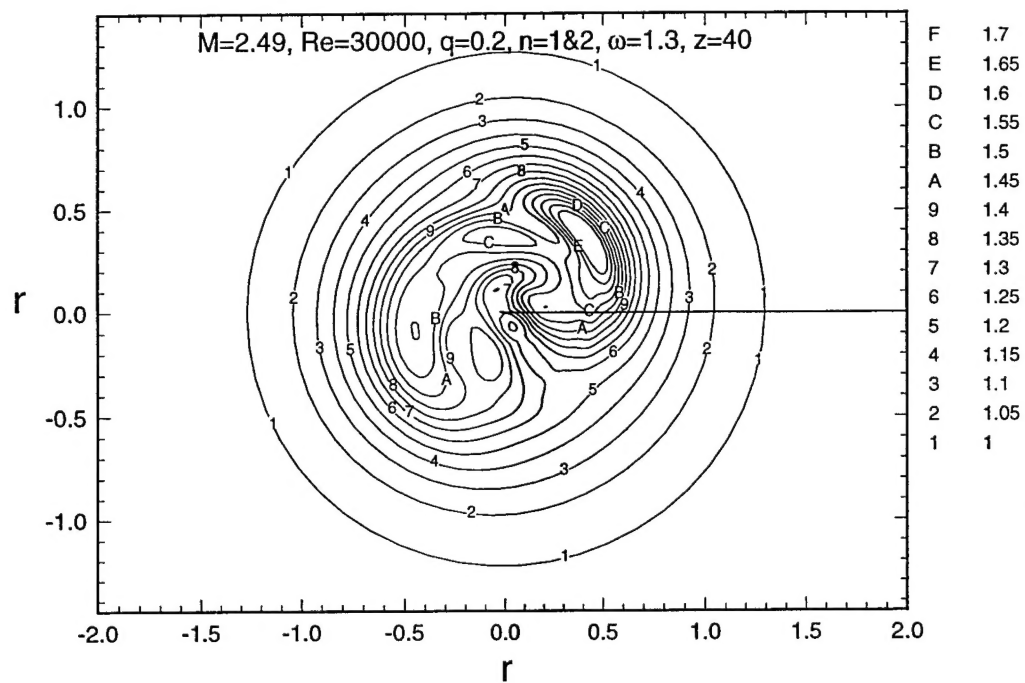
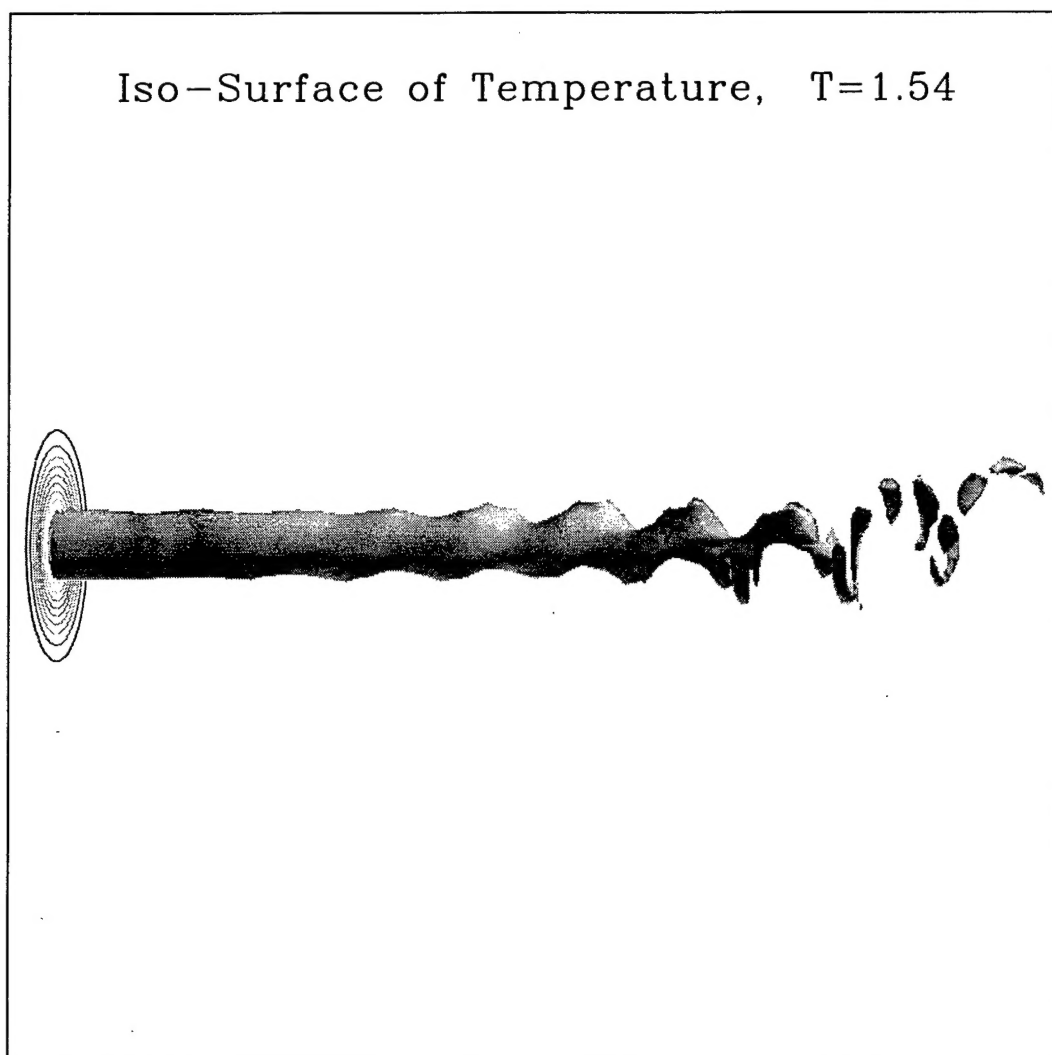Fig. 57b. $z = 40$

Iso-Surface of Temperature, T=1.54

Fig. 58.   Iso-surface of temperature showing evolution of the vortex core in the streamwise direction and its subsequent breakdown into smaller segments of hotter fluid.
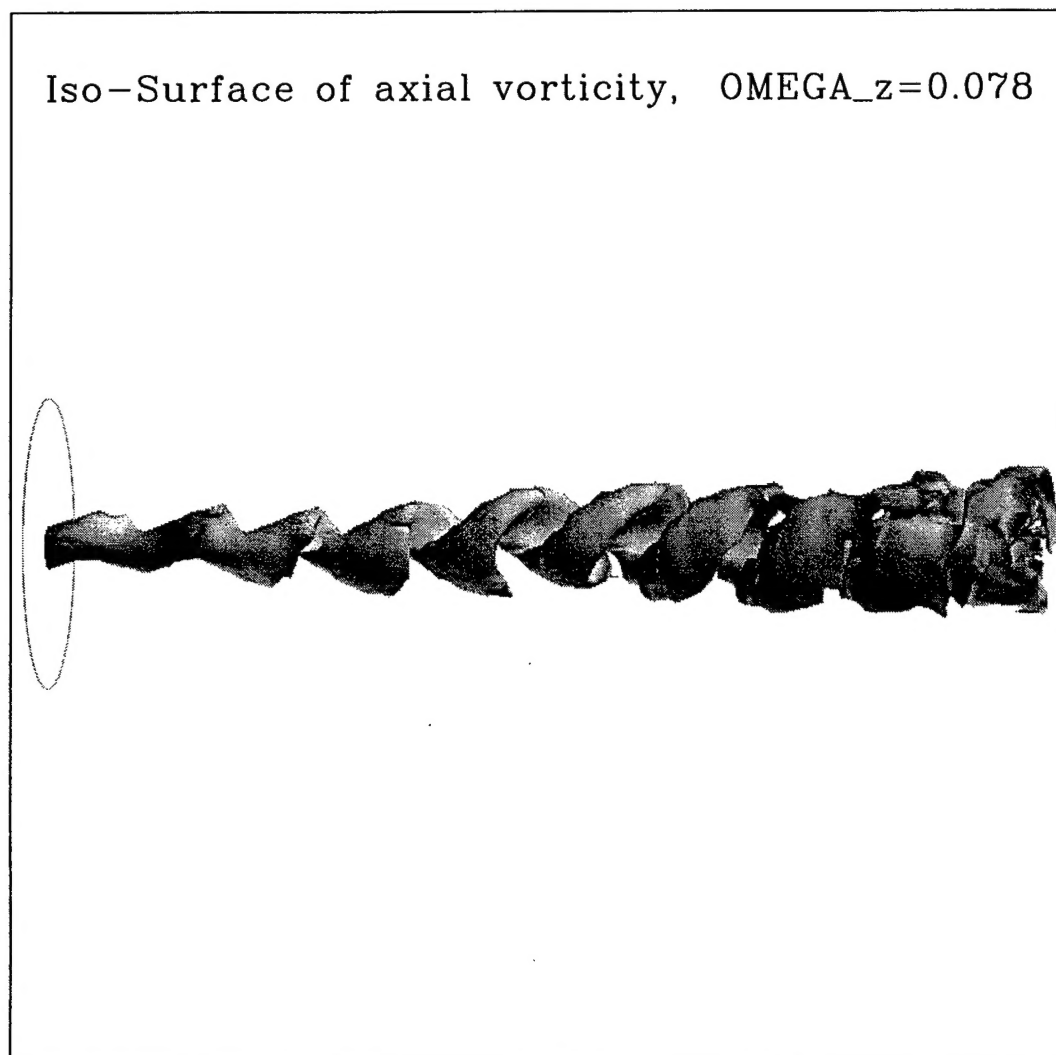
Fig. 59.   Iso-surface of axial vorticity showing the evolution of vorticity field in the vortex core.